Bimetallic Platinum-Chromium Nanoparticles as Electrocatalysts for Proton Exchange Membrane Fuel Cells (PEMFCs)

A thesis submitted to School of Chemical Engineering

University of Birmingham (UK) for the degree of

Doctor of Philosophy

by

Gaurav Gupta

September 2014

Supervisor: Prof. Paula M. Mendes

Co- Supervisor: Dr. Surbhi Sharma

Declaration

Hereby I declare that I wrote this document myself with the help of no more than the mentioned literature and auxiliary means.

Up to now, this document was not published or presented to another examinations office in the same or similar shape.

Birmingham, September 2014
place and date

signature (Gaurav Gupta)

Dedication

To my lovely parents for their constant support in everything I wanted to do.....

Late Professor Ramamurthy Balasubramaniam

(1961-2009)

Table of Contents

List of Figures

List of Tables

Acknowledgments

I would like to express my gratitude towards the School of Chemical Engineering, University of Birmingham for sponsoring my PhD under the College Scholarship.

I would like to take this opportunity to express my appreciation towards my supervisors, Prof. Paula M. Mendes and Dr. Surbhi Sharma for their continuous support and guidance throughout the PhD. I would also like to thank Prof. Kevin Kendall and Dr. Bruno Pollet for giving me the opportunity to do PhD in Fuel Cell Group and for their support during the initial stages of my PhD. I am also thankful to the group members of Hydrogen and Fuel Cell research and Mendes group for their assistance in various practical aspects of this work. Special thanks to Dr. Parvez Iqbal for helping in the work on Core-shell nanaoparticles and teaching me a bit of supramolecular chemistry.

I am thankful to the technical staff at University of Birmingham namely, Theresa Morris, Dr. Artur Majewski, Bob Sharpe for their help in using various equipments for this work. I am also thankful to Dr. Michael Ward, Leeds EPSRC Nanoscience and Nanotechnology Research Equipment Facility (LENNF) for help in TEM analysis and Dr. Anders Barlow, National EPSRC XPS Users Service (NEXUS) for help in XPS analysis.

I am thankful to all my friends especially Vikrant, Sairam, Raghu, Vinu, Vishal, Ankur, Ahmad and Supriya who have always been there for me and also doing the proof reading work at odd hours.

And last but not the least, I would like to convey my deepest appreciation and gratitude to my family, my father, my mother, my brothers Neeraj and Chetan, my sister in laws Prachi and

Roshmi for all their love and constant encouragement in life, to finish my PhD and come back home soon to enjoy time with family and specially my two beautiful nieces Kooho and Misha. Without their support, love and motivation I would have never been able to achieve any of this.

Abstract

Polymer electrolyte membrane fuel cells (PEMFCs) are envisioned to replace internal combustion engines (ICEs) as vehicle power sources and to compete with conventional technologies in backup power systems, residential combined heat and power (CHP) devices and consumer electronics. However, the commercial viability is still hindered due to the cost and durability that are significantly related to the precious metal catalysts used in these cells. In the current work, two different methods towards reducing the precious metal content by the use of transition metal (Cr) with Pt as electrocatalysts for PEMFCs are reported.

The commercial Pt/C catalysts layer consists of three components i.e. Pt, carbon support and Nafion ionomer. The Nafion ionomer binder does not penetrate through the microporous carbon support and thus limits the triple phase boundary region (catalytic reaction takes place at triple phase boundary), which in turn leaves a significant amount of Pt being inactive or not utilised. In the first part of this work, Nafion- stabilised Pt-Cr alloys are synthesised using a novel wet chemical synthesis. The aim of this work is to improve the triple phase boundary region with the introduction of Nafion during the synthesis and alloying with Cr that can enhance the catalytic activity. Thus, in turn improving the utilisation of the catalyst and also reducing the amount of Pt loading.

The formation of the alloys and binding of the Nafion with the nanoparticles are characterized by using different characterization techniques like X-ray diffraction (XRD), transmission electron microscopy (TEM) and X-ray photoelectron spectroscopy (XPS). The results suggested formation of Nafion-stabilised Pt-Cr alloy nanoparticles of ~6 nm with some agglomeration. The Pt-Cr/C catalysts were electrochemically characterized using rotating disc electrode to determine the electrochemical area, catalytic activity towards oxygen reduction reaction. The alloys showed lower electrochemical area and similar specific activity compared to commercial Pt/C catalysts.

Accelerated stress testing was done to study the durability of the alloy catalysts. The results showed a twofold improvement in the durability of the alloy catalysts compared to commercial Pt/C. In-situ single cell testing was done by the fabrication of membrane electrode assemblies to study the polarisation characteristics which gives better representation of a fuel cell environment. The results suggested that alloy catalysts performed half to that of the commercial Pt/C and this can be attributed to the not enough Pt covering the whole of the electrode area and agglomeration of the alloy nanoparticles.

In the second part of this thesis, a new strategy has been proposed for the synthesis of Pt/Cr shell/core nanoparticles that involve the formation of an intermediate Pt ion-containing supramolecular complex/non-noble metal nanomaterial which is later getting reduced to Pt/non-noble metal core/shell nanomaterial. The characterization techniques used could not confirm the formation of core-shell structure, however the presence of both Pt and Cr is confirmed and further analysis by aberration corrected STEM is needed to confirm the core-shell formation. The electrochemical testing of these nanoparticles using rotating disc electrode showed a lower electrochemical area but improved specific activity compared to Pt/C catalysts. Pt/Cr nanoparticles follow different kinetics for ORR reaction and not the four electron process as Pt/C. This is attributed to the formation of partial covering of Pt shell on Cr core and also interaction of Pt with nitrogen from the bipyridine molecule during the synthesis.

Abbreviations

Å	Angstrom
AST	Accelerated Stress Test
CV	Cyclic Voltammetry
ECSA	Electrochemical Surface Area
EDS	Energy Dispersive Spectroscopy
EIS	Electrochemical Impedance Spectroscopy
FWHM	Fixed Width at Half Maxima
GCE	Glassy Carbon Electrode
GDL	Gas Diffusion Layer
HOR	Hydrogen Oxidation Reaction
LSV	Linear Sweep Voltammetry
MA	Mass Activity
MEA	Membrane Electrode Assembly
nm	Nanometer
ORR	Oxygen Reduction Reaction
PEMFC	Proton Exchange Membrane Fuel Cell/ Polymer Electrolyte Membrane Fuel Cell
RDE	Rotating Disc Electrode
RHE	Reversible Hydrogen Electrode
RPM	Revolutions per minute
SA	Specific Activity
SHE	Standard Hydrogen Electrode
TGA	Thermogravimetric Analysis
TEM	Transmission Electron Microscopy
XPS	X-ray Photoelectron Spectroscopy
XRD	X-Ray Diffraction

Chapter 1
Introduction

Fuel cells have attracted a lot of attention in the search for alternative and green energy sources owing to their high efficiencies and low emissions. Proton exchange membrane fuel cells (PEMFCs) are a promising candidate as the next generation power sources for transportation, stationary, and portable applications due to low operating temperature, quick start-up time, high current density and easy scale-up. They are also receiving more importance due to the concerns that petroleum resources are depleting and thus needs an alternate solution as fuel i.e. Hydrogen. Even though the invention of the fuel cell dates back to 1839, the commercialisation has not been fully attained for them. The barriers in the commercialisation are the high costs due to the use of Pt as catalyst and poor durability. The current research focusses on reducing the amount of Pt loading without losing its performance while also improving the durability at the same time.

A major drawback for PEMFCs is the sluggish reaction kinetics for the oxygen reduction reaction (ORR), which leads to high voltage losses within the fuel cell and therefore causes the low conversion efficiency. This also means that a higher amount of Pt catalyst has to be used in the cathode side. The current research aims to reduce the loading of the Pt and improve durability of these catalysts. In order to achieve this aim, the main research focus has been on the following points:

- Forming alloys of non-precious metals (i.e. Cu, Co, Fe, Ni) with Pt
- Core-shell structure of non-precious metals (i.e. Co, Ni, Fe, Cu) forming the core and a monolayer of Pt as the shell.
- Replacing Pt completely with non-precious metals and their alloys (i.e. Co, Fe, Cu, Ni) to obtain similar performance with low cost.
- Ionomer stabilisation (i.e. Nafion, PVP, NP9) to improve utilisation and prevent dissolution of Pt during fuel cell operation.

1.1 Aim and Objectives of the Thesis

Aim:

Synthesis of Bimetallic Pt-Cr electrocatalysts in order to reduce Pt loading in proton exchange membrane fuel cells (PEMFCs).

To achieve the above aim, following objectives were identified:

1) Synthesis of Nafion-stabilised Pt-Cr alloys using wet chemical method. This method will benefit from the advantages of ionomer stabilisation and alloying into one system i.e. stabilisation by Nafion to improve durability, utilisation and Pt-Cr alloy to improve the activity of the catalyst in order to reduce the amount of Pt.
2) Characterisation of these alloys using physical characterisation techniques like TGA, TEM, XRD, XPS.
3) Electrochemical characterisation of these alloy catalysts to study the electrochemical area, catalytic activity and durability.

A new approach for the synthesis of Cr/Pt core/shell nanoparticles was also investigated using supramolecular chemistry. However, it was a short study and needs a more detailed investigation.

1.2 Thesis Overview

A brief overview of the different chapters of this thesis has been given under:

Chapter-2: Provides an overview of fuel cells, history, and different type of fuel cells. It also discusses the various catalysts in the proton exchange membrane fuel cells and the need and scope of developing new electrocatalysts i.e. alloys and core-shell.

Chapter-3: Discusses the synthesis techniques for Pt-Cr alloys and Cr/Pt core/shell nanoparticles employed in this study. It also explains the principles and techniques used for the characterisation of these nanoparticles as electrocatalysts.

Chapter-4: Consists of detailed characterisation of Nafion-stabilised Pt-Cr alloy catalysts using wide range of characterisation techniques like TGA, TEM, XRD and XPS, in order to understand the composition, size and distribution of the nanoparticles, also the oxidation states of the different elements.

Chapter-5: Investigates the electrochemical surface area, catalytic activity towards ORR and durability of the Pt-Cr alloys synthesised in this study. Effect of the presence of Nafion and amount of Cr is also studied.

Chapter-6: Consists of the detailed characterisation of Pt-Cr samples prepared in an attempt to synthesise Pt-Cr core-shell structures using characterisation techniques like NMR, FTIR, TGA, TEM, XRD and XPS. It also consists of the electrochemical studies done on these nanoparticles like electrochemical surface area, activity towards ORR.

Chapter-7: Provides the comprehensive conclusions of this study and also the recommendations for future work that can be done on the various aspects of this research.

Chapter 2
Literature Review

This chapter provides an introduction to fuel cells, which includes the history of the fuel cells and various types of fuel cells that exist in the current market. Following this, the focus will be shifted to the polymer electrolyte membrane fuel cells (PEMFCs) as the current project is to synthesise and study catalyst materials for the PEMFCs. Recent studies are outlined, highlighting the different techniques used to lower the Pt loading, increase the fuel cell performance and durability. The chapter is concluded by summarising the major advantages of these studies.

2.1 Introduction to Fuel Cells

A fuel cell is an electrochemical device that provides efficient conversion of the chemical energy of fuels directly into electricity for power generation. It can also be defined as an energy conversion device that electrochemically converts chemical energy of two reactants, a fuel and an oxidant into electrical energy. Fuel cells and direct electrochemical fuels (particularly hydrogen) can be the long-term solution to the improvement of energy efficiency, energy sustainability, energy security and the reduction of greenhouse gases and urban pollution. Significant environmental benefits in the field of energy conversion for transportation and electric power generation are expected from fuel cells.

2.2 History of Fuel Cells

The first step towards the discovery of fuel cells took place more than two centuries ago but commercialisation of these systems is still to be achieved because of certain barriers like cost, efficiency, and infrastructure. This journey started when Christian Friedrich Schönbein described the operational principle of fuel cells in January 1839 and Sir William R. Grove fabricated the first prototype cells on the same principle [1]. The basic principle which was mentioned and used is reversing the water electrolysis process to generate electricity from hydrogen and oxygen as fuel. The principle still remains the same "*A fuel cell is an electrochemical 'device' that continuously converts chemical energy into electrical energy (and some heat) for as long as fuel and oxidant are supplied*".

Figure 2.1 shows the setup, used by Grove as the first prototype cell, consisting of platinum strip electrodes surrounded by tubes containing hydrogen and oxygen in a dilute solution of sulfuric acid and water. The performance of the cell was however found to be highly inconsistent with other electrolytes and fuels.

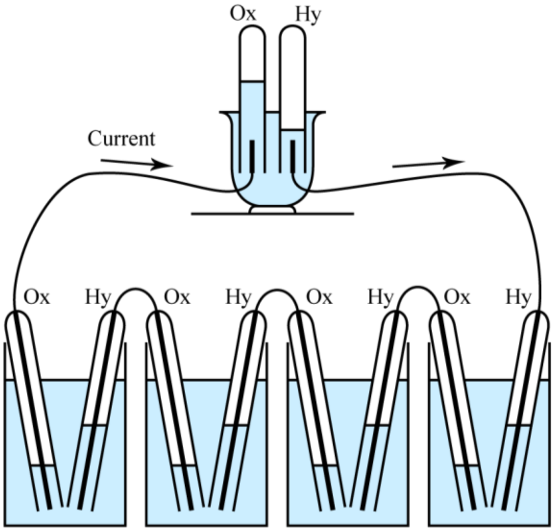

Figure 2.1: William Grove's prototype fuel cell [1]

In 1890s almost 50 years from the discovery of fuel cells, major breakthrough was made by Ludwig Mond and Charles Langer [2]. They modified the design of Grove's cell by using improved porous electrodes. They built the first practical device to be operated on air and coal gas as the fuels and after testing of their cell of 700 cm^2 covered with 0.35 g of Pt foil and 1 g of Pt black, they were able to obtain a current density of 2.8-3.5 $mAcm^{-2}$ at 0.73 V. Furthermore, they identified that internal resistance and concentration polarization are the mechanism for huge losses at the oxygen electrode.

William Ostwald realised the great potential of fuel cells – for example, the possibility of obtaining high thermal efficiencies and he came up with the idea of using carbon as the fuel with oxygen or air as the oxidising agent [3]. In 1897, William White Jacques improved on the idea of Ostwald to use carbon as the electrode and fused sodium hydroxide as the electrolyte to develop 1.5 kW fuel cell battery [4].

Even though Germany laid the foundation for carbonate cycle and solid oxide fuel cells, it was Dr. Francis T. Bacon who made significant contribution to the fuel cell technology [5]. He found that potassium hydroxide performed as well as acid electrolytes and was less corrosive to the electrodes. In 1959, he demonstrated a practical 5 kW hydrogen-oxygen fuel cell stack that provided 700 $mAcm^{-2}$ at 38 bar and 200°C [5]. Based on the Bacon's studies, a 15 kW fuel cell stack was used to power a tractor by Allis-Chalmers Manufacturing Co. operating at a lower temperature and pressure.

The development of fuel cells was further encouraged due its application as stationary source of electricity for on-board space aircrafts [6]. In 1965, fuel cells (polymer electrolyte membrane fuel cells) were first used as power source on the space mission in Gemini V which was developed by General Electric. This resulted in the doubling of the space flight record compared to Gemini IV and thus outperformed the battery systems used on previous missions [7, 8]. In 1966, Nafion ionomer replaced the sulfonated polystyrene membranes as electrolytes because of better performance and durability [7, 8].

Fuel cells performed successfully in the space programs but they were very expensive and thus the use was limited to only space missions and other special applications. In 1990s, with the invention of thin-film electrodes, the Pt loading was reduced. Thus, bringing the cost down and opening the fuel cells system market for other applications [7, 8]. The automotive and distributed energy sectors were the major player in the research and development of fuel cells. This was driven due to various factors ranging from 1) limited reserves of fossil fuels, 2) limitations on green house gas emissions. This led to search for a clean fuel and efficient replacement for the internal combustion engine and fuel cells were the perfect contender. Due to the requirements for higher energy density and longer operational times, fuel cells was also seen as an alternative in the portable electronics, e.g. laptop computers, smart phones and other handheld devices [7, 8].

Even though the technology of fuel cells is good enough for commercialisation, the cost of the production is still very high. Fuel cells have to perform better at competitive cost in order to enter the market which is already saturated. Therefore, current research aims at lowering the cost to a competitive level by replacing expensive materials and improving performance.

2.3 Types of Fuel Cells

Fuel cell types are usually characterised by their electrolyte, operating temperature, transported ion and fuel. A summary of fuel cell types with respective electrolyte materials, transported ions and operating temperatures are presented in table 2.1.

Table 2.1: Summary of most common fuel cell types [7, 8]

Fuel Cell Type	**Electrolyte Material**	**ion**	**Operating Temperature**	**Fuel**	**Electrical efficiency**	**Power Range/ applications**
Polymer electrolyte membrane fuel cell (PEMFC)	Cation conducting polymer membrane	H^+	20-80 °C	Pure H_2	35-60%	5-250 kW, Automotive, CHP, Portable
Direct methanol/ethanol fuel cell (DMFC/DEFC)	Cation conducting polymer membrane	H^+	20-80 °C	Methanol/ ethanol	35-60%	5-250 kW Automotive, CHP, Portable
Phosphoric acid fuel cell (PAFC)	Molten phosphoric acid (H_3PO_4)	H^+	150-200 °C	Pure H_2	40%	200 kW, CHP
Alkaline fuel cell (AFC)	Aqueous alkaline solution (e.g. KOH)	OH^-	< 250 °C	Pure H_2	35-55%	< 5 kW, niche markets (military, space)
Molten carbonate fuel cell (MCFC)	Molten alkaline carbonate (e.g. $NaHCO_3$)	CO_3^{2-}	600-700 °C	H_2, CO, CH_4, other hydrocarbons	> 50%	200 kW- MW range, CHP and stand-alone

Solid oxide fuel cell (SOFC)	O^{2-} conducting ceramic oxide (e.g. $Y_2O_3^-$ stabilised ZrO_2)	O^{2-}	600-1000 °C	H_2, CO, CH_4, other hydrocarbon	> 50%	2 kW- MW range, CHP and stand-alone

From the fuel cell types listed in Table 2.1, molten carbonate fuel cells and solid oxide fuel cells are classified as high temperature fuel cells, the rest are classified as low temperature fuel cells.

Alkaline fuel cells (AFC): They are named after the electrolyte that is being used like potassium hydroxide, which is alkaline. They work on the principle that the negatively charged ions, OH^- from the cathode travel through the electrolyte to the anode and combine with hydrogen to produce water and electrons[7, 8].

$$\text{Anode:} \quad H_2 + 2OH^- \longrightarrow 2H_2O + 2e^-$$

$$\text{Cathode:} \quad \tfrac{1}{2} O_2 + 2e^- + H_2O \longrightarrow 2OH^-$$

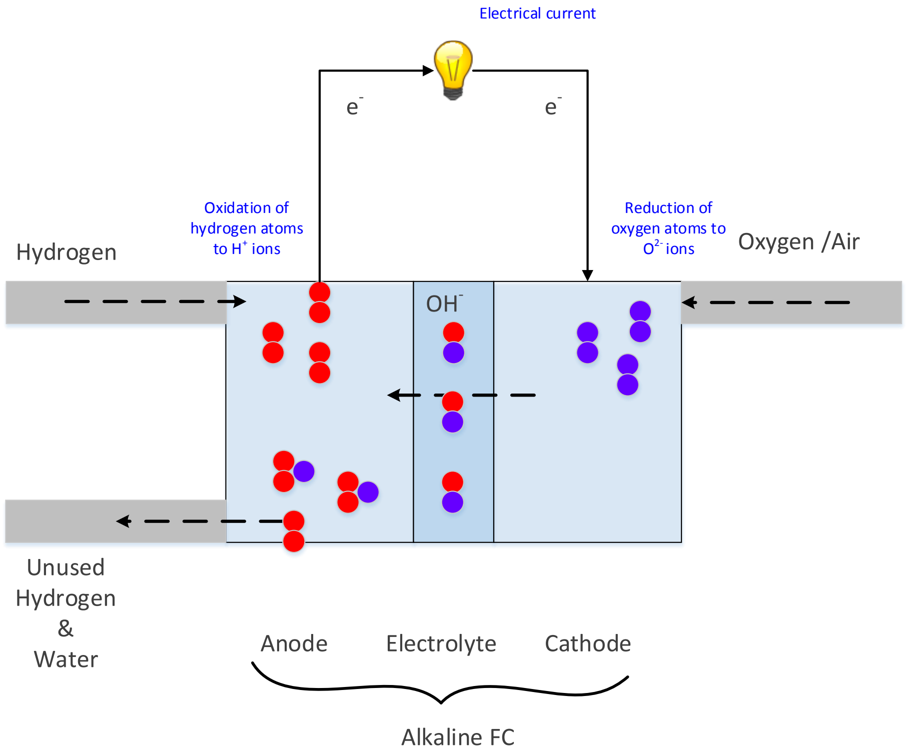

Figure 2.2: Schematic of alkaline fuel cell.

They were the first fuel cells to be used for practical applications in NASA's space missions. The major drawback for these fuel cells is the sensitivity to carbon dioxide and therefore the use of pure oxygen and hydrogen as the reactants which make AFCs expensive for terrestrial applications. Hydrogen is the main fuel, but alternative fuels like low alcohols and sodium borohydride has also been studied [9, 10]. AFCs are used in applications that require high performance regardless of price, e.g. space and military applications.

Phosphoric acid fuel cell (PAFC): These fuel cells are considered as the first generation commercial fuel cell type. The principle of these cells is similar to the PEMFCs where hydrogen is oxidized at anode to H^+ ions and these ions travel through the electrolyte to the cathode where they react with O_2 to produce water and generate electricity[7, 8].

$$\text{Anode: } H_2 \longrightarrow 2H^+ + 2e^-$$

$$\text{Cathode: } \tfrac{1}{2}O_2 + 2H^+ + 2e^- \longrightarrow H_2O$$

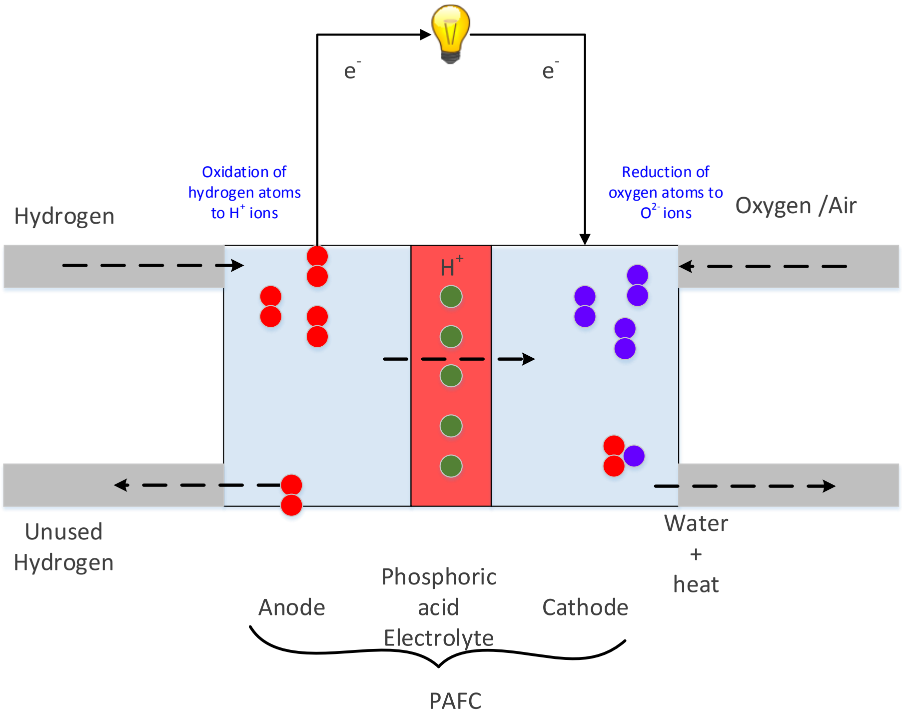

Figure 2.3: Schematic of phosphoric acid fuel cell.

The major advantage of these fuel cells is the tolerance to the carbon monoxide and carbon dioxide. Owing to an operating temperature closer to 200 °C and their tolerance to CO, there are wide variety of fuels which can be used including natural gas, petroleum products, coal liquids and coal gases. PAFCs have been used mostly for stationary electricity and heat production and the efficiency can be increased to about 85% by using as CHP cogeneration system[7, 8]. The cost of these cells is higher owing to the use of Pt in both anode and cathode sides. Due to the highly corrosive nature of the phosphoric acid, corrosion resistant materials have to be used which further add to the cost and make them more expensive.

Direct methanol, ethanol and formic acid fuel cells: They are closely related to polymer electrolyte membrane fuel cells and can be considered a subset of PEMFCs. The main difference between these cells is the fuel used instead of hydrogen rich gas. These cells are designed to use liquid fuels and tolerate more carbon monoxide on the anode side, which is created as a by-product in fuel oxidation. The cathode side is often identical to that in PEMFCs. The main advantage being the easy handling on the fuel and also provide high energy density. The major drawbacks or problem with these fuel cells is the methanol crossover from the anode to the cathode side which results in the poisoning of the cathode catalysts leading to voltage loss[7, 8].

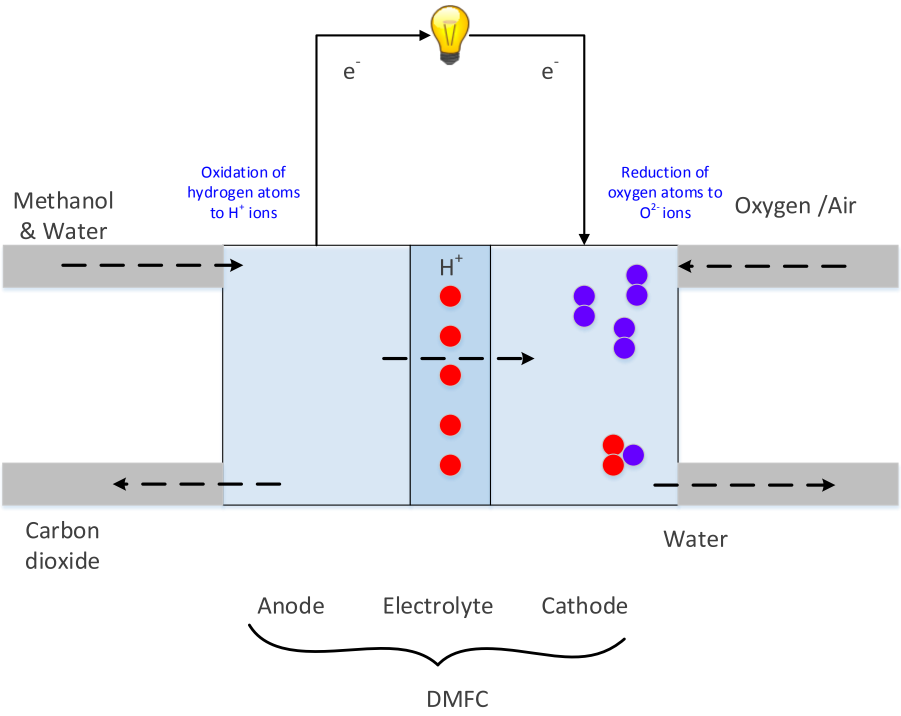

Figure 2.4: Schematic of direct methanol fuel cell.

Molten carbonate fuel cell (MCFC): In this case, the negative ions from the cathode travel through the electrolyte to the anode and combine with hydrogen to generate water and release electrons. The negative ions which move through the electrolyte are the CO_3^- ions that form when CO_2 and O_2 react at the cathode[7, 8].

$$\text{Anode:} \quad H_2 + CO_3^{2-} \longrightarrow CO_2 + 2H_2O + 2e^-$$

$$\text{Cathode: } \tfrac{1}{2} O_2 + CO_2 + 2e^- \longrightarrow CO_3^{2-}$$

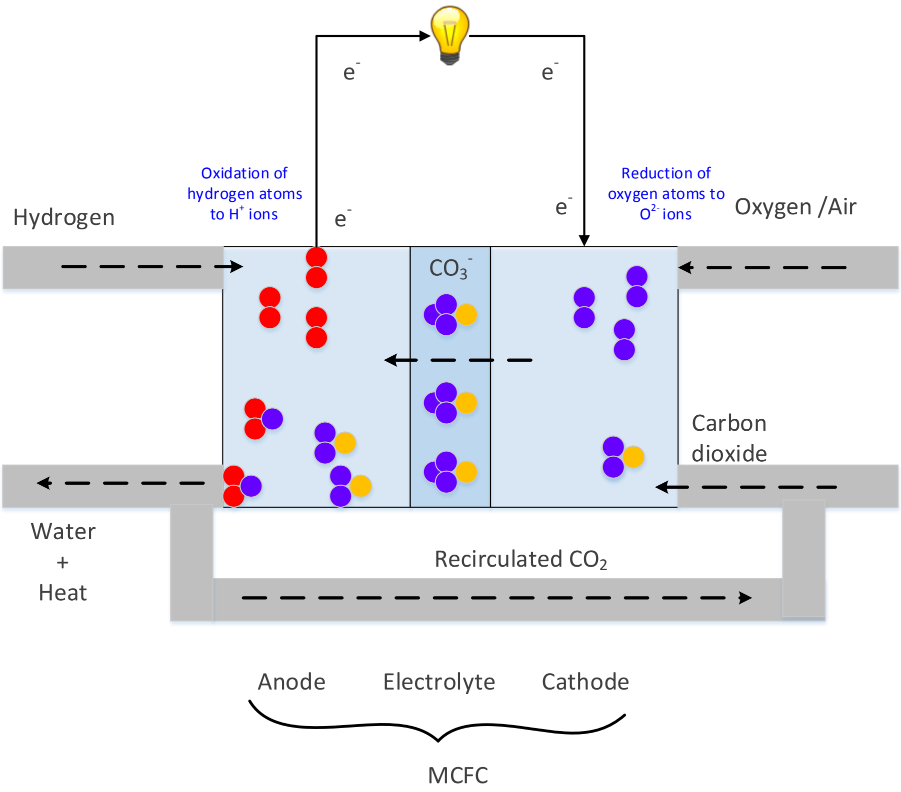

Figure 2.5: Schematic of molten carbonate fuel cell.

Due to the higher operating temperature of these fuels (~650C), cheap catalysts like nickel can be used to given sufficient activity for electrochemical oxidation and reduction and thus improving on the cost [7, 8]. Carbon monoxide can be used as fuel in addition to various common fossil fuels and renewable fuels that can be reformed internally. However, use of expensive materials for various cell components is required to achieve good mechanical stability and sufficient lifetime owing to high operating temperature and corrosive electrolyte.

Furthermore, recycling of the anode exhaust can serve as the source of carbon dioxide which acts as fuel on the cathode side.

Solid oxide fuel cells (SOFC): They also work on the similar principle as MCFCs and AFCs where the negatively charged oxide ions from the cathode travel through the solid electrolyte to the anode, react with hydrogen and form water(steam in this case) while releasing electrons[7, 8].

$$\text{Anode:} \quad H_2 + O^{2-} \longrightarrow H_2O + 2e^-$$

$$\text{Cathode:} \ \tfrac{1}{2}\, O_2 + 2e^- \longrightarrow O^{2-}$$

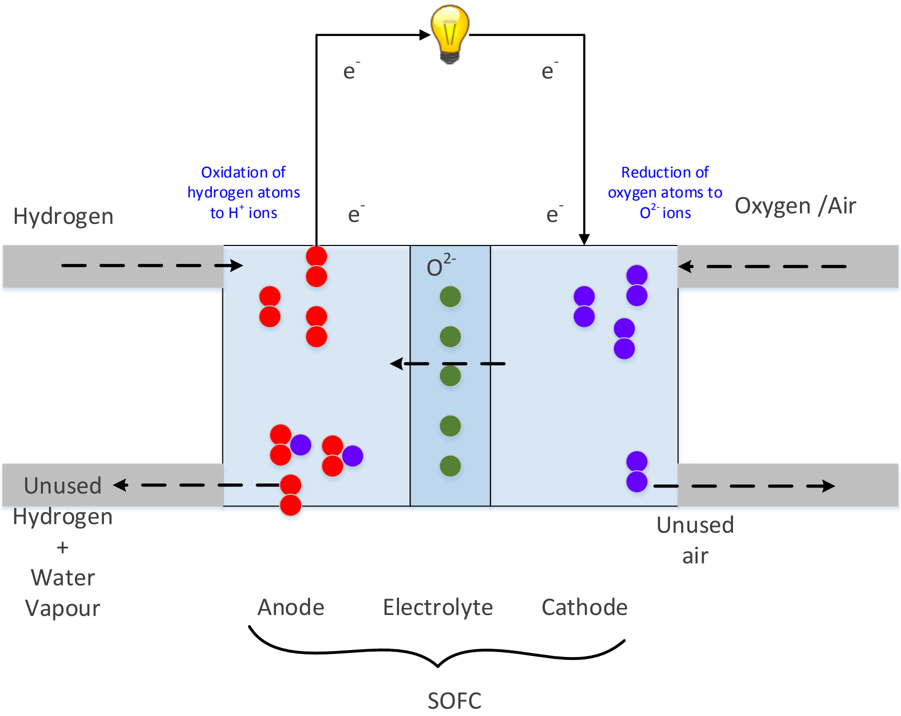

Figure 2.6: Schematic of solid oxide fuel cell.

High operating temperature also allows the use of various hydrocarbons and even CO as fuel. It further enables the use of waste heat for cogeneration or use in steam turbines and also eliminates the need for noble metal catalysts. The electrolyte is a hard ceramic compound (yttria-stabilised zirconia) and the cell involves only two phases i.e. gas and solid thus eliminating material corrosion and water management problems[7, 8]. However, thermal expansion and corrosion of metal components is an issue due to the high operating temperature. SOFCs are best suited for stationary and distributed power generation, either in heat and power cogeneration or hybrid systems with gas turbines.

2.4 Polymer Electrolyte Membrane Fuel Cell (PEMFC)

The invention of the PEMFC dates back to 1960 by Thomas Grubb and Leonard Niedrach at General Electric. It works on the principle of converting chemical energy into electrical energy through an electrochemical reaction. Membrane electrode assembly (MEA) forms the key part of the PEMFC. It consists of a polymer electrolyte in contact with the anode on one side and cathode on other side. A schematic of PEMFC is shown in Figure 2.7.

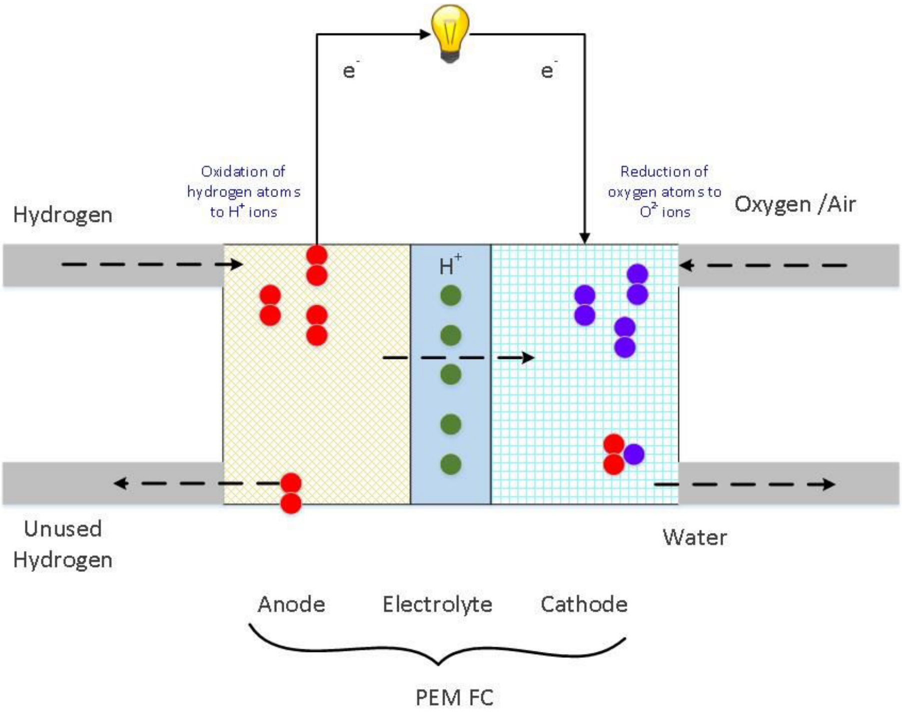

Figure 2.7 Schematic of a proton exchange membrane fuel cell (PEMFC)

Hydrogen is used as the fuel on the anode side and oxygen as oxidant on the cathode side which are separated by proton conducting polymer (ionomer) membrane as the electrolyte. Hydrogen molecules are oxidised on the anode and protons is transferred through the electrolyte membrane to the cathode which reacts with oxygen and electrons to form water and heat.

The reactions taking place in hydrogen fed PEMFC are as follows[7, 8, 11] :

Anode reaction: $H_2 \rightarrow 2H^+ + 2e^-$ $E° = 0$ V vs RHE (2.1)

Cathode reaction: $½O_2 + 2H^+ + 2e^- \rightarrow H_2O$ $E° = +1.23$ V vs RHE (2.2)

Overall reaction: $H_2 + ½O_2 \rightarrow H_2O$ $E° = +1.23$ V vs RHE (2.3)

The most commonly used catalyst in PEMFC is platinum supported on carbon black. The role of the catalyst is to enable the reaction and also increase the half cell reactions rate on the anode (oxidation of hydrogen) and the cathode (reduction of oxygen) side [7, 8, 11].

The standard operating temperature for PEMFCs ranges between 80-120 °C. While the operating temperature range for PEMFCs can be extended, it is restricted between freezing and boiling points of water. This is due to need of humidification of the electrolyte membrane which is essential for proton conductivity. They can be used below freezing temperature but the conditions can damage the membrane when fuel cell is not operating. With the use of high temperature membrane which can maintain proton conductivity at higher temperature, the operating temperature can be expanded above boiling points of water [7, 11]. The benefits of PEMFCs are quick startup, quick load following and ease of electrolyte handling, low corrosion and system robustness due to solid electrolyte.

The major drawbacks are the mass transfer due to the presence of liquid water which can cause flooding and reduce the performance. Even very low concentration of carbon monoxide can cause the poisoning of the catalyst at normal operating temperature range[11].

There are certain barriers for the commercialisation of the PEMFC even though the technology is ready for applications. These barriers include cell durability, lifetime alongwith the higher cost of the catalysts and ionomer which makes them very expensive to compete in the market which is already saturated. The cost of the assembly and manufacturing can be decreased with mass production but to decrease the cost of catalysts and ionomer- less expensive materials have to be identified [7, 11].

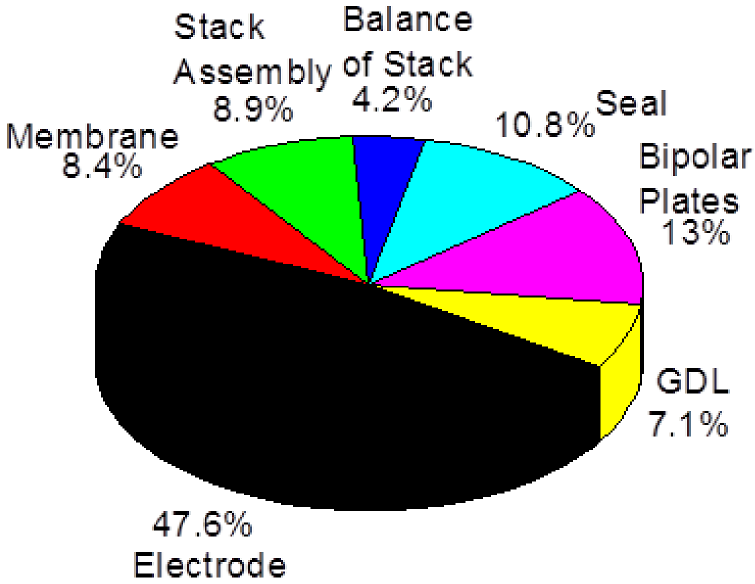

Figure 2.8 Cost breakdown for an 80 kW PEMFC stack, assuming Pt cost of approx. £25/g and overall Pt loading 0.15 mg.cm^{-2} as per DOE report 2010[12]

The cost of the fuel cell stack was estimated to be about \$22/kW for 2010 and the target for 2015 is set to \$15/kW as per U.S. department of energy [12]. The main components that contribute to about 50% (Figure 2.8) of the total cost are the electrodes [12-14]. Pt-based electrocatalysts used in the electrode are the main contributor to the cost. Unfortunately, these are currently the only viable choice in PEMFCs due to their high exchange current density for oxygen reduction, a high resistance to chemical attack, excellent high-temperature characteristic and stable electrical properties [15]. There are certain limitations which prevent the use of Pt on a large scale like the expensive nature and limited worldwide availability of Pt. The platinum loading is typically about 0.05–0.2 $mgcm^{-2}$ on the anode side and 0.2–0.6 $mgcm^{-2}$ on the cathode side. More platinum is used on the cathode side because of the sluggish oxygen reduction reaction which dictates the performance of the fuel cell rather than anodic hydrogen oxidation reaction [15, 16]. The approach applied for reducing the cost of the fuel cells is to lower the percentage of the Pt in the catalyst on the cathode side without affecting the performance. The other way is to develop non-precious ORR catalyst with better catalytic activity and durability.

2.5 Cathode Catalysts for PEMFCs

The catalyst plays an important role in the PEMFC and forms the fundamental component in the operation and performance of the cell. The catalysts layers are formed by the mixing of colloidal solution of metal with addition of Nafion® and supported on the carbon in the form of an ink. The role of Nafion® in this mixture is to increase the adherence of the catalyst to the electrode. This results in the increase of triple phase boundary between catalyst, ionomer and carbon support and eventually increases the catalyst utilisation and reducing the ohmic resistance. Triple phase boundary is defined at the point of between the ion conducting phase (ionomer), electron conducting phase (carbon support) and gas phase on the electrode which is required for the electrochemical reaction to take place. A schematic of triple phase boundary showing the different phases is shown in figure 2.9.

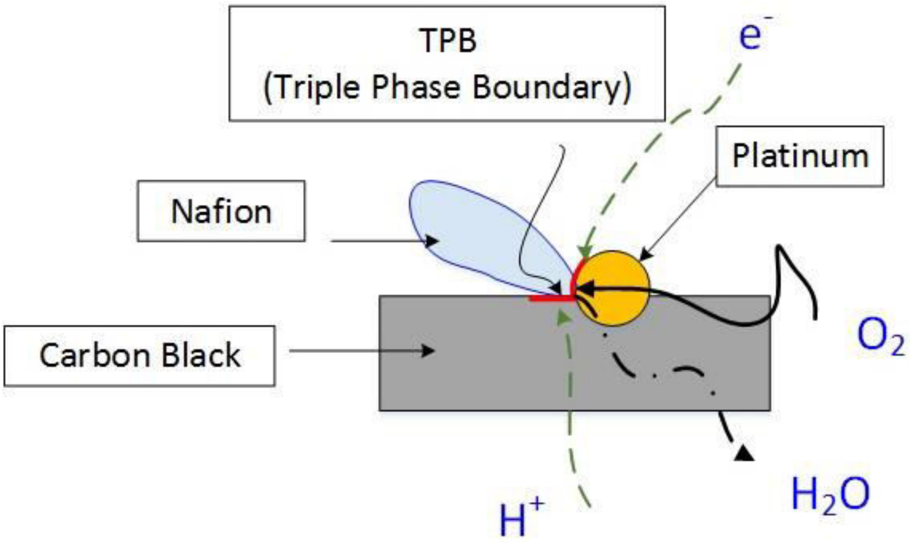

Figure 2.9: Schematic of a triple phase boundary

A lot of research has been done on different catalyst systems for their possible use as cathode catalyst in fuel cells ranging from precious metals like Pt, Pd, Au and non-precious metals like Cu, Co, Fe [17-23]. The approach towards the development of these catalysts has been based on the performance and the cost of the resulting catalyst. The cost can be reduced by the use of the non-precious metals. However, there is loss in the performance due to the use of less active non-precious metal. Alloying of precious and non-precious metals has attracted a lot of interest from the researchers in order to improve the performance of the catalyst while reducing the cost.

2.5.1 Non-precious Metal Catalysts

There has been a lot of research on the non-precious electrocatalysts which eliminate the use of noble metals like Pt, Pd or Au and use alloys of Fe, Ni, Cu and other transition metals. To date a number of non-noble metal electrocatalysts have been investigated and evaluated for the PEMFC. However, these electrocatalysts were not even able to match the performance of

Pt-based alternatives which achieve power densities of the order of 1000 mW cm^{-2} [20, 24, 25]. These catalysts include complexes of transition metal with macrocycles, carbides, chalcogenides, porphyrins and nitrides [18, 26-38]. The best performance reported till date is that of iron and cobalt macrocyclic complexes with power density of ~70 mW cm^{-2}[18]. The activity and the durability of non-precious metal electrocatalyst is still a challenge for the commercialisation [15].

2.5.2 Precious Metal Catalysts

Pt has been the most viable choice for use as cathode electrocatalysts. However, due to the high cost of Pt (approx £33/g as at 10th Sep, 2014) and limited availability of the Pt reserves, a lot of attention is diverted to the use of transition metals alloyed with Pt. This not only reduces the cost but also increases the activity and durability of the catalyst[6, 8, 11]. Different alloy systems have been studied over the past decade comprising binary as well as certain ternary alloys. Some of these alloys include Pt-Co[39-47], Pt-Ni[46-52], Pt-Ru[53-57], Pt-Au[58-61], Pt-Pd[62-66], Pt-Co-Cr[55, 56, 67] Pt-Ni-Cu[50], Pt-Ni-Co[50]. Previous studies have suggested that the Pt-Cr alloy system also possess higher activity for ORR as compared to the Pt/C commercial [68] but very limited literature is available on the performance of this system for ORR. Some of the studies will be explained in section 2.6.4.

2.6 Reduction of Pt Amount or Prevention of Dissolution of Pt in the Fuel Cell

This section will highlight the recent developments in the field of fuel cells to reduce the amount of Pt, better utilisation and durability of the catalyst in the fuel cell. There are certain ways of reducing the amount of Pt in the system: by alloying, using core-shell structures or using non-precious catalysts. The dissolution of Pt in the fuel cell can be prevented by stabilising the catalyst with ionomer, which can also improve the triple phase boundary [69-73] and can result in better utilisation of the catalyst. All these systems will be discussed in detail below:

2.6.1 Stabilisation of the Catalyst with Ionomer

Even though the physical surface area of catalysts improved with the introduction of electrocatalysts supports, but the electrochemically active surface area was still very low. The electrochemical area, which participates in the reaction, is the region where the catalyst is in contact with reactant gases, product media while maintaining the electrical contact with the electrode. This region is known as the triple phase boundary.

In the 1980s, it was demonstrated that with the incorporation of proton-conducting ionomer within the pore structure of the catalyst layer, the performance of the catalysts can be improved with reduction of Pt loading [74]. This is due to improvement of the triple phase boundary throughout the catalyst layer which results in higher electrochemically active Pt. Catalyst utilisation is termed as the ratio of electrochemical surface area to the physical surface area and is given by equation (2.4), where ECSA and A_{Phys} are the specific electrochemically active and physical surface areas of the catalyst, respectively:

$$U_{Pt} = \frac{ECSA}{A_{Phys}} X\, 100\% \quad (2.4)$$

Although this is now the standard procedure for PEMFC catalyst layers preparation, there are certain limitations of this method which restrict the catalyst utilisation to around 80%. This is due to the fact that the ionomer is not able to penetrate the micropores of the carbon support which are < 2nm diameter and thus the Pt present in those pores is isolated and does not take part in the catalyst reactions[75, 76]. This leads to significant losses in the active Pt surface area within the catalyst layer as can be seen in Figure 2.10. It is difficult to get complete ionomer coverage of Pt particles trapped within the mesopores (2-50 nm) using standard chemical route. If the concentration of ionomer is increased above 33 wt.% Nafion, reduced performance of the catalyst is observed. This is due to the blockage of gas diffusion pathways by excessive ionomer [77-80].

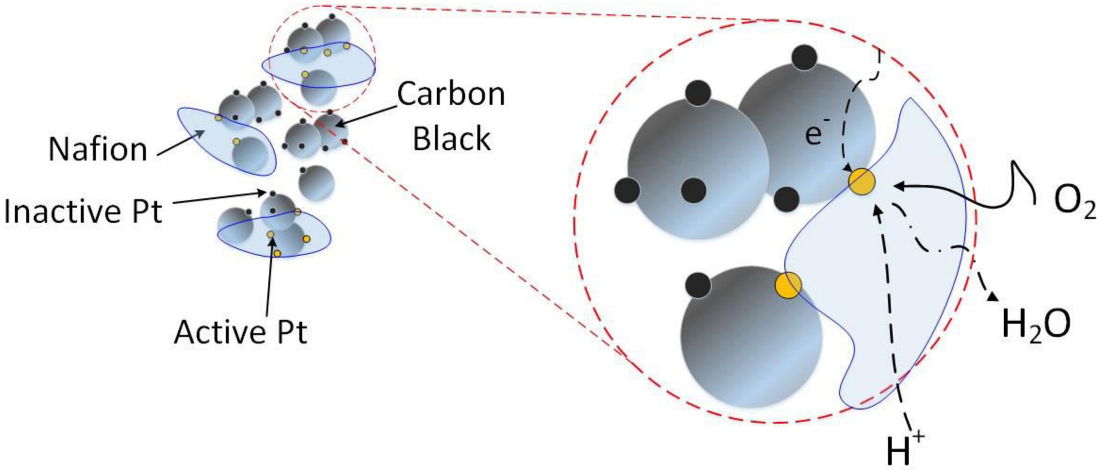

Figure 2.10: Schematic representations of a Pt/C catalyst ink, showing partial ionomer coverage resulting in inactive Pt particles. Triple phase boundary with the anodic and cathode reactions is also shown.

The earliest work reported in the field of ionomer stabilisation for the synthesis of electrocatalysts was carried out by Sarma *et al.*[70]. They used alcohol reduction method for the synthesis of Pt-Ru catalysts supported on Vulcan XC-72. The synthesis method reported the formation of dispersion of Vulcan XC-72 in a solution of H_2PtCl_6 and $RuCl_3$ and the mixture was reduced using MeOH under reflux at pH 11. 5 wt.% Nafion solution was added in the mixture prior to reduction step such that the Nafion: catalyst ratio was 3:1. From the TEM micrographs shown in Figure 2.11, a decrease in the average particle size of the catalysts from 5-7 nm (without Nafion) to 3-4 nm (with Nafion) was observed with the addition of Nafion.

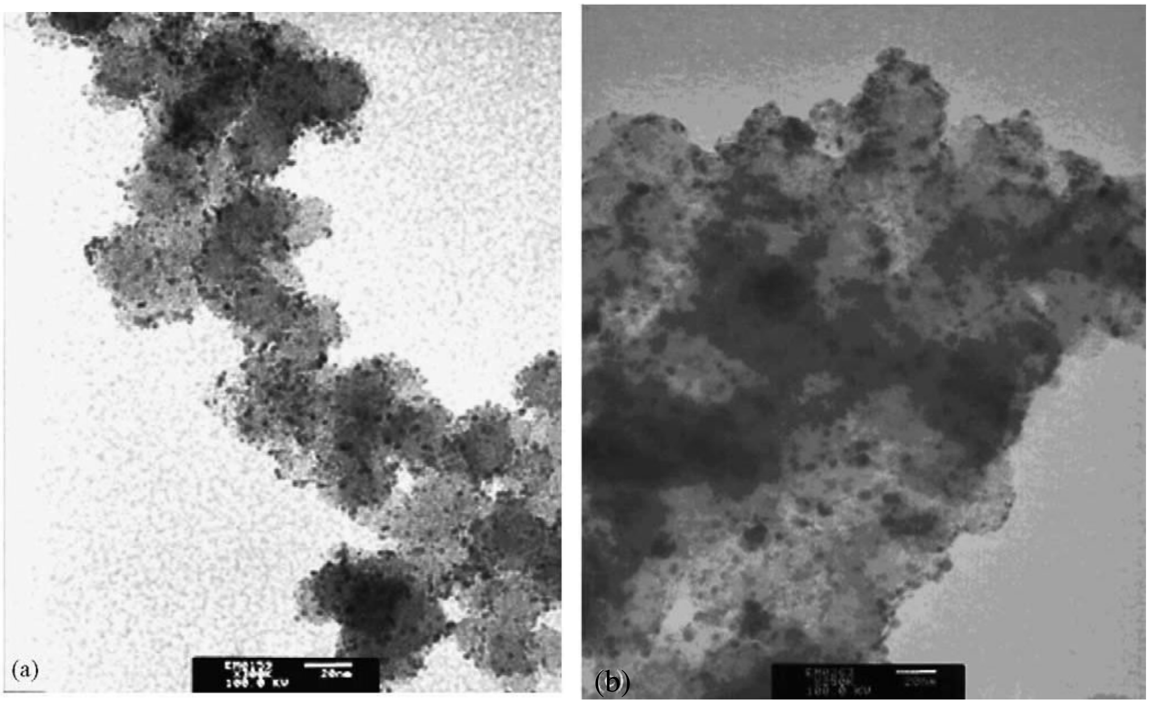

Figure 2.11: Pt-Ru/C electrocatalysts prepared by MeOH reduction a) in the presence of Nafion dispersion and b) without Nafion. Reproduced with permission from [70]

The working electrodes were prepared by depositing Nafion-stabilised Pt-Ru/C catalyst onto carbon cloth. They performed the electrochemical experiments in 0.5 M H_2SO_4 with varying concentrations of MeOH and catalytic activity towards methanol oxidation reaction (MOR) was measured as shown in figure 2.12. From the results obtained they concluded that the Nafion-stabilised catalyst has higher mass activity toward MOR than an E-Tek 40 wt.% commercial catalyst (MAs @ +0.4 V *vs* SHE were 1.82 and 0.55 Ag^{-1} respectively) at low methanol concentrations (5%). The same results were verified using the electrochemical impedance spectroscopy as the commercial catalysts showed higher specific resistance compared to the Nafion- stabilised catalysts. Thus, it can be concluded from the above results that with the addition of Nafion during synthesis, the particle size decreased and the catalytic activity of the Pt-Ru/C increased.

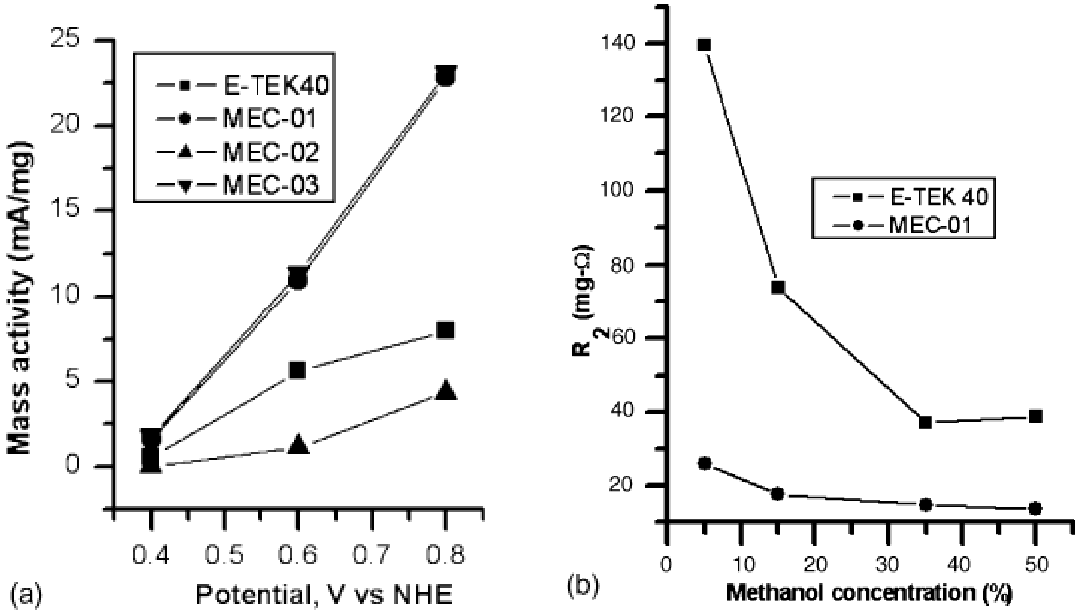

Figure 2.12: (a) Anode performance of Pt-Ru/C electrodes at 40 °C in 5% methanol, (b) Relationship between specific resistance and methanol concentration of E-Tek 40 and MEC-01 Pt-Ru/C catalysts. MEC-01, MEC-02, MEC-03 are Pt-Ru/C catalyst produced with different amount of reducing agent (15, 25, 35 ml respectively). Reproduced with permission from [70]

In 2010, a study on the Nafion stabilised Pt/C was reported by Curnick *et al.* [73], a previous work from our group. The authors prepared the Nafion-stabilised Pt/C by borohydride reduction method. Nafion dispersion was added to the aqueous H_2PtCl_6 in order to obtain Pt:Nafion ratio of 1:30 and then the mixture was stirred for 30 min before adding freshly prepared $NaBH_4$ solution. Figure 2.13 a shows the TEM image of the Nafion stabilised Pt/C. The particles were forming a loosely agglomerated network on the carbon support which could indicate coordination with the Nafion ionomer. The particle size was estimated to be around 7 nm. However, the E-Tek Pt/C showed well dispersed Pt particles on the carbon support with a particle size of around 2-3 nm (figure 2.13 b). They also reported >90% utilisation for the Nafion-Pt/C in comparison only 50% for commercial Pt/C. The main objective of this study was to investigate durability of the Nafion-Pt/C catalysts and the authors used accelerated catalyst degradation by performing linear sweep voltammetry between 0.05 V and 1.2 V at 25 mV/s at various rotation speeds (400-3000 rpm). The authors recorded the CV before and after this degradation test to study the electrochemical surface area variation. Figure 2.13 c and d shows the CV for Nafion Pt/C and E-Tek Pt/C before and after the degradation test. It can be seen from the curve that Nafion-Pt/C shows no change in the H_{upd} region and thus no change in the ECSA whereas Pt/C shows reduction in the H_{upd} region and thus loss in the ECSA which was calculated to be about 23%. The degradation of the E-Tek catalyst was attributed to the growth of the Pt particles during the cycling. The authors proposed a hypothesis that the enhanced durability for the Nafion-Pt/C is due to the novel morphology of the catalyst in which Nafion acts as protective agent which inhibits the dissolution of the particles as well as the sintering. However, this study does not include the standard accelerated durability testing which is potential cycling between 0.6 V- 1.2 V and thus the need for more analysis and testing to further the claims of better durability. Later on a study was also published about improved utilisation of the Pt catalyst by varying the amount of Nafion in the synthesis and almost 100% utilisation was observed[69].

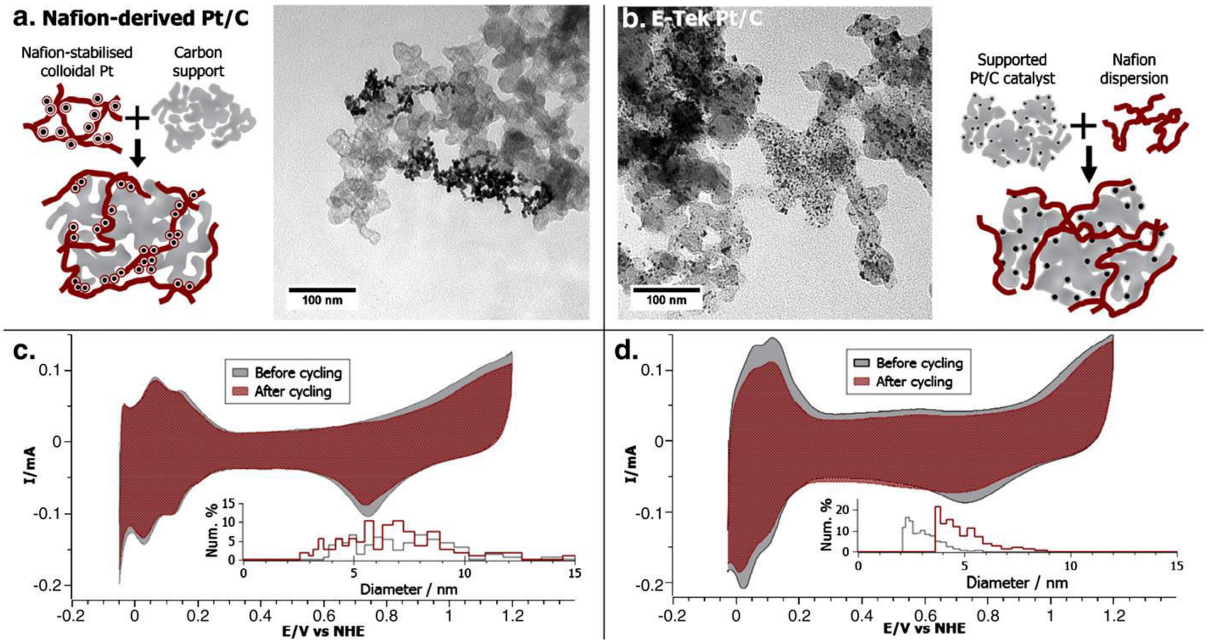

Figure 2.13: Schematic illustrations of catalyst layer morphology and TEM micrographs for (a) Nafion®-derived Pt/C catalyst and (b) E-Tek commercial 20 wt.% Pt/C. Cyclic voltammograms recorded at 25 mV/s in 0.1 M $HClO_4$ and at 298 K before and after electrochemical cycling and (inset) particle size distributions for c) Nafion®-derived Pt/C catalyst and d) E-Tek 20 wt.% Pt/C. Reproduced with permission from [73]

Various studies reported over past couple of years on the stabilisation of nanoparticles by ionomer are shown in table 2.2. However, these studies are limited to ex-situ testing of these nanoparticles and needs further in-situ testing in the real fuel cell environments for these catalysts to be successful.

Table: 2.2 List of various studies on ionomer stabilised electrocatalysts for fuel cells

System	Method	Ionomer used	Particle size	Comments	Ref
Pt/C	Borohydride reduction	Nafion	~6 nm	Increased durability of the Nafion stabilised Pt/C catalyst as compared to E-Tek (Pt/C)	[73]
Au@Pt/C	Seed mediated growth method	Nafion	4-6 nm	Au@Pt/C showed 6-9 times higher activity as compared to Pt/C	[81]
Pt/TiB_2	Colloidal route by adding NaOH and refluxing at pH-9	Nafion	3.4 nm	Pt/TiB_2 shows 4 times improved electrochemical stability as compared to Pt/C	[71]
Pt/C	Colloidal route by adding NaOH and refluxing at pH-8-10	Nafion	3.3 nm	Nafion-Pt/C shows 3 times improved durability as compared to Pt/C	[72]
Pt/C	Alcohol reduction	Nafion	2-4 nm	Nafion stabilised Pt/C showed higher tolerance to methanol than Pt/C	[82]
Pt-Ru/C	Alcohol reduction	Nafion	3-7 nm	Nafion addition improves the methanol electro oxidation activity compared to Pt/C.	[70]

2.6.2 Performance Enhancements of Catalysts by Alloying or Core-shell Structures

Figure 2.14 shows the oxygen reduction activities of various elemental catalysts as a function of oxygen binding energy on the surface of catalysts [83]. Pt has the highest activity towards ORR compared to all elemental catalysts and thus stands at peak of the so called 'Volcano' plot. The volcano plots are based on the Sabatier principle which states that a heterogeneous catalysts must bind reaction intermediates with sufficient strength to facilitate electron transfer but weakly enough to allow reaction products to desorb from the surface [84]. The optimum binding energy for oxygen to have the best activity is 1.8-2 eV. Pt with an oxygen binding energy of 1.57 eV is the closest to the optimum energy and thus forms the best electrocatalysts. However, this binding energy is still lower than the optimum binding energy and thus Pt still bind the oxygen rather strongly. The elements on the right side of Pt i.e. Ag and Au are poor catalysts as the binding energy of oxygen to them is weak and thus electron transfer is difficult. However, for the elements on the left side of the volcano plot (W, Mo, Fe, Co, Ru) make poor catalysts for the ORR as they bind oxygen species rather strongly (large, negative binding energy) ΔE_O [83]. So, there is to need to develop the catalysts with oxygen binding energies 0.3-0.4 eV more positive than that of Pt to improve the ORR kinetics, and current research is focussed on developing on bimetallic alloys of Pt[19-21, 85].

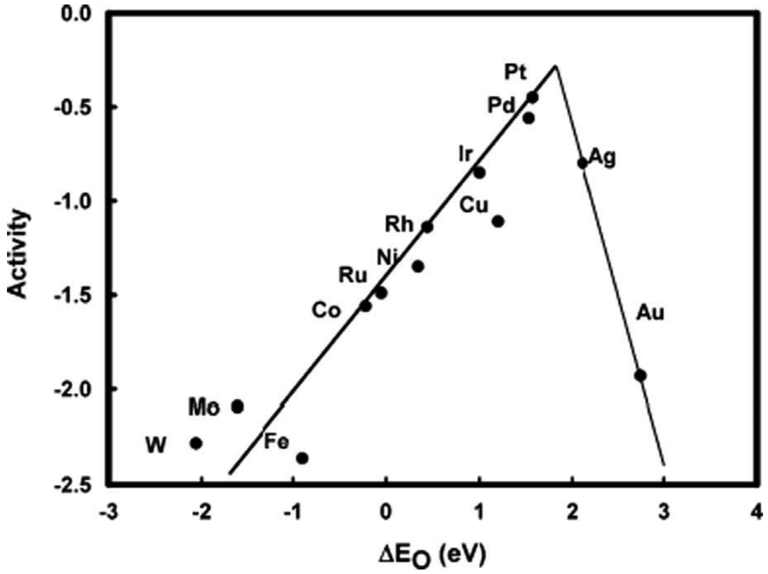

Figure 2.14: Trends in oxygen reduction activity as a function of the oxygen binding energy. Reproduced with permission from [83].

2.6.3 Pt-M alloys with Enhanced Activity and Durability

Greeley *et al.*[85] reported a computational study with Pt-skin structures having different ratio of the bimetallic species in order to study the relation of ORR activity to the binding energy for oxygen adsorbates. They also evaluated the thermodynamic stability of these alloys. Figure 2.15 (a) shows the volcano relationship of different Pt based alloys relative to Pt. It provides a good estimate of the catalytic activity of an alloy on the basis of oxygen adsorption energy. The figure shows both the experimental activity data as well as predicted activity (dashed line) using DFT calculations. The results suggested that ORR activity of an alloy will be better than Pt for a surface that binds oxygen more weakly than Pt (111) with a value from 0 to 0.4 eV. The optimum value can roughly be estimated to about 0.2 eV weaker than Pt. Figure 2.15 (b) showed a plot of the oxygen binding energy on a Pt/Pd skin surface relative to Pt (ΔE_O-ΔE_O^{Pt}) as a function of heat of formation of the bulk alloy (ΔE_{alloy}) that were calculated using DFT calculations. The calculations were done by varying the ratio of alloying elements from 25-50% in the second layer. The alloys which lie in the white shaded area are expected to show an improvement in the ORR activity. The alloys on the left side of the diagram (ΔE_{alloy}=-1.2 eV) are thermodynamically more stable and the stability decrease as we move right (towards ΔE_{alloy}=0.2eV). Thus, Pt_3Sc and Pt_3Y are expected to be the most thermodynamically stable – significantly more so than the 'traditional' Pt-M alloys (M=Ni, Co, Fe, Cr, Cu, Mo, Mn).

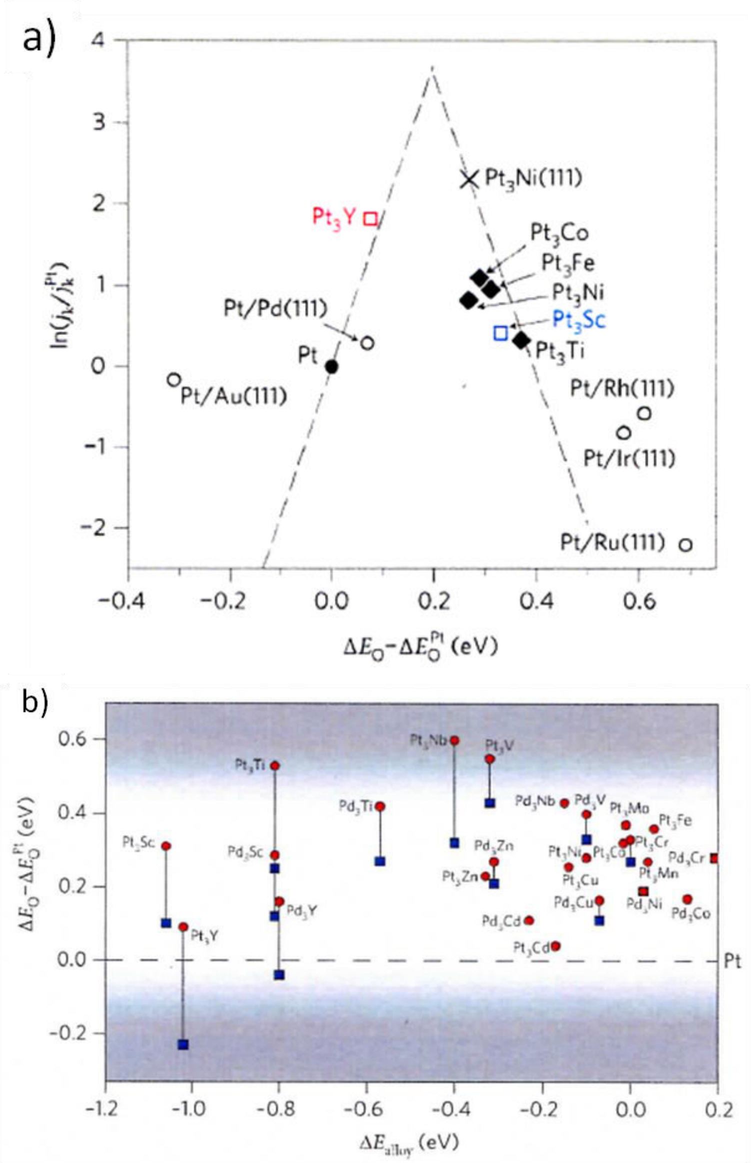

Figure 2.15: (a) Volcano relationships for ORR on Pt-based alloys between kinetic current density and oxygen adsorption energy (ΔE_O). All data are shown relative to Pt. (b) Oxygen binding energy of Pt as a function of alloying energy (red spots- 50%, blue spots -25% alloying element). Reproduced with permission from [85].

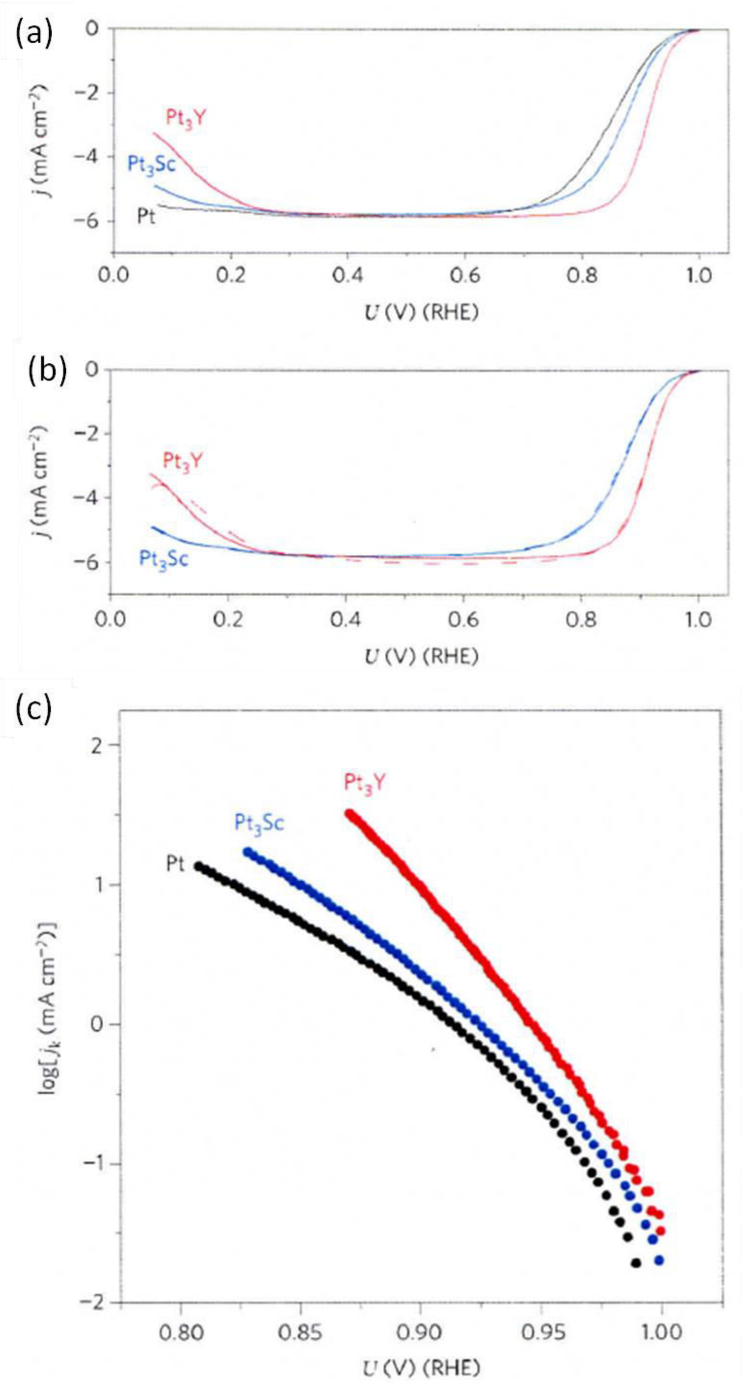

Figure 2.16: (a) linear sweep voltammograms for Pt and Pt_3Y, Pt_3Sc single-crystal surfaces obtained in RDE experiments at 23ºC, 1600 rpm in 0.1M $HClO_4$ at a scan rate of 20 mV/s; (b) anodic RDE sweeps comparing initial performance (solid lines) and that after 90 minutes of cycling (dashed lines); (c) Tafel plots of ORR specific activity for Pt and Pt_3Sc, Pt_3Y alloys. Reproduced with permission from [85].

Electrochemical experiments were carried out by Greeley *et al.* on the bulk alloys of Pt_3Y and Pt_3Sc, the results confirmed that Pt_3Y and Pt_3Sc offer 6-fold and 1.5-fold enhancements in ORR activity (relative to pure Pt at 0.9 V *vs* RHE) respectively (figure 2.16(c))[85]. Pt_3Y

reported the highest ORR activity and thus positioned close to the top of the volcano plot in Figure 2.15 (a). Also, they reported a positive shift in the onset potential for ORR in case of Pt_3Y and Pt_3Sc relative to Pt (figure 2.16 (a)) The stability of these alloys were also studied by potential cycling for 90 minutes from 1.0 to 0.05 V vs RHE at 20 mV/s and the results are represented by the dashed lines in Figure 2.16 (b). They showed no change in the performance after durability testing. However, it is possible that in nanocrystalline form the alloys may be prone to dissolution/leaching of base metals, and the authors acknowledge the need for in-situ PEMFC testing to confirm the expected stability. To date no results from in-situ testing have been reported for the above system.

Paulus *et al.* reported that Pt_3Co and Pt_3Ni catalysts in nanocrystalline and bulk form showed 1.5 to 2 fold activity enhancement in comparison to Pt/C catalyst [86, 87]. In another study, Stamenkovic *et al. [88]* reported that the rate of ORR on the Pt_3Ni (111) surface was around 10 and 90 times higher than on the Pt_3Ni (100) and commercial Pt/C, respectively (Figure 2.17). This suggested the dependence of catalytic activity on the crystallographic planes with (111) being highly active compared to (100) plane. This activity enhancement was attributed to the presence of tetrahedral particles for (111) planes compared to cubic particles for (100) plane providing superior specific activity.

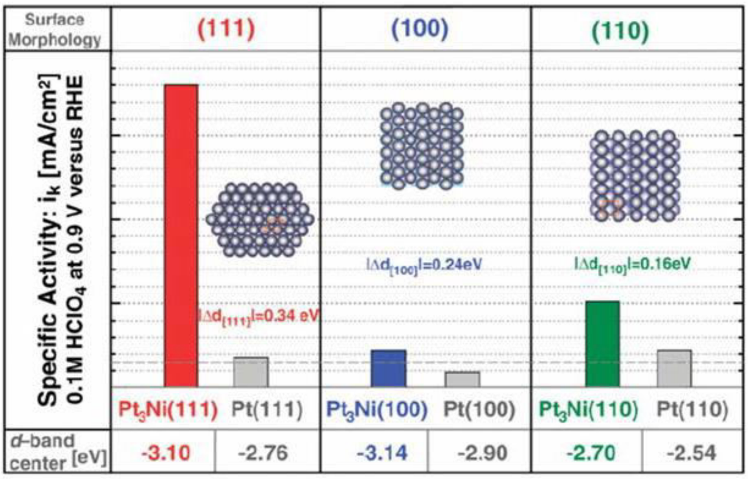

Figure 2.17: Relative rates of ORR on Pt_3Ni and pure Pt surfaces, along with corresponding d-band centre shifts in eV. Reproduced with permission from[88].

2.6.4 Studies on Pt-Cr Alloy Catalysts

Yang *et al.* [68] studied the ORR kinetics of Pt-Cr alloy catalysts supported on Vulcan XC-72 by porous rotating disk electrode in pure and methanol containing electrolytes. The Pt-Cr alloys were prepared using carbonyl route followed by heat treatment at 400-550 °C. The mean particle size for all the alloys was less than 5 nm and TEM micrographs showed the structure of these alloys (figure 2.18).

Figure 2.18 clearly shows that the alloy nanoparticles are well dispersed on the surface and possess a narrow particle size distribution. All alloys had a metal loading of about 20 wt.%. The authors reported that with the decrease in the Cr content of the alloy, the particle size increases from 3.1 nm for Pt-Cr (1:1) to about 3.3 nm and 3.4 nm for Pt-Cr (2:1) and Pt-Cr (3:1) respectively. However, if we take into account the standard deviation; all the alloys have same particle size.

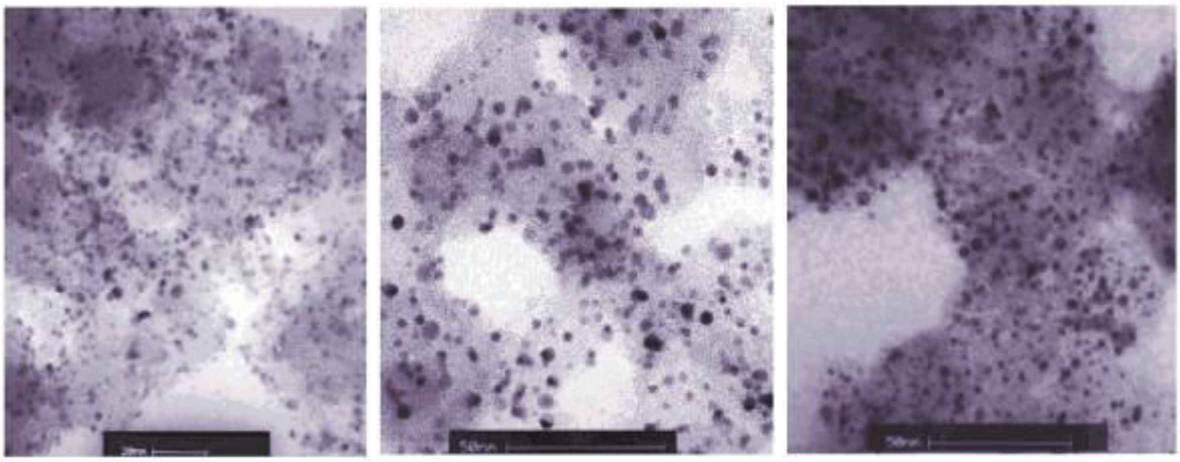

Figure 2.18: TEM images of the (a) Pt-Cr (3:1)/C (3.4±1.0 nm), (b) Pt-Cr (2:1)/C (3.3±1.2 nm), and (c) Pt-Cr (1:1)/C (3.1±1.3 nm) catalysts with 20 wt. % metal loading. Reproduced with permission from [68]

Figure 2.19 shows the mass activity (MA) and specific activity (SA) of the Pt-Cr alloys in comparison to the Pt/C catalyst in 0.5 M $HClO_4$ solution as reported by Yang *et al.*[68]. All the Pt-Cr alloys show a slight increase in the electrocatalytic activity for ORR in the absence of methanol and a significant increase in the presence of methanol as compared to the Pt/C catalyst. In case of Pt-Cr, the MA for ORR showed slight enhancement but a significant enhancement (of a factor of ~ 1.5-3) was observed in the case of SA when compared to that of Pt/C. This enhancement was attributed to the change in lattice parameters and the surface composition.

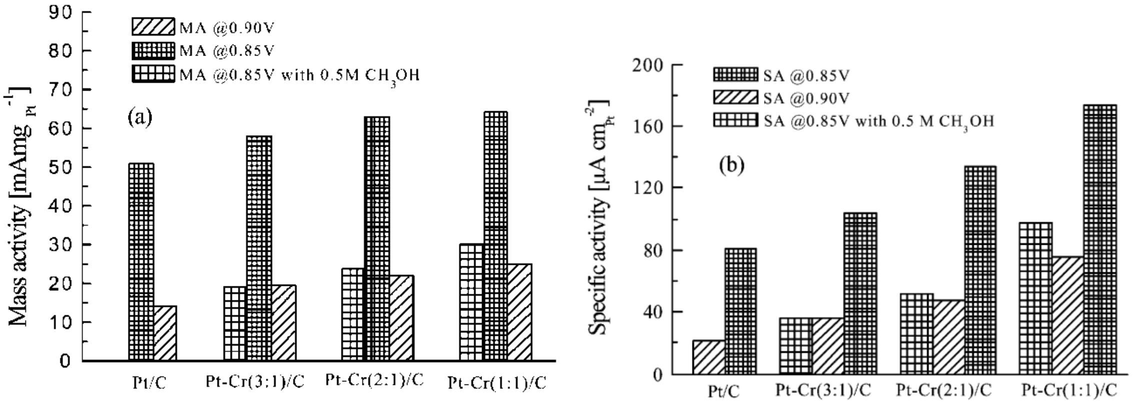

Figure 2.19: Histograms of the Mass Activity (MA) (a) and the Specific Activity (SA) (b) of the Pt-based electrocatalysts for the ORR in 0.5M $HClO_4$ solution. Reproduced with permission from [68]

Antolini *et al.* [89] studied the electrocatalytic activities of different alloys of Pt-Cr for ORR in 1 M H_2SO_4 and 1 M H_2SO_4/1–3 M CH_3OH solution using rotating disc electrode. A Pt-Cr alloy with atomic ratio of 3:1 was prepared by $NaBH_4$ reduction method[89]. Figure 2.20 (a) shows steady state polarization curve for all the alloys in pure H_2SO_4 and the plot is normalised by the Pt surface area. The overpotential for Pt_9Cr and PtCr/C at 0.1 mAcm^2 was ca.30-40 mV higher than pure platinum whereas for Pt_3Cr it was ca. 60 mV lower. The reason for the superior activity for Pt_3Cr/C was suggested to be a good combination of Pt-Pt bond distance and the Pt 5d band vacancy.

Figure 2.20(b) shows the Tafel plots obtained for ORR in 1 M H_2SO_4 solution for Pt/C and Pt-Cr/C catalysts that were normalised per mass of Pt in the catalyst layer. The plots were represented by plotting E vs. $| j*j_L/(j_L-j)|$, where j_L is the diffusion limiting current [89]. From the figure, it is clear that the Tafel slope is very similar between 52-56 mV/decade for Pt/C and Pt-Cr/C catalysts above 0.74V vs. RHE while below 0.74 V vs RHE, it is close to 120 mV/decade. Thus, the authors concluded that Tafel slope does not depend on the composition and structural parameters of electrocatalysts. This explains why there was no change in the reaction mechanism of ORR with the addition of Cr in the Pt.

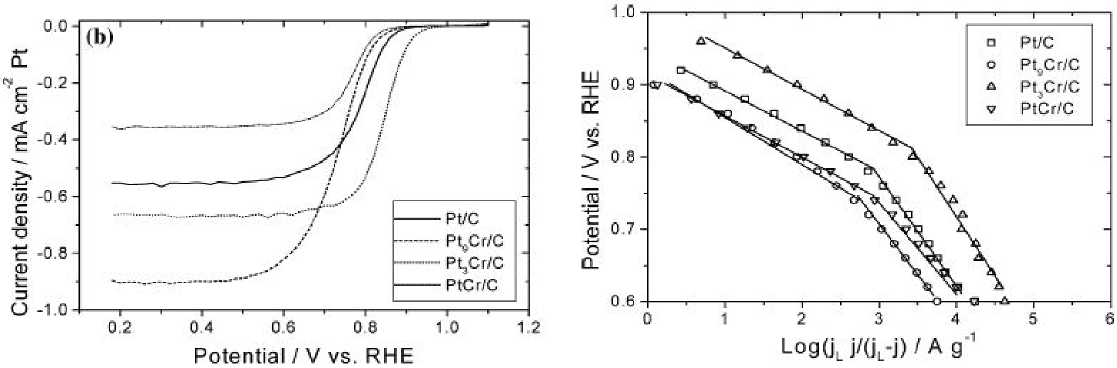

Figure 2.20: a) Steady-state polarization curves for O_2 reduction at 1600 rpm in 1M H_2SO_4 at 25°C for Pt/C and Pt–Cr/C electrocatalysts b) Tafel plots for the ORR in 1M H_2SO_4 (methanol free solution) on Pt/C and Pt–Cr/C catalysts. Reproduced with permission from [89]

Antolini *et al.* [89] also reported that the Pt_9Cr/C prepared by reduction with $NaBH_4$ exhibits the lowest activity for methanol oxidation and the highest activity for oxygen reduction in the presence of methanol, in comparison to commercial Pt/C, Pt_3Cr/C and PtCr/C electrocatalysts.

2.6.5 Core-shell Nanoparticles

Core-shell nanoparticles can be described as the particles which are synthesised to decrease the loading of a precious metal by forming a monolayer of shell on top of a core of less expensive metal and denoted by core@shell. Recently a lot of attention have been attracted by these structures due to improved activity in the field of fuel cells and the structures widely reported in literature are M@Pt (M= Cu, Co, Ni, Fe, etc.) [81, 90-96]. The materials used for these structures can range from metals, semiconductors dielectric materials depending on the final properties required. They are also receiving lot of attention due to the problems faced in the use of alloy catalysts i.e. dissolution of non-noble metal, this can be avoided by forming a shell of precious metal on top of the non-noble metal.

These structures can also give the flexibility of varying the molar ratio of the alloying element as well as the possibility of different three dimensional arrangements within the particles. The composition of these particles can be controlled by controlling the ratio of the precursors during chemical synthesis and also using methods like sputtering, electrodeposition. However, the arrangement of the structure is difficult to control and the different structures which can form during synthesis are shown in Figure 2.21. The aim of every researcher to have maximum Pt mass activity for ORR is obtain a structure of the arrangement (figure 2.21a) which has a monolayer of Pt on the non-noble metal core. However, the preparation conditions like temperature, pressure, concentration and chemical nature of precursors are the controlling factors for the final structure [97, 98].

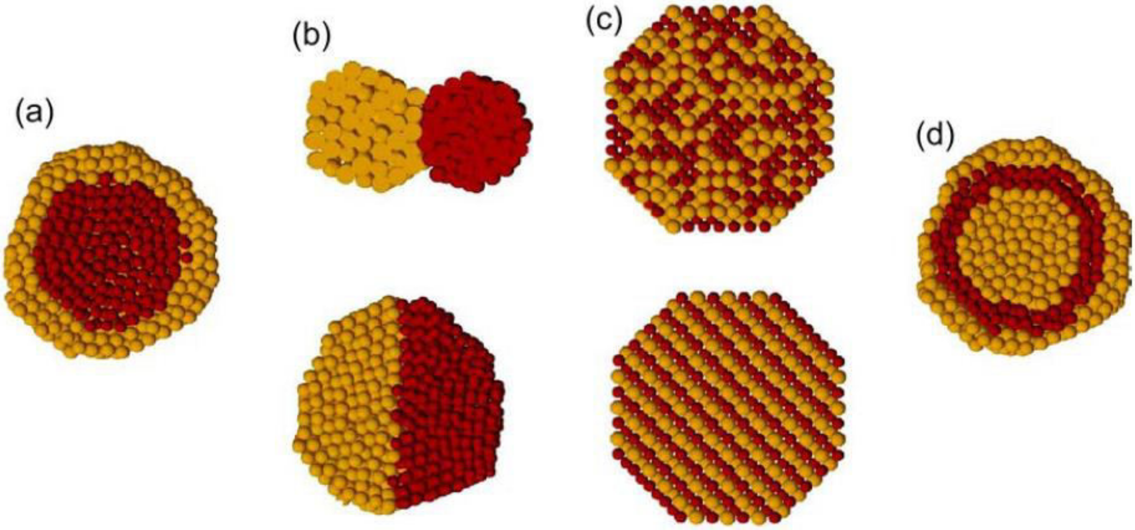

Figure 2.21: Possible combination fashions for two metals forming a bimetallic nanoparticle include (a) core-shell; (b) 'dipolar' or 'dumb-bell'; (c) intermixed random or ordered intermetallic alloys or (d) multi-layer 'onion-like' structures. Reproduced with permission from [97].

Chen *et al.*[99] studied the effect of shell coverage on the catalytic properties of the Ni@Pt/C core-shell nanoparticles. A two step reduction process was undertaken for the synthesis of Ni-Pt/C core-shell by modified polyol process. In the first step, Ni/C nanoparticles were synthesised by reducing Ni precursor using KBH_4 as reducing agent and oleic acid as capping agent. After the synthesis of Ni/C, Pt precursor was added dropwise to the solution and was reduced under continuous stirring. Different ratios of Pt:Ni were synthesised to study the coverage of Pt on Ni. Pt/Ni ratio of 3:10 was assumed to form a monolayer of Pt shell on Ni core assuming fcc Ni nanoparticles have cuboctahedral shapes and it was 2:10 for spherical shape.

Figure 2.22 shows the TEM images of different Ni-Pt/C catalysts synthesised with different ratios of Pt:Ni. It can be seen that the average particle size increased with the increase in the ratio of Pt:Ni. A narrow particle size distribution was observed for all the nanoparticles which showed a good control over the process. The authors have shown HRTEM images and suggested the formation of core-shell nanoparticles. However, from the images one cannot distinguish the Pt shell and thus it was still doubtful whether they have a core-shell structure or an alloy.

The authors performed electrochemical testing of the Ni-Pt/C core-shell nanoparticles in Ar-saturated H_2SO_4. Figure 2.23(a) shows the CV curves for the various Ni-Pt/C catalysts in comparison to Pt/C catalysts. The studies carried out by the authors confirmed that all the Ni-Pt catalysts have the similar desorption/adsorption behaviour of hydrogen and oxygen as of Pt/C which suggests the surface layer of Pt on these catalysts. From this behaviour, the authors confirmed the formation of core-shell nanoparticles as also suggested by HRTEM.

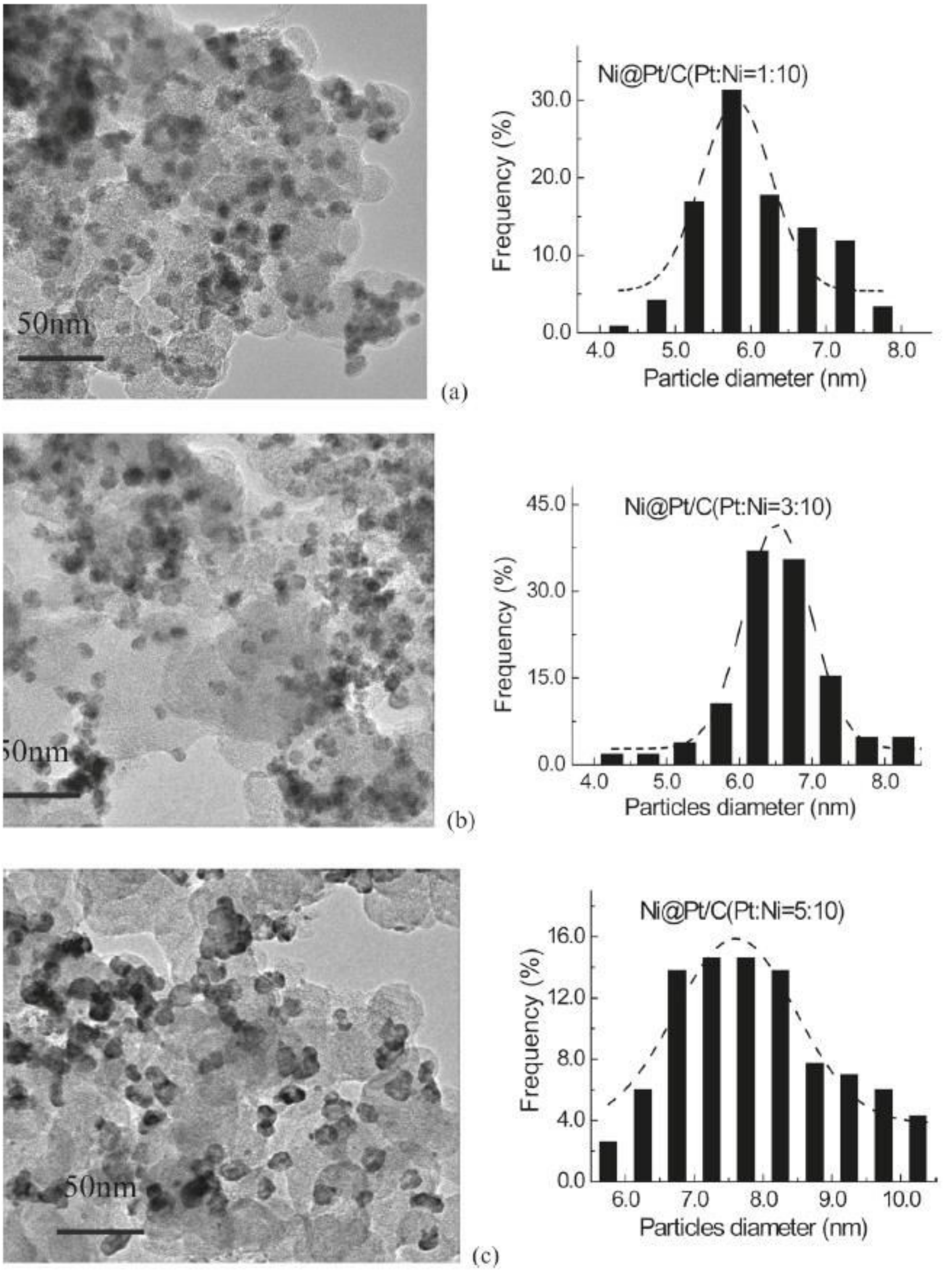

Figure 2.22: Representative TEM images (left) and the corresponding histograms of the particle size distribution (right) of the prepared Ni-Pt/C catalysts with Pt/Ni ratios of (a) 1:10, (b) 3:10, and (c) 5:10. The scale bars in TEM figures represent 50 nm. Reproduced with permission from [99].

Figure 2.23(b) shows the ORR linear sweep voltammograns of Ni-Pt/C catalysts with different ratios of Pt/Ni in O_2 saturated H_2SO_4. Figure 2.23(c, d) shows the specific area activities and mass activities of Pt, respectively. The specific activities were obtained by normalizing the kinetic current (I_k) by the electrochemical surface area of Pt and the Pt mass activities were obtained by normalizing I_k by the total mass of Pt on the electrode. Electrochemical testing carried out by the authors (figures 2.23 c and d), revealed that the specific area and mass activities were highest for the catalysts with Pt/Ni ratio of 3:10 and it goes down with a further increase in the Pt/Ni ratio. Thus it can be said that the monolayer of Pt shell offers the most optimised properties for ORR in the various Ni-Pt/C catalysts studied in the present case. The Pt surface coverage of either less or greater than a monolayer could result in a Pt surface which has less ORR activity and also does not give any benefits to the durability of the catalysts.

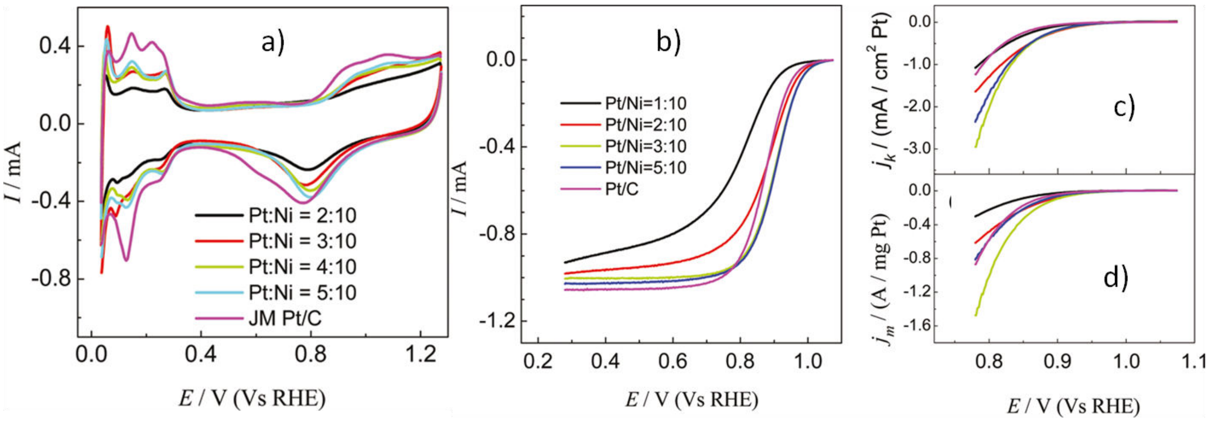

Figure 2.23: (a) CVs of the prepared Ni-Pt/C and the JM Pt/C catalysts in Ar-saturated 0.5 M H_2SO_4, (b) Representative ORR polarization curves for the prepared Ni-Pt/C and the JM Pt/C catalysts and the corresponding (c) specific area and (d) mass activities of Pt. Reproduced with permission from [99]

Various studies done on the Pt based alloys and core-shell nanoparticles over the course of past 4 years are summarised in table 2.3, highlighting the major advantages of the catalysts.

Table: 2.3 List of various studies on Pt based alloy and core-shell electrocatalysts for fuel cells

System	Method	Particle size (nm)	Comments	Ref.
Pd@Pt/C, PdPt/C	Borohydride reduction	~4-5	Pd@Pt/C showed better activity and 1.5 times higher current at 0.6V in MEA testing that Pt/C and better durability.	[100]
Co@Pt/C	Two step reduction with $NaBH_4$	3-5	Co@Pt/C (reduced) showed better catalytic activity. ECSA stays same after 130 h of operation suggesting better durability and stability.	[93]
PtCu/C, Pt(Cu)/C	Borohydride reduction	3-4	PtCu/C shows better activity towards ethanol reduction than Pt(Cu)/C and Pt/C.	[101]
$Ni_1@Pt_{0.067}/C$	Colloidal Template	6	$Ni_1@Pt_{0.067}/C$ shows higher catalytic activity towards ORR and MOR	[96]
Pd@Pt/C	Chemical reduction by ascorbic acid	4-6	Pd@Pt/C showed better mass activity and durability than Pt/C	[102]
Au@Pt/C	Successive reduction using sodium citrate and ascorbic acid	16-35	Au@Pt/C (1:2) showed higher electrocatalytic acitivity towards methanol oxidation in acidic media and better durability than Pt/C.	[103]
PtCo/C, PtPd/C	Impregnation and seeding	3-4	PtCo/C showed higher catalytic activity and stability than PtPd/C and Pt/C.	[104]
Ni@Pt/C	ZnO nanorod	3	Ni@Pt/C showed similar electrochemical area	[95]

	array-template assisted electrodeposition		and better catalytic activity and stability to methanol oxidation compared to Pt/C	
PtNi/C, PtCo/C, PtCu/C	Reduced under H_2/Ar at high temperature	4-12	$Pt_{75}Cu_{25}$/C reduced at 900 °C showed 2-3 times highest activity than Pt/C for same conditions.	[105]
$PtCO_3$/C, PtCo/C, Pt_3Co/C	Liquid precursor impregnation -freeze drying-annealing	3-4	Mass activities followed the trend in 0.1M $HClO_4$ $PtCo_3$ >Pt_3Co > PtCo >Pt. $PtCo_3$/C showed 3-5 fold increase compared to Pt/C	[106]
Au@Pt/C	Seed mediated growth method	3-5	Au@Pt/C showed higher activity towards ORR than Pt/C.	[94]
Ni@Pt/C	Colloidal chemical reduction using TBA as capping agent	7.5	Ni@Pt/C showed higher catalytic activity compared to Pt/C	[107]
PtCo/C, PtNi/C	Carbonyl route	~3	Increase methanol tolerance for PtNi/C and PtCo/C compared to Pt/C for ORR in acid media	[108]

Pt_3Co/Graphene, Pt_3Cr/Graphene	Ethylene glycol reduction	3-4	PtM/Graphene showed 3-4 times higher catalytic activity towards ORR than Pt/Graphene	[109]
Pt-Pd alloy and core-shell	Modified polyol method	5-10	Core-shell showed better electrocatalytic activity compared to the alloys	[110]
Cu@Pt/C	Two step reduction	5-6	Cu@Pt/C showed higher electrochemical surface area and ORR compared to Pt/C	[111]
Ni@Pt/C	Modified polyol method	6-8	A monolayer of Pt shell shows better activity and durability and more layers does not add any benefits.	[99]
Au@Pt/C	Seed mediated growth method	4-6	Au@Pt/C showed 6-9 times higher activity as compared to Pt/C	[81]
Pt_xNi_{1-x}/C	Organic solvothermal	5	Pt_xNi_{1-x}/C showed 3-4 fold increased catalytic activity compared to Pt/C.	[112]
Pt_xFe_{1-x}/C	Chemical reduction using oleylamine and oleic acid as stabilisers	2-4	Pt_xFe_{1-x}/C showed higher catalytic activity compared to Pt/C.	[113]
Cu@Pt/C	Galvanic displacement	2-8	Cu@Pt/C shows better catalytic activity towards ORR both per unit mass and per unit surface area	[91]

	of Cu by Pt^{4+} ions and leaching		compared to Pt/C	

2.6.6 Summary

From the discussion about the various studies ranging from using ionomer for stabilisation of the nanoparticles to alloy and core-shell nanoparticles, it can be seen that they all have advantages in either improving the catalytic properties or durability of the catalysts. The major advantages of using stabilisation by ionomer are 1) enhanced durability and 2) better utilisation of the catalyst. Alloys and core-shell lower the amount of Pt used and improves the catalytic activity from 2-10 times in various cases. The Pt-Cr system has been studied very less and thus lacks literature about possible use as catalyst in PEMFCs. However, the limited literature has shown positive results about improved catalytic activity for this system.

Even though the ionomer stabilisation has shown improved durability and utilisation, however there are no literature studies reporting the performance of these catalysts in actual fuel cell testing i.e. in-situ electrochemical testing. Alloys have shown improved catalytic activity but they are not stable i.e. dealloying of the catalyst takes place during the fuel cell operation over time. Thus, there is need for a system which can combine the advantages of alloying and ionomer stabilisation and overcome the disadvantage of dealloying during fuel cell operation. The current thesis is focussed on combining Nafion with Pt-Cr alloy system to form a catalyst which will be more catalytically active, stable and durable in the fuel cell environment.

References

1. Grove, W.R., in *Philosphical Magazine*1839.
2. Mond, L. and C. Langer, Proceedings of the Royal Society of London, 1889. **46**.
3. Ostwald, W., Zeitschrift fur Elektrotechnik und Electrochemie, 1894. **1**.
4. Jacques, W.W., Zeitschrift fur Elektrotechnik und Electrochemie, 1897. **4**.
5. Bacon, F.T., in *Fuel Cells*, G.J. Young, Editor. 1960, Reinhold Publishing: New York.
6. Appleby, A.J. and F.R. Foulkes, *Fuel Cell Handbook*. 1989, New York, USA: van Nostrand Reinhold.
7. Srinivas, S., *Fuel Cells: From Fundamentals to Applications*. 2006, United States of America: Springer Science + Business Media.
8. Vielstich, W., A. Lamm, and H.A. Gasteiger, eds. *Handbook of Fuel Cells: Fundamentals, Technology, Applications*. 2003, Wiley: New York.
9. Lamy, C., et al., *Recent advances in the development of direct alcohol fuel cells (DAFC).* Journal of Power Sources, 2002. **105**(2): p. 283-296.
10. Verma, A. and S. Basu, *Direct use of alcohols and sodium borohydride as fuel in an alkaline fuel cell.* Journal of Power Sources, 2005. **145**(2): p. 282-285.
11. Zhang, J., ed. *PEM Fuel Cell Electrocatalysts and Catalyst Layers : Fundamentals and Applications*. 2008, Springer.
12. Sinha, J. and Y. Yang, *Direct Hydrogen PEMFC Manufacturing Cost Estimation for Automotive Applications*, in *DOE Annual Merit Review Washington*2010.
13. Trongchuankij, W., K. Pruksathorn, and M. Hunsom, *Preparation of a high performance Pt–Co/C electrocatalyst for oxygen reduction in PEM fuel cell via a combined process of impregnation and seeding.* Applied Energy, 2011. **88**(3): p. 974-980.
14. Bar-On, I., R. Kirchain, and R. Roth, *Technical cost analysis for PEM fuel cells.* Journal of Power Sources, 2002. **109**: p. 71-75.
15. Gasteiger, H.A., et al., *Activity benchmarks and requirements for Pt, Pt-alloy, and non-Pt oxygen reduction catalysts for PEMFCs.* Applied Catalysis B: Environmental, 2005. **56**(1-2): p. 9-35.
16. Gasteiger, H.A., J.E. Panels, and S.G. Yan, *Dependence of PEM fuel cell performance on catalyst loading.* Journal of Power Sources, 2004. **127**(1-2): p. 162-171.
17. Chen, Z., et al., *A review on non-precious metal electrocatalysts for PEM fuel cells.* Energy & Environmental Science, 2011. **4**(9): p. 3167.
18. Bezerra, C., et al., *A review of Fe–N/C and Co–N/C catalysts for the oxygen reduction reaction.* Electrochimica Acta, 2008. **53**(15): p. 4937-4951.
19. Yu, W., M.D. Porosoff, and J.G. Chen, *Review of Pt-based bimetallic catalysis: from model surfaces to supported catalysts.* Chem Rev, 2012. **112**(11): p. 5780-817.
20. Wang, Y., et al., *A review of polymer electrolyte membrane fuel cells: Technology, applications, and needs on fundamental research.* Applied Energy, 2011. **88**(4): p. 981-1007.
21. Markovic, N.M., et al., *Oxygen Reduction Reaction on Pt and Pt Bimetallic Surfaces: A Selective Review.* Fuel Cells, 2001. **1**(2): p. 105-116.
22. Ehteshami, S.M.M. and S.H. Chan, *A review of electrocatalysts with enhanced CO tolerance and stability for polymer electrolyte membarane fuel cells.* Electrochimica Acta, 2013. **93**: p. 334-345.
23. Yu, X. and S. Ye, *Recent advances in activity and durability enhancement of Pt/C catalytic cathode in PEMFC: Part II: Degradation mechanism and durability enhancement of carbon supported platinum catalyst.* Journal of Power Sources, 2007. **172**(1): p. 145-154.
24. Antolini, E., J. Salgado, and E. Gonzalez, *The stability of Pt–M (M=first row transition metal) alloy catalysts and its effect on the activity in low temperature fuel cellsA literature review and tests on a Pt–Co catalyst.* Journal of Power Sources, 2006. **160**(2): p. 957-968.
25. Bing, Y., et al., *Nanostructured Pt-alloy electrocatalysts for PEM fuel cell oxygen reduction reaction.* Chemical Society Reviews, 2010. **39**(6): p. 2184.
26. Pylypenko, S., et al., *Non-platinum oxygen reduction electrocatalysts based on pyrolyzed transition metal macrocycles.* Electrochimica Acta, 2008. **53**: p. 7875-7883.

27. Easton, E.B., A. Bonakdarpour, and J.R. Dahn, *Fe-C-N Oxygen Reduction Catalysts Prepared by Combinatorial Sputter Deposition.* Electrochemical and Solid-State Letters, 2006. **9**(10): p. A463.
28. Hsueh, K.L., E.R. Gonzalez, and S. Srinivasan, *Electrolyte effects on oxygen reduction kinetics at platinum: A rotating ring-disc electrode analysis.* Electrochimica Acta, 1983. **28**(5): p. 691-697.
29. Bezerra, C., et al., *Novel carbon-supported Fe-N electrocatalysts synthesized through heat treatment of iron tripyridyl triazine complexes for the PEM fuel cell oxygen reduction reaction.* Electrochimica Acta, 2008. **53**(26): p. 7703-7710.
30. Bezerra, C., et al., *A review of heat-treatment effects on activity and stability of PEM fuel cell catalysts for oxygen reduction reaction.* Journal of Power Sources, 2007. **173**(2): p. 891-908.
31. Charreteur, F., et al., *Fe/N/C non-precious catalysts for PEM fuel cells: Influence of the structural parameters of pristine commercial carbon blacks on their activity for oxygen reduction.* Electrochimica Acta, 2008. **53**(6): p. 2925-2938.
32. Gan, T., et al., *Study on the membrane electrode assembly fabrication with carbon supported cobalt triethylenetetramine as cathode catalyst for proton exchange membrane fuel cell.* Journal of Power Sources, 2011. **196**(4): p. 1899-1903.
33. Garsuch, A., et al., *The effect of boron doping into Co-C-N and Fe-C-N electrocatalysts on the oxygen reduction reaction.* Electrochimica Acta, 2008. **53**(5): p. 2423-2429.
34. Lefèvre, M., *Fe-based catalysts for the reduction of oxygen in polymer electrolyte membrane fuel cell conditions: determination of the amount of peroxide released during electroreduction and its influence on the stability of the catalysts.* Electrochimica Acta, 2003. **48**(19): p. 2749-2760.
35. Lefevre, M. and J. Dodelet, *Fe-based electrocatalysts made with microporous pristine carbon black supports for the reduction of oxygen in PEM fuel cells.* Electrochimica Acta, 2008. **53**(28): p. 8269-8276.
36. Medard, C., et al., *Oxygen reduction by Fe-based catalysts in PEM fuel cell conditions: Activity and selectivity of the catalysts obtained with two Fe precursors and various carbon supports.* Electrochimica Acta, 2006. **51**(16): p. 3202-3213.
37. Meng, H., et al., *Iron porphyrin-based cathode catalysts for polymer electrolyte membrane fuel cells: Effect of NH3 and Ar mixtures as pyrolysis gases on catalytic activity and stability.* Electrochimica Acta, 2010. **55**(22): p. 6450-6461.
38. Schilling, T. and M. Bron, *Oxygen reduction at Fe–N-modified multi-walled carbon nanotubes in acidic electrolyte.* Electrochimica Acta, 2008. **53**(16): p. 5379-5385.
39. Antolini, E., et al., *Preparation of carbon supported binary Pt–M alloy catalysts (M=first row transition metals) by low/medium temperature methods.* Materials Chemistry and Physics, 2007. **101**(2-3): p. 395-403.
40. Antolini, E., J.R.C. Salgado, and E.R. Gonzalez, *Carbon supported Pt75M25 (M=Co, Ni) alloys as anode and cathode electrocatalysts for direct methanol fuel cells.* Journal of Electroanalytical Chemistry, 2005. **580**(1): p. 145-154.
41. Lopes, T., et al., *Carbon supported Pt–Co (3:1) alloy as improved cathode electrocatalyst for direct ethanol fuel cells.* Journal of Power Sources, 2007. **164**(1): p. 111-114.
42. Salgado, J., E. Antolini, and E. Gonzalez, *Carbon supported PtCo electrocatalyst prepared by the formic acid method for the oxygen reduction reaction in polymer electrolyte fuel cells.* Journal of Power Sources, 2005. **141**(1): p. 13-18.
43. Salgado, J., E. Antolini, and E. Gonzalez, *Carbon supported Pt–Co alloys as methanol-resistant oxygen-reduction electrocatalysts for direct methanol fuel cells.* Applied Catalysis B: Environmental, 2005. **57**(4): p. 283-290.
44. Salgado, J.R.C., E. Antolini, and E.R. Gonzalez, *Pt-Co/C Electrocatalysts for Oxygen Reduction in H_2/O_2 PEMFCs Synthesized by Borohydride Method.* Journal of The Electrochemical Society, 2004. **151**(12): p. A2143.
45. Zignani, S.C., E. Antolini, and E.R. Gonzalez, *Evaluation of the stability and durability of Pt and Pt–Co/C catalysts for polymer electrolyte membrane fuel cells.* Journal of Power Sources, 2008. **182**(1): p. 83-90.

46. Min, M.K., et al., *Particle size and alloying effects of Pt-based alloy catalysts for fuel cell applications.* Electrochimica Acta, 2000. **45**(25-26): p. 4211-4217.
47. Travitsky, N., et al., *Pt-, PtNi- and PtCo-supported catalysts for oxygen reduction in PEM fuel cells.* Journal of Power Sources, 2006. **161**(2): p. 782-789.
48. Xiong, L., A.M. Kannan, and A. Manthiram, *Pt–M (M=Fe, Co, Ni and Cu) electrocatalysts synthesized by an aqueous route for proton exchange membrane fuel cells.* Electrochemistry Communications, 2002. **4**: p. 898-903.
49. Xiong, L. and A. Manthiram, *Effect of Atomic Ordering on the Catalytic Activity of Carbon Supported PtM (M=Fe, Co, Ni, and Cu) Alloys for Oxygen Reduction in PEMFCs.* Journal of The Electrochemical Society, 2005. **152**(4): p. A697.
50. Mani, P., R. Srivastava, and P. Strasser, *Dealloyed binary PtM3 (M=Cu, Co, Ni) and ternary PtNi3M (M=Cu, Co, Fe, Cr) electrocatalysts for the oxygen reduction reaction: Performance in polymer electrolyte membrane fuel cells.* Journal of Power Sources, 2011. **196**(2): p. 666-673.
51. Ramossanchez, G., H. Yeemadeira, and O. Solorzaferia, *PdNi electrocatalyst for oxygen reduction in acid media.* International Journal of Hydrogen Energy, 2008. **33**(13): p. 3596-3600.
52. Zignani, S.C., E. Antolini, and E.R. Gonzalez, *Stability of Pt–Ni/C (1:1) and Pt/C electrocatalysts as cathode materials for polymer electrolyte fuel cells: Effect of ageing tests.* Journal of Power Sources, 2009. **191**(2): p. 344-350.
53. Lizcano-Valbuena, W.H., et al., *Catalysts for DMFC: relation between morphology and electrochemical performance.* Electrochimica Acta, 2003. **48**: p. 3869-3878.
54. Guo, J., et al., *Carbon nanofibers supported Pt–Ru electrocatalysts for direct methanol fuel cells.* Carbon, 2006. **44**(1): p. 152-157.
55. Cooper, J. and P. McGinn, *Combinatorial screening of fuel cell cathode catalyst compositions.* Applied Surface Science, 2007. **254**(3): p. 662-668.
56. Cooper, J. and P. McGinn, *Combinatorial screening of thin film electrocatalysts for a direct methanol fuel cell anode.* Journal of Power Sources, 2006. **163**(1): p. 330-338.
57. Kaplan, D., et al., *Study of core–shell platinum-based catalyst for methanol and ethylene glycol oxidation.* Journal of Power Sources, 2011. **196**(3): p. 1078-1083.
58. Fang, B., et al., *Proton exchange membrane fuel cells with nanoengineered AuPt catalysts at the cathode.* Journal of Power Sources, 2011. **196**(2): p. 659-665.
59. Luo, J., et al., *Activity-composition correlation of AuPt alloy nanoparticle catalysts in electrocatalytic reduction of oxygen.* Electrochemistry Communications, 2006. **8**(4): p. 581-587.
60. Mott, D., et al., *Nanocrystal and surface alloy properties of bimetallic Gold-Platinum nanoparticles.* Nanoscale Research Letters, 2006. **2**(1): p. 12-16.
61. Wanjala, B.N., et al., *Nanoscale Alloying, Phase-Segregation, and Core−Shell Evolution of Gold−Platinum Nanoparticles and Their Electrocatalytic Effect on Oxygen Reduction Reaction.* Chemistry of Materials, 2010. **22**(14): p. 4282-4294.
62. Thanasilp, S. and M. Hunsom, *Effect of MEA fabrication techniques on the cell performance of Pt–Pd/C electrocatalyst for oxygen reduction in PEM fuel cell.* Fuel, 2010. **89**(12): p. 3847-3852.
63. Thanasilp, S. and M. Hunsom, *Effect of Pt: Pd atomic ratio in Pt–Pd/C electrocatalyst-coated membrane on the electrocatalytic activity of ORR in PEM fuel cells.* Renewable Energy, 2011. **36**(6): p. 1795-1801.
64. Thanasilp, S. and M. Hunsom, *Preparation of a high-performance Pt–Pd/C-electrocatalyst-coated membrane for ORR in PEM fuel cells via a combined process of impregnation and seeding: Effect of electrocatalyst loading on carbon support.* Electrochimica Acta, 2011. **56**(3): p. 1164-1171.
65. Salvador-Pascual, J.J., et al., *Low Pt content on the Pd45Pt5Sn50 cathode catalyst for PEM fuel cells.* Journal of Power Sources, 2010. **195**(11): p. 3374-3379.
66. Beard, K.D., J.W. Van Zee, and J.R. Monnier, *Preparation of carbon-supported Pt–Pd electrocatalysts with improved physical properties using electroless deposition methods.* Applied Catalysis B: Environmental, 2009. **88**(1-2): p. 185-193.

67. Seo, A., et al., *Performance and stability of Pt-based ternary alloy catalysts for PEMFC.* Electrochimica Acta, 2006. **52**: p. 1603-1611.

68. Yang, H., et al., *Tailoring, Structure, and Activity of Carbon-Supported Nanosized Pt−Cr Alloy Electrocatalysts for Oxygen Reduction in Pure and Methanol-Containing Electrolytes.* The Journal of Physical Chemistry B, 2004. **108**(6): p. 1938-1947.

69. Curnick, O.J., B.G. Pollet, and P.M. Mendes, *Nafion®-stabilised Pt/C electrocatalysts with efficient catalyst layer ionomer distribution for proton exchange membrane fuel cells.* RSC Advances, 2012. **2**(22): p. 8368.

70. Sarma, L.S., et al., *Carbon-supported Pt–Ru catalysts prepared by the Nafion stabilized alcohol-reduction method for application in direct methanol fuel cells.* Journal of Power Sources, 2005. **139**(1-2): p. 44-54.

71. Yin, S., et al., *A highly stable catalyst for PEM fuel cell based on durable titanium diboride support and polymer stabilization.* Applied Catalysis B: Environmental, 2010. **93**(3-4): p. 233-240.

72. Cheng, N., et al., *Improved lifetime of PEM fuel cell catalysts through polymer stabilization.* Electrochemistry Communications, 2009. **11**(8): p. 1610-1614.

73. Curnick, O.J., P.M. Mendes, and B.G. Pollet, *Enhanced durability of a Pt/C electrocatalyst derived from Nafion-stabilised colloidal platinum nanoparticles.* Electrochemistry Communications, 2010. **12**(8): p. 1017-1020.

74. Srinivasan, S., et al., *Advances in solid polymer electrolyte fuel cell technology with low platinum loading electrodes.* Journal of Power Sources, 1988. **22**(3-4): p. 359-375.

75. Malek, K., et al., *Self-Organization in Catalyst Layers of Polymer Electrolyte Fuel Cells.* Journal of Physical Chemistry C, 2007. **111**(36): p. 13627-13634.

76. Ignaszak, A., S. Ye, and E.d. Gyenge, *A Study of the Catalytic Interface for O2Electroreduction on Pt: The Interaction between Carbon Support Meso/Microstructure and Ionomer (Nafion) Distribution.* The Journal of Physical Chemistry C, 2009. **113**(1): p. 298-307.

77. Zhang, J.Z., K. Hongsirikarn, and J.G. Goodwin, *Effect and siting of Nafion® in a Pt/C proton exchange membrane fuel cell catalyst.* Journal of Power Sources, 2011. **196**(19): p. 7957-7966.

78. Tabe, Y., et al., *Effects of Cathode Catalyst Layer Structure and Properties Dominating Polymer Electrolyte Fuel Cell Performance.* Journal of The Electrochemical Society, 2011. **158**(10): p. B1246.

79. Friedmann, R. and T. Van Nguyen, *Optimization of the Microstructure of the Cathode Catalyst Layer of a PEMFC for Two-Phase Flow.* Journal of The Electrochemical Society, 2010. **157**(2): p. B260.

80. Esparbé, I., et al., *Structure and electrocatalytic performance of carbon-supported platinum nanoparticles.* Journal of Power Sources, 2009. **190**(2): p. 201-209.

81. Cheng, N., et al., *Highly active Pt@Au nanoparticles encapsulated in perfluorosulfonic acid for the reduction of oxygen.* Chem Commun (Camb), 2011. **47**(48): p. 12792-4.

82. Liu, Z., Z.Q. Tian, and S.P. Jiang, *Synthesis and characterization of Nafion-stabilized Pt nanoparticles for polymer electrolyte fuel cells.* Electrochimica Acta, 2006. **52**(3): p. 1213-1220.

83. Nørskov, J.K., et al., *Origin of the Overpotential for Oxygen Reduction at a Fuel-Cell Cathode.* The Journal of Physical Chemistry B, 2004. **108**(46): p. 17886-17892.

84. Nørskov, J., et al., *Universality in Heterogeneous Catalysis.* Journal of Catalysis, 2002. **209**(2): p. 275-278.

85. Greeley, J., et al., *Alloys of platinum and early transition metals as oxygen reduction electrocatalysts.* Nat Chem, 2009. **1**(7): p. 552-6.

86. Paulus, U.A., et al., *Oxygen reduction on high surface area Pt-based alloy catalysts in comparison to well defined smooth bulk alloy electrodes.* Electrochimica Acta, 2002. **47**(22-23): p. 3787-3798.

87. Paulus, U.A., et al., *Oxygen Reduction on Carbon-Supported Pt−Ni and Pt−Co Alloy Catalysts.* The Journal of Physical Chemistry B, 2002. **106**(16): p. 4181-4191.

88. Stamenkovic, V.R., et al., *Improved oxygen reduction activity on Pt3Ni(111) via increased surface site availability.* Science, 2007. **315**(5811): p. 493-7.
89. Antolini, E., et al., *Carbon supported Pt–Cr alloys as oxygen-reduction catalysts for direct methanol fuel cells.* Journal of Applied Electrochemistry, 2006. **36**(3): p. 355-362.
90. Chen, Y.M., et al., *Ni@Pt core-shell nanoparticles: Synthesis, structural and electrochemical properties.* Journal of Physical Chemistry C, 2008. **112**(5): p. 1645-1649.
91. Sarkar, A. and A. Manthiram, *Synthesis of Pt@Cu Core-Shell Nanoparticles by Galvanic Displacement of Cu by Pt4+ Ions and Their Application as Electrocatalysts for Oxygen Reduction Reaction in Fuel Cells.* Journal of Physical Chemistry C, 2010. **114**(10): p. 4725-4732.
92. Zhang, X.B., et al., *Magnetically recyclable Fe@Pt core-shell nanoparticles and their use as electrocatalysts for ammonia borane oxidation: the role of crystallinity of the core.* J Am Chem Soc, 2009. **131**(8): p. 2778-9.
93. Lin, R., et al., *Synthesis and application of core–shell Co@Pt/C electrocatalysts for proton exchange membrane fuel cells.* Journal of Power Sources, 2013. **223**: p. 190-198.
94. Lin, R., et al., *Investigation of Au@Pt/C electro-catalysts for oxygen reduction reaction.* Electrochimica Acta, 2012. **62**: p. 263-268.
95. Ding, L.X., et al., *Porous Ni@Pt core-shell nanotube array electrocatalyst with high activity and stability for methanol oxidation.* Chemistry, 2012. **18**(27): p. 8386-91.
96. Duan, D., et al., *Electrocatalytic performance of Nicore@Ptshell/C core–shell nanoparticle with the Pt in nanoshell.* International Journal of Hydrogen Energy, 2013. **38**(33): p. 14261-14268.
97. Ferrando, R., J. Jellinek, and R.L. Johnston, *Nanoalloys: from theory to applications of alloy clusters and nanoparticles.* Chem Rev, 2008. **108**(3): p. 845-910.
98. Carbone, L. and P.D. Cozzoli, *Colloidal heterostructured nanocrystals: Synthesis and growth mechanisms.* Nano Today, 2010. **5**(5): p. 449-493.
99. Chen, Y., et al., *Ni–Pt Core–Shell Nanoparticles as Oxygen Reduction Electrocatalysts: Effect of Pt Shell Coverage.* The Journal of Physical Chemistry C, 2011. **115**(49): p. 24073-24079.
100. Lim, Y., et al., *One-step synthesis of carbon-supported Pd@Pt/C core-shell nanoparticles as oxygen reduction electrocatalysts and their enhanced activity and stability.* Nanoscale, 2014.
101. Ammam, M. and E.B. Easton, *PtCu/C and Pt(Cu)/C catalysts: Synthesis, characterization and catalytic activity towards ethanol electrooxidation.* Journal of Power Sources, 2013. **222**(0): p. 79-87.
102. Zhang, G., et al., *Core–shell Pt modified Pd/C as an active and durable electrocatalyst for the oxygen reduction reaction in PEMFCs.* Applied Catalysis B: Environmental, 2013. **132-133**: p. 183-194.
103. Feng, R., M. Li, and J. Liu, *Synthesis of core–shell Au@Pt nanoparticles supported on Vulcan XC-72 carbon and their electrocatalytic activities for methanol oxidation.* Colloids and Surfaces A: Physicochemical and Engineering Aspects, 2012. **406**: p. 6-12.
104. Termpornvithit, C., N. Chewasatn, and M. Hunsom, *Stability of Pt–Co/C and Pt–Pd/C based oxygen reduction reaction electrocatalysts prepared at a low temperature by a combined impregnation and seeding process in PEM fuel cells.* Journal of Applied Electrochemistry, 2012. **42**(3): p. 169-178.
105. Jayasayee, K., et al., *Oxygen reduction reaction (ORR) activity and durability of carbon supported PtM (Co, Ni, Cu) alloys: Influence of particle size and non-noble metals.* Applied Catalysis B: Environmental, 2012. **111-112**: p. 515-526.
106. Oezaslan, M., F.d.r. Hasché, and P. Strasser, *Oxygen Electroreduction on PtCo3, PtCo and Pt3Co Alloy Nanoparticles for Alkaline and Acidic PEM Fuel Cells.* Journal of The Electrochemical Society, 2012. **159**(4): p. B394.
107. Godínez-Salomón, F., M. Hallen-López, and O. Solorza-Feria, *Enhanced electroactivity for the oxygen reduction on Ni@Pt core-shell nanocatalysts.* International Journal of Hydrogen Energy, 2012. **37**(19): p. 14902-14910.

108. Favry, E., et al., *Synthesis, electrochemical characterization and molecular dynamics studies of surface segregation of platinum nano-alloy electrocatalysts.* Phys Chem Chem Phys, 2011. **13**(20): p. 9201-8.

109. Rao, C.V., et al., *Synthesis and electrocatalytic oxygen reduction activity of graphene-supported Pt3Co and Pt3Cr alloy nanoparticles.* Carbon, 2011. **49**(3): p. 931-936.

110. Long, N.V., et al., *Synthesis and characterization of Pt–Pd alloy and core-shell bimetallic nanoparticles for direct methanol fuel cells (DMFCs): Enhanced electrocatalytic properties of well-shaped core-shell morphologies and nanostructures.* International Journal of Hydrogen Energy, 2011. **36**(14): p. 8478-8491.

111. Zhu, H., X. Li, and F. Wang, *Synthesis and characterization of Cu@Pt/C core-shell structured catalysts for proton exchange membrane fuel cell.* International Journal of Hydrogen Energy, 2011. **36**(15): p. 9151-9154.

112. Wang, C., et al., *Correlation Between Surface Chemistry and Electrocatalytic Properties of Monodisperse PtxNi1-x Nanoparticles.* Advanced Functional Materials, 2011. **21**(1): p. 147-152.

113. Lai, F.J., et al., *Tunable properties of PtxFe1-x electrocatalysts and their catalytic activity towards the oxygen reduction reaction.* Nanoscale, 2010. **2**(4): p. 573-81.

Chapter 3
Materials, Methods and Techniques

The previous chapter explained the various current electrocatalysts and the need for research in finding new catalysts to overcome the barrier for commercialisation of low temperature fuel cells (i.e. polymer electrolyte membrane fuel cells – PEMFCs). This chapter will detail the methods used for the synthesis of Pt-Cr nanoparticles in the present study. It is divided into two sections i.e. 1) Pt-Cr alloy and 2) Pt-Cr core-shell nanoparticles. The nanoparticles were characterised using different techniques to study the properties ranging from particle size, shape, composition and purity. These techniques include Thermogravimetric Analysis (TGA), Transmission Electron Microscopy (TEM), X-ray Diffraction (XRD) and X-ray Photoelectron Spectroscopy (XPS). The nanoparticles were supported on Vulcan carbon to carry out the electrochemical testing. Electrochemical testing was divided into two parts: ex-situ and in-situ to study the catalytic behaviour of these nanoparticles for use in a PEMFC.

3.1 Synthesis and Purification of Pt-Cr Alloy Nanoparticles

In the present study, the nanoparticles were synthesised by colloidal route as it gives better control over the particle size, homogeneity of size and composition in comparison with high temperature routes(such as polyol method, impregnation and reduction, reduction and annealing)[1-10]. Borohydride reduction method has been widely used for the synthesis of nanoparticles of Pt[11-13], Pd[14] and alloys of Pt-Pd[15], Pt-Ru[16], Pt-Ni[12, 17] Pt-Co[3, 17-21], Pd-Ni[22]. The main advantage of this technique was that the whole process takes place at ambient temperature and $NaBH_4$ is safer to handle as compared to other strong reducing agents like hydrazine, $LiBH_4$, lithium triethylborohydride. Even though, the standard reduction potential of Cr is -0.74 V which is more negative than hydrogen reduction potential, it can still be reduced at room temperature by the use of borohydrides as they are among the most effective reducing agent due to the presence of hydrogen with negative charge[23]. The aim was to produce nanoparticles of Pt-Cr alloy using wet chemical synthesis at room temperature to

1) avoid growth of nanoparticles of only Pt or Cr,
2) avoid use of highly sensitive and expensive equipment
3) achieve better control over the reaction at low temperature

Nafion® stabilised colloidal Pt has been successfully synthesised using chemical reduction of $PtCl_6^{2-}$ [13, 24]. The same method has been modified in this study to synthesise the Pt-Cr alloy nanoparticles. Before the synthesis, the glassware wass cleaned using aqua regia (3:1 HCl: HNO_3) in order to remove any impurities present. Following this the glassware was rinsed thoroughly with UHQ (millipore) water. Two methods were used for the Pt-Cr alloy synthesis:

1. Borohydride reduction method-1 with water as solvent
2. Borohydride reduction method-2 with ethanol as solvent

3.1.1 Borohydride Reduction Method-1 with Water as Solvent

Aqueous precursors of Pt ($PtCl_6^{2-}$) (Sigma-Aldrich) and Cr ($CrCl_3$) (Sigma-Aldrich) were mixed together for 10 min in a round-bottom flask with continuous stirring at 500 rpm. Nafion® dispersion (10 %) (Dupont) was added to the solution to achieve different metal:

Nafion® ratios, ranging from 1:10, 1:20, 1:30 and 1:50. As reported by Curnick *et al.* [13] and also during our initial characterisation, 1:30 metal: Nafion® ratio gives better coverage and stabilisation of the nanoparticles and thus this was chosen as the optimised ratio for all syntheses. The solution was stirred for 30 min at 500 rpm before freshly prepared $NaBH_4$ (Sigma-Aldrich) solution (>4 times the stoichiometric requirement) was added to the precursor-Nafion® mix. This resulted in the instant change of colour from green to black, confirming the reduction of the precursors. The reaction mixture was centrifuged (Sigma 3K 30, 4 °C, 2000 rpm) to remove the excess of Nafion® using acetone as the precipitation solvent. Following this, the product was redispersed using ultrasonication in a mixture of 1:4 v/v water/acetone and centrifuged several times. Figure 3.1 (a) shows the flowchart with different steps involved in the synthesis. The results showed formation of Pt nanoparticles with traces of Cr only and no formation of alloy and thus the need for another method. The detailed analysis of these nanoparticles is reported in next chapter.

3.1.2 Borohydride Reduction Method-2 with Ethanol as Solvent

This method was modified from aqueous based method by changing the solvent with ethanol. In initial trials with higher amount of reducing agent in water, the product formed started to bubble out of the glassware and thus resulted in the loss of product. This was due to the hydrolysis of $NaBH_4$ in water resulting in the release of H_2[25]. Consequently, less amount of $NaBH_4$ remained for the reduction of the Cr and Pt precursors. To solve this problem, ethanol was used as solvent as the hydrolysis of $NaBH_4$ in ethanol is less vigorous as compared to that in water and thus more $NaBH_4$ will be available for reducing Cr and Pt precursors. As Nafion used in this study was a 10% solution in water and alcohol so it was assumed that the dissolution will not be affected when water is replaced by ethanol as a solvent. In this method, excess reducing agent ($NaBH_4$) was used with the aim to reduce more amount of Cr from $CrCl_3$ as it has been reported in literature that with the higher amount of reducing agent the reduction rate of Cr can be increased [26, 27]. This was attributed to a large difference in the driving force for the reduction process with respect to the Pt and Cr precursors. Moreover, the current reduction process only uses low temperature conditions and relatively weak reducing agents. Consequently, Pt which has a higher redox potential is preferentially reduced first, whereas the Cr precursor still struggles to fully attain the metallic state [27].

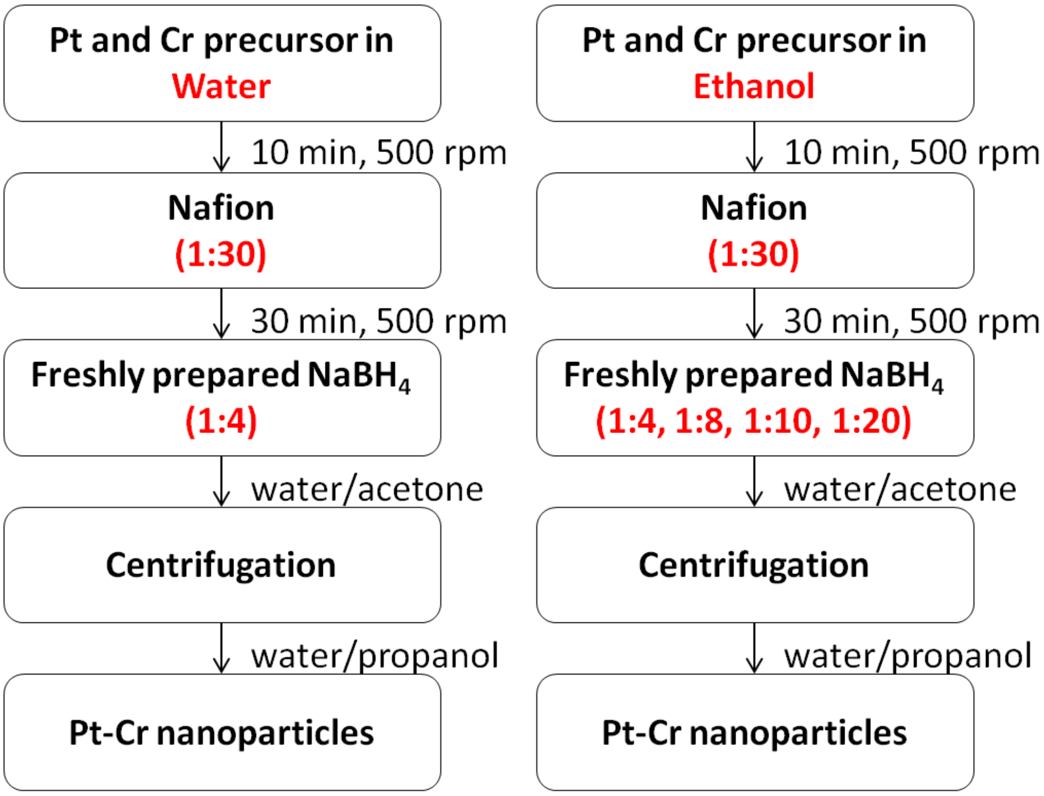

(a) (b)

Figure 3.1: Flow chart showing the synthesis of Nafion® stabilised Pt-Cr nanoparticles using borohydride method

Figure 3.1 (b) shows the flowchart with different steps involved in the synthesis. Pt precursor ($PtCl_6^{2-}$) and Cr precursor ($CrCl_3$) were dissolved in ethanol in the molar ratio of 1:1 and mixed in a flask with continuous stirring at 500 rpm for 10 min using magnetic stirrer. Nafion® (10%) was added in the mixture to attain a ratio of 1:30 of metal: Nafion®. The mixture was stirred for 30 mins at 500 rpm for the Nafion® to be completely dispersed with the both precursors. A freshly prepared solution of $NaBH_4$ was added in the mixture in different stoichiometry to obtain different alloy compositions. The ratios used were 1:4, 1:8, 1:10 and 1:20. An instant change of colour from green to black confirmed the reduction of the precursors. Thus, the product was fully available for further purification and different characterisation. The product was centrifuged for 1 hr by adding more acetone to remove the excess Nafion®. The product was further redispersed using ultrasonication in the mixture of 1:4 v/v water/acetone and centrifuged thrice.

3.2. Synthesis and Purification of Pt-Cr Core-Shell Nanoparticles

A new mechanism for the formation of Pt/Cr shell/core structure has been proposed in this section. This method involves formation of a stable core of Cr before the attachment of a monolayer of Pt shell on top of it. This method was divided into 3 sections:

1) Synthesis of [2,2’-bipyridine]-5 amine (NH_2-BiPy)
2) Formation of [2, 2’-bipyridine]-5-diazonium (D-BiPy)
3) Synthesis of Pt/Cr shell/core nanoparticles

This synthesis was done at room temperature without the use of any protective environment as Cr nanoparticles formed during this synthesis are expected to be stable with the attachment to the diazonium compound.

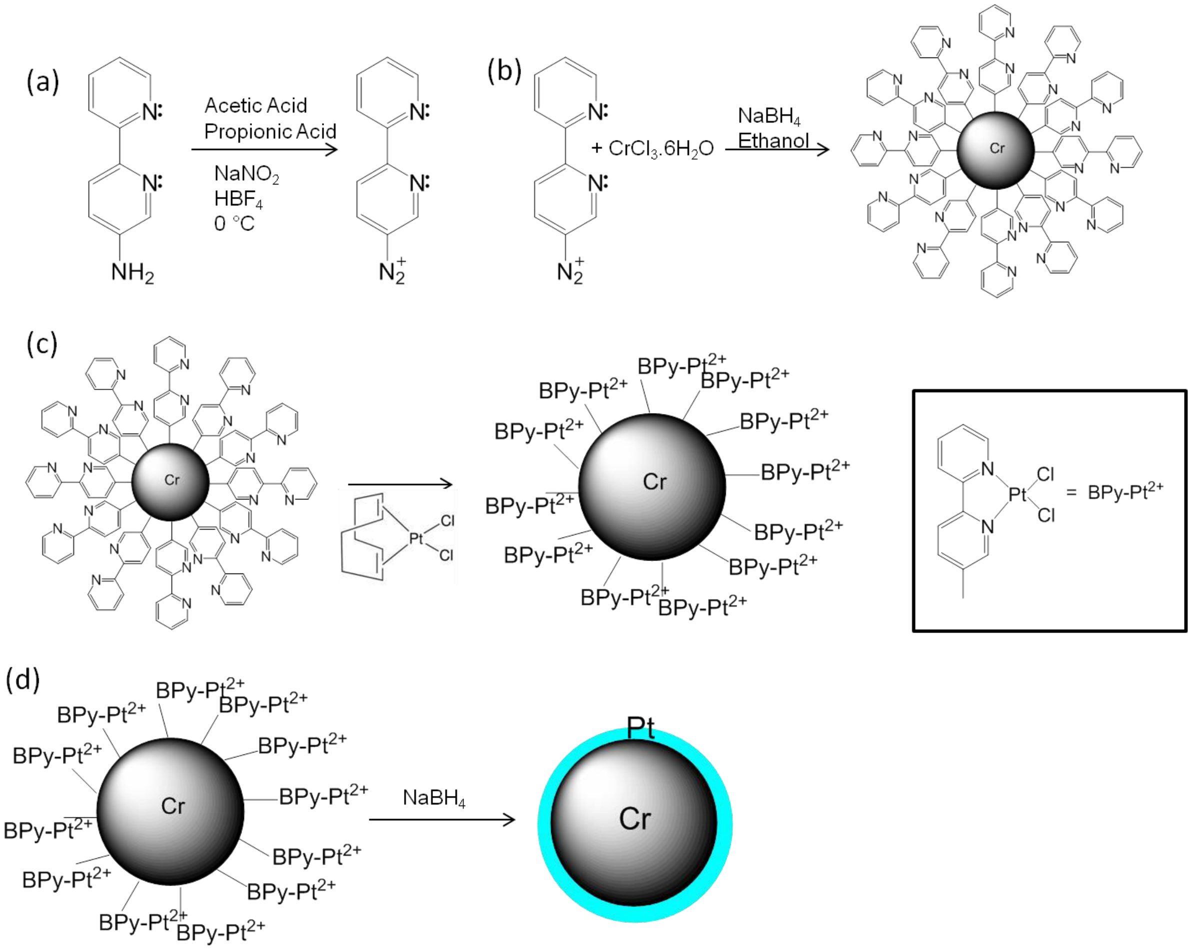

Figure 3.2: Schematic for the synthesis of Pt/Cr shell/core

1) Synthesis of NH_2-BiPy

NH_2-BiPy was supplied by Dr. Parvez Iqbal from School of Chemistry, University of Birmingham. NH_2-BiPy was synthesised via a multiple step synthetic route (figure 3.3), initiated with the protection of commercially available 4-bromo, aminopyridine to form the pyrrole derivative **1** in the presence of 2, 5-hexanedione. Tributylstannylpyridine (**2**) was obtained through reaction of commercially available 2-bromopyridine with n-BuLi and tributyltin chloride. The Stille reaction was undertaken to couple pyrrole derivative **1** and stannylpyridine (**2**) in the presence of catalytic amount of tetrakis(triphenylphosphine)-palladium(0) to yield the pyrrole bypyridine derivative (**3**). The desired NH_2-BiPy was synthesised by reacting pyrrole bypridine derivative **3** with hydroxylamine hydrochloride in the presence of base, triethylamine.

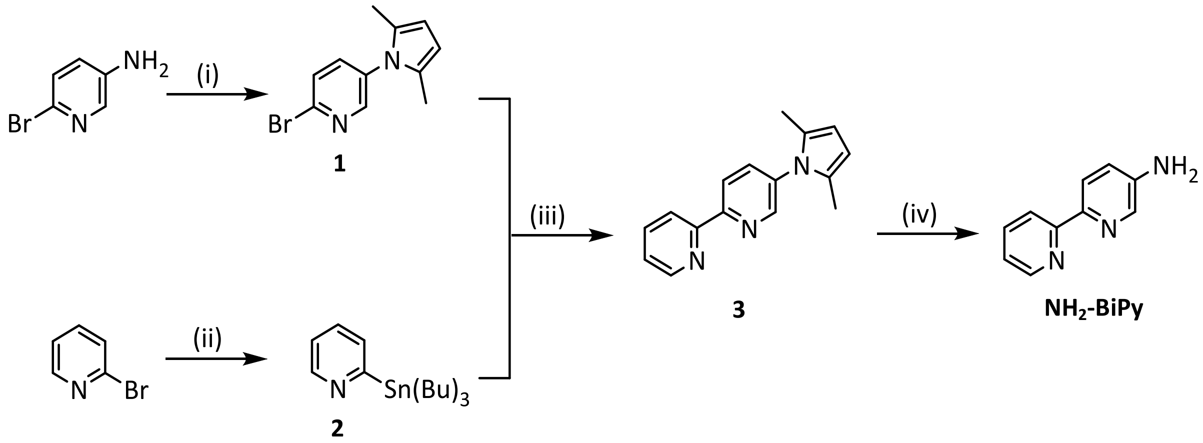

Figure 3.3: Synthesis of **NH_2-BiPy**; (i) *p*-TsOH, hexanedione, PhMe, reflux, N_2(g) atm, 4 h; (ii, a) n-BuLi, Et_2O, N_2(g) atm, -78 °C, 1 h, (ii, b) $(Bu)_3SnCl$, THF, N_2(g) atm, -78 °C, 1 h; (iii) $[Pd(PPh_3)_4]$, PhMe, N_2(g) atm, 130 °C, 24 h; (iv) $NH_2OH.HCl$, Et_3N, EtOH, H_2O, reflux, 24 h.

Experimental

Materials. Commercially available chemicals were purchased from Sigma Aldrich and solvents from Fisher Scientific or VWR and used as received. Thin-layer chromatography (TLC) was carried out on aluminium plates coated with silica gel 60 F254 (Merck 5554). For the aryl-based compounds the TLC plates were air-dried and analysed under a short wave UV lamp (254 nm), whereas for the aliphatic compounds the TLC plates were air dried and developed in a $KMnO_4$ dip. Column chromatographic separations were either performed on silica gel 120 (I24C8 Chrom 32– 63, 60 A°) or alumina (activated basic, Brockmann I, standard grade, ~150 mesh, 58 Å)

1-1-(2-Bromopyridine-5-yl)-2, 5-dimethyl-1*H*-pyrrole (1)

p-TsOH (15 mg, 0.08 mmol) was added to a solution of 2-bromo-5-aminopyridine (1.00 g, 5.78 mmol) and 2,5-hexanedione (0.65 g, 6.40 mmol) in dry PhMe (20 ml) and the resultant solution was heated at refluxed for 4 h under a N_2 atmosphere. After the reaction mixture cooled to room temperature, the mixture was quenched with saturated aqueous solution of $NaHCO_3$ and the aqueous layer was extracted with DCM (2 x 20 ml). The organic layer was washed with H_2O (20 ml), dried ($MgSO_4$), filtered and solvent removed *in vacuo*. The resultant product was purified by flash silica gel column chromatography (elute: hexane/EtOAc, 9:1) and the solvent was removed *in vacuo* to yield pyrrole pyridine derivative **1** as a pale yellow solid (1.28 g, 88 %).

^{1}H NMR (300 MHz, $CDCl_3$, Me_4Si, 25 ^{o}C) δ_H 8.58 (d, *J* = 2.9 Hz, 1H), 7.60 (d, *J* = 8.3 Hz, 2H), 7.40 (dd, *J* = 8.3, 2.9, 1 H), 5.92 (s, 2H), 2.02 (s, 6H); ^{13}C NMR (75 MHz, $CDCl_3$, Me_4Si, 25 ^{o}C) δ_C ppm 149.4, 140.7, 138.0, 135.1, 128.8, 128.4, 107.1, 13.0; m/z (ESMS): 251 ($[M + H]^+$, 100 %); m/z (HRMS): found 251.0171. Calc. Mass for $C_{11}H_{11}BrN$: 251.0178.

2-Tributylstannylpyridine (2)

A solution of 2.5 M BuLi (0.40 g, 0.58 ml, 6.29 ml) was added dropwise to a solution of 2-bromopyridine (1.00g, 6.29 mmol) in dry THF (12 ml) under a N_2 atmosphere at -78 ^{o}C. The reaction mixture was further stirred for 1 h under a N_2 atmosphere at -78 ^{o}C followed by dropwise addition of tributyltin chloride (2.05 g, 6.29 mmol) under a N_2 atmosphere at -78 ^{o}C. After the addition, the reaction mixture was further stirred for 10 min at -78 ^{o}C and then allowed to warm to room temperature. The reaction was quenched with saturated NH_4Cl solution (10 ml) and the aqueous layer was extracted with Et_2O (3 x 20 ml). The combined organic layers were washed with H_2O (10 ml) and brine (20 ml). The organic layer was dried

($MgSO_4$), filtered and solvent removed *in vacuo*. The crude product was purified by flash alumina column chromatography (elute: hexane/EtOAc, 19:1) and the solvent was removed *in vacuo* to yield a pale yellow oil (2.27 g, 98 %).

^{1}H NMR (300 MHz, $CDCl_3$, Me_4Si, 25 °C) δ_H 8.76 (dd, *J* = 4.9, 1.3 Hz, 1H), 7.52 (td, *J* = 7.4, 1.3 Hz, 1H), 7.43 (dd, *J* = 7.4, 1.2 Hz, 1H), 7.14 (ddd, *J* = 7.4, 4.9, 1.2 Hz, 1H), 1.67-1.03 (m, 18H), 0.83 (t, , *J* = 7.3 Hz, 9H): ^{13}C NMR (75 MHz, $CDCl_3$, Me_4Si, 25 °C) δ_C ppm 174.0, 150.5, 133.3, 132.4, 122.0, 29.127.2 14.1; m/z (ESMS): 370 ([M + H]$^+$, 100 %); m/z (HRMS): found 370.1562. Calc. Mass for $C_{17}H_{32}N_2Sn$: 370.1557.

1-(2, 2'-Bipyridine -5-yl))-2, 5-dimethyl-1*H*-pyrrole (3)

A solution of 2-(tributyltin) pyridine **2** (0.54 g, 1.46 mmol) in PhMe (2 ml) was added to a solution of **1** (0.24 g, 0. 96 mmol) in PhMe (5 ml) followed by addition of catalytical amount of [$Pd(PPh_3)_4$] (12 mg , 7.00 µmol) under a N_2 atmosphere. The reaction mixture was heated at 130 °C for 16 h and then allowed to cool to room temperature. The reaction was quenched with 1 M NaOH and the aqueous layer was extracted with EtOAc (2 x 20 ml). The combined organic layers were washed with brine, dried ($MgSO_4$), filtered and the solvent removed *in vacuo*. The crude product was purified by flash silica gel column chromatography (gradient elution; 0 to 20 % EtOAc in hexane, increase in increments of 5 % after 100 ml of eluent) and solvent removed *in vacuo* to yield white solid (0.19 g, 80 %).

^{1}H NMR (300 MHz, $CDCl_3$, Me_4Si, 25 °C) δ_H 8.72 (dd, *J* = 4.4, 1.0 Hz, 1H), 8.58 (d, *J* = 2.4 Hz, 1H), 8.54 (dd, *J* = 7.9, 0.9 Hz, 1H), 8.44 (d, *J* = 8.0 Hz, 1H), 7.86 (td, *J* = 7.9, 1.0 Hz, 1H), 7.69 (dd, *J* = 8.0, 2.4 Hz 1 H), 7.35 (ddd, *J* = 7.9, 4.4, 0.9 Hz, 1 H), 5.97 (s, 2H), 2.09 (s, 6H); ^{13}C NMR (75 MHz, $CDCl_3$, Me_4Si, 25 °C) δ_C ppm 155.3, 155.2, 149.1, 148.4, 137.1, 136.3, 135.6, 129.0, 124.0, 121.1, 106.8, 13.1; m/z (ESMS): 272 ([M + Na]$^+$, 100 %); m/z (HRMS): found 272.1157. Calc. Mass for $C_{16}H_{15}N_3Na$: 272.1164.

5-Amino-2, 2'-bipyridine hydrochloride (NH_2-BiPy)

A solution of **3** (0.25 g, 1.00 mmol), hydroxylamine hydrochloride (0.70 g, 10.00 mmol) and Et_3N (0.22 g, 2.18 mmol) in a mixture of EtOH (1.8 ml) and water (0.78 ml) was heated at reflux for 16 h. The reaction mixture was allowed to cool to room temperature, followed by quenching with 1 M HCl (10 ml). The solution pH was adjusted to 9-10 with addition of 1 M $NaOH_{(aq)}$ and the aqueous layer was extracted with DCM (3 x 10 ml). The combined organic layers were dried ($MgSO_4$), filtered and solvent removed *in vacuo*. The crude brown solid was dissolved in MeOH and a few drops of concentrated HCl were added which led to precipitation. The white precipitate was collected through suction filtration (133 mg, 80 %).

^{1}H NMR (300 MHz, $CDCl_3$, Me_4Si, 25 °C) δ_H; ^{1}H NMR (300 MHz, $CDCl_3$) δ 8.61 (d, *J* = 4.8, 1.8, 0.9 Hz, 1H), 8.24 (dt, *J* = 7.4, 2.1, 1.0 Hz, 1H), 8.19 (d, *J* = 8.6 Hz, 1H), 8.15 (d, *J* = 2.8 Hz, 1H), 7.75 (td, *J* = 8.0, 7.5, 1.8 Hz, 1H), 7.21 (ddd, *J* = 7.5, 4.8, 1.2 Hz, 1H), 7.09 (dd, *J* = 8.5, 2.8 Hz, 1H), 3.86 (br, *J* = 6.3 Hz, 1H); ^{13}C NMR (75 MHz, $CDCl_3$, Me_4Si, 25 °C) δ_C ppm 156.4, 148.9, 146.9, 142.9, 136.8, 136.5, 122.5, 122.1, 121.7, 199.9; m/z (ESMS): 172 ([M + H]$^+$, 100 %); m/z (HRMS): found 172.0868, Calc. Mass for $C_{10}H_{10}N_3$: 172.0875.

Compound characterisation

NMR. ^{1}H Nuclear magnetic resonance (NMR) spectra were recorded on a Bruker AVIII300 (300.13 MHz) spectrometer. ^{13}C NMR spectra were recorded on a Bruker AVIII 400 (75.5 MHz) using Pendent pulse sequences. All chemical shifts are quoted in ppm to higher frequency from Me_4Si using either deuterated chloroform ($CDCl_3$) as the lock and the residual solvent as the internal standard. The coupling constants are expressed in hertz (Hz) with multiplicities abbreviated as follows: s = singlet, d = doublet, dd = double doublet, t = triplet, q = quartet and m = multiplet.

Mass spectrometry (MS). Electron impact mass spectroscopy (EIMS) was performed on a VG Prospec. Low and high resolution electrospray mass spectrometry was performed on a Micromass time of flight (TOF) instrument using methanol as the mobile phase.

2) Formation of diazonium compound

NH_2-BiPy was supplied by Dr. Parvez Iqbal and used as received. In a typical preparation, 10 mg of the NH_2-BiPy was dissolved in 100 µl of a 50/50 v/v mixture of acetic and propionic acid to which 70 µl of 50 wt. % aqueous solution of tetrafluoroboric acid (HBF_4, Sigma) was added before cooling to 0ºC in an ice bath. 25 mg of $NaNO_2$ was added in small proportions under stirring (figure 3.2 (a)). The mixture was stirred for 1 hr and allowed to warm gently to ~10ºC. The product was dried under low pressure vacuum line overnight to remove all the solvents and a yellow crystalline solid was left. The presence of the diazonium moiety in the product was confirmed by FTIR and NMR spectroscopy. Samples for NMR were prepared by dissolving ~5 mg of the product in deuterated methanol (MeOD), and the crystalline solid was directly used as FTIR sample. ^{1}H NMR (300 MHz, MeOD) δ 9.83 (dd, J = 2.4, 0.5 Hz, 1H), 9.13 (dd, J = 9.0, 2.5 Hz, 1H), 8.99 (dd, J = 9.0, 0.6 Hz, 1H), 8.87 (ddd, J = 4.8, 0.8 Hz, 1H), 8.73 (dt, J = 7.0, 0.9 Hz, 1H), 8.19 (td, J = 7.8, 1.7 Hz, 1H), 7.73 (ddd, J = 7.7, 4.9, 1.1 Hz, 1H). IR (KBr) ν_{max} cm^{-1} 2290 ($N\equiv N^+$). m/z (ESMS): 187 ([M + H]$^+$, 100 %); m/z (HRMS): found 187.1, Calc. Mass for $C_{10}H_8N_4$: 187.1.

3) Synthesis of Pt/Cr shell/core

The D-BiPy used for the Pt/Cr shell/core synthesis was prepared and used straightaway as it is quite unstable. The D-BiPy was dissolved in ethanol and mixed with Cr precursor (in ethanol solvent) for 10 minutes and freshly prepared $NaBH_4$ solution was added slowly for the reduction of Cr precursor to form Cr nanoparticles surface functionalised with the bipyridine derivative (figure 3.2 (b)). A change of color from light green to dark green was observed during the synthesis that suggests the reduction of Cr precursor. Pt precursor was added slowly to the mixture for the Pt ions to adsorb on the surface of the core by forming a complex with the bypiridine moiety (figure 3.2(c)). Following complexation for 20-30 seconds, Pt reduction took place. The total time for reaction was 20-30 minutes to make sure all the reactants were reduced. The Pt precursor that reduces after complexation with the bipyridine molecule forms a shell on the Cr core already present in the mixture (figure 3.2(d)).

3.3 Characterisation

The nanoparticles synthesised using the above two methods were characterised using various techniques which are explained in this section.

3.3.1 Thermogravimetric Analysis (TGA)

It is a technique to measure the change in the physical and chemical properties of a material which are recorded as mass change as a function of time or temperature when the material is heated using a predefined temperature program. Mass change is recorded as a function of temperature in case of constant heating rate and as a function of time under isothermal conditions. This technique is used in the present study to determine the amount of Nafion® as well as the material content of the final product. It has been employed by various researchers in the field for determining the Vulcan and Pt content as they observe a decomposition peak of carbon around 150-300 °C which is catalysed by the Pt and the residual mass can give the Pt content at 800 °C. Baturina *et al.* [28] studied the thermal stability of different supported catalyst and reported that decomposition of Vulcan normally starts after 550 °C with gradual mass loss and a sudden drop above 625 °C. However, they observed that the decomposition temperature was reduced when Pt was supported on the carbon. Figure 3.4(a) shows the behaviour of the Pt/C with different loading in comparison with Vulcan XC-72 as observed during the thermogravimetric analysis in air. Platinum accelerates the rate of carbon decomposition and the onset temperature was reduced to 150-200 °C while the abrupt mass loss occurs at 400 °C. The residual mass left after the decomposition is the platinum content. Stevens *et al.* [29] also observed the similar behaviour for the platinum catalyst supported on carbon. Ammam *et al.* [30] reported the same behaviour for Pt-Cu alloy catalysts supported on carbon as shown in Figure 3.4(c). The TGA of the different alloy catalysts supported on carbon showed that the onset of the decomposition of carbon was similar for all the catalyst but the alloy catalyst PtCu/C had different profile in comparison with Pt/C and Cu/C. This behaviour suggests that the catalytic combustion effect has decreased for PtCu/C towards the combustion of carbon.

Baturina *et al.* [28] also demonstrated that TGA can be used to determine the Nafion® content in the catalyst layer and it can be seen from the figure 3.4(b). The figure shows the TGA curve in air for Nafion® membrane, Pt/C catalyst and catalyst layer. Degradation of Nafion® 112 occurs between 300-500 °C, however it has been observed by Samms *et al.* [31] that when the membrane is loaded with Pt, the decomposition temperature of Nafion® is reduced and occurs at much lower temperature. The same behaviour can be seen in the

Figure 3.4(b), the catalyst layer has 3 different decomposition regions. The mass loss below 300 °C is very low and can be attributed to the decomposition of the C-O of the Vulcan. The detailed study of the second and third region led to the conclusion that second region which is from 300-350 °C is due to the decomposition of Nafion® while above 350 °C is the decomposition of carbon. The Pt amount can be estimated as the residual mass above 400 °C. The same technique was employed in the present study to estimate the Nafion® content from decomposition and Pt from the residual mass at 800 °C and the instrument used is Netzsch TG.

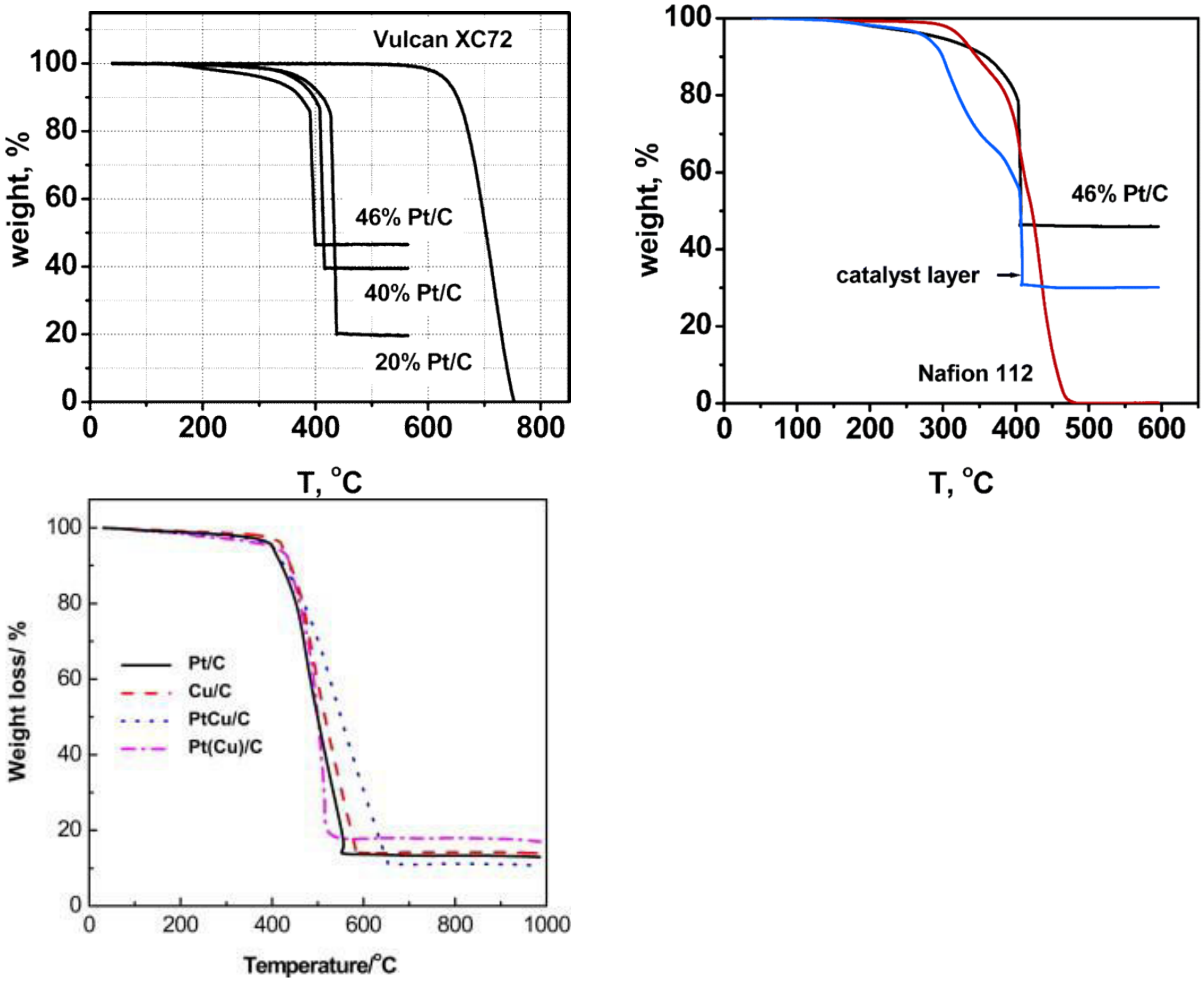

Figure 3.4: TGA graph in air for (a) Vulcan XC-72 and supported catalysts with 20, 40 and 46 % Pt on C, (b) Nafion® 112 membrane, 46% Pt/C catalyst and a catalyst layer containing both Pt/C and Nafion® (Reproduced with permission from[28]) (c) Pt/C, Cu/C, PtCu/C, and Pt(Cu)/C (Reproduced with permission from [30]).

3.3.2 Transmission Electron Microscopy (TEM)

Transmission electron microscopy (TEM) is a characterisation technique in which an accelerated electron beam at high operating voltages is allowed to transmit through a sample within ultra-high vacuum and a range of signals are generated. These signals (scattered electrons, X-rays) are utilised in various imaging and spectroscopic techniques to give a detailed analysis of the specimen under investigation. As it is a transmission technique, it is imperative that the specimen under investigation has a very fine thickness of less than 1000 Å. The main advantage of TEM over other microscopic techniques is firstly the high resolution due to very low wavelength of the highly energetic electrons. Furthermore, the range of signals generated due to the electron-specimen interaction makes it a complete characterisation tool to investigate the morphology, crystal structure, defects, phases and composition by imaging, electron diffraction and mapping[32].

Sample preparation: The colloidal solution of Pt-Cr or Pt-Cr/C was dispersed in water/ethanol and sonicated for 10-15 min. A drop of the solution was pipetted and dropped on a standard copper grid with carbon film (Agar-Scientific) and left to dry on its own in vacuum and placed in TEM holder for analysis. The samples were freshly prepared before TEM in order to avoid any contamination or degradation of the sample on exposure to the atmosphere.

Low magnification or initial TEM analysis was done on a JEOL 1200ex LAB6 TEM operated at an accelerating voltage of 80 kV. This technique was useful to give an idea about the distribution of nanoparticles as well as the size of the particles. However this instrument did not have the possibility to carry out compositional analysis of the nanoparticles using energy dispersive spectroscopy of X-rays (EDS).

High Resolution imaging was done in a FEI Tecnai F20 field-emission TEM operated at 200 kV (University of Leeds, UK) equipped with an Oxford Instruments detector for EDS analysis. The compositional analysis was carried out using the INCA software from Oxford Instruments. Electron diffraction patterns were obtained to confirm the crystallinity of the particles. The particle size analysis was done using the graphical analysis software ImageJ.

3.3.3 X-Ray Diffraction (XRD)

X-Ray diffraction is a non-destructive technique used to study the atomic or molecular structure of a crystal. As crystalline materials have a regular periodic arrangement of atoms, it is possible to deduce the crystal structure by illuminating the sample with a monochromatic source of X-rays. When the incident X-rays interfere constructively with the periodic arrangement of the atomic planes, a unique diffraction pattern is generated for each crystal structure [33, 34]. This behaviour has been described by Bragg's Law:

$$2d\sin\theta = n\lambda$$

where d is the spacing between the planes, n is an integer which gives the order of diffraction, λ is the wavelength and θ is the angle between incident ray and scattering planes. When Bragg´s Law is satisfied at specific angles of detection, a peak is observed in the diffraction pattern. Analysis of these diffraction patterns allows the identification of different phases present within a given sample. With that achieved, it may be possible to quantify each phase present, the crystallinity of a sample, the crystal structures and their lattice parameters, crystallite size and strain.

The crystallite size can be calculated using the Scherer equation which gives a relationship between the sizes to the amount of broadening of a peak in the diffraction pattern[33, 34]. The equation is:

$$\mathrm{B} = \frac{\mathrm{K}\lambda}{\beta \mathrm{Cos}\,\theta}$$

where B is the mean crystallite size, K is the dimensionless shape factor constant which is usually taken as unity, λ is the wavelength of the X-rays used, β is the line broadening at half the maximum intensity (FWHM) and θ is the Bragg's angle.

XRD can be used to calculate the lattice parameters of the samples tested which can confirm the element present. For the calculation of lattice parameters, the d-spacing was calculated for the different peak positions using the Bragg's law as reported above.

After the calculation of d-spacing, the following equation for the calculation of lattice parameter for cubic system is used

$$d = \frac{a}{\sqrt{h^2 + k^2 + l^2}}$$

where d is the d-spacing for a given plane, a is the lattice parameter, (h,k,l) are the reciprocal indices of the planes.

The instrument used for recording the X-ray diffraction pattern for all the nanoparticles synthesised in the present study was INEL XRD Equinox 3000 that uses a Cu Kα target.

3.3.4 X-ray Photoelectron Spectroscopy (XPS)

XPS is a surface sensitive chemical analysis technique useful for measuring the elemental composition and chemical or electronic state of surface elements, with a sensitivity of parts per thousand. Dry samples supported on electrically conductive surface have to be used for this technique due to ultra high vacuum involved during the observation to prevent charging of the samples. A monochromatic source of X-ray is used which results in the excitation and ejection of core-level electrons. An electrostatic analyser is used for the analysis of energy of the photoelectrons and the photoelectrons are detected by an electron multiplier tube or a multichannel detector such as a microchannel plate. The energies of ejected photoelectrons are related to their initial binding energies within their atomic orbitals. The energy of these photoelectrons are less than 1500 eV and thus they interact strongly with material, and so can only escape from the top few atomic layers (6-10 nm)[35-37]. The oxidation states of the elements can be analysed from the shifts in the binding energy as the binding energy of an electron is related to the oxidation state and local chemical environment of the atom. The higher the oxidation state of the atom (i.e. the more electron-deficient), the higher the binding energy associated with its remaining electrons due to increased Coulombic interaction with the atomic nucleus. Thus, this technique is useful for the analysis of the oxidation states and composition of the elements present in the material. The analysis of the XPS spectrum is done using a software such as CasaXPS [36].

This technique was used to analyse the elemental composition and oxidation states of these elements, confirming the presence of Nafion® in the samples for all the nanoparticles synthesised using the two methods explained above. The XPS analysis was performed at NEXUS, EPSRC National XPS Facility, University of Newcastle and the machine used is AXIS Nova (Kratos Analytical).

3.4 Electrochemical Characterisation

The as prepared catalysts were electrochemically characterised to study the electrochemical surface area, oxygen reduction reaction, durability/degradation, power density and impedance. This characterisation was done using two methods: 1) Ex-situ 2) In-situ.

3.4.1. Ex-Situ Electrochemical Characterisation

Ex-situ testing can provide valuable information regarding the intrinsic properties of a catalyst under controlled, reproducible conditions. All the electrochemical testing procedures were done at 25°C in a 3 electrode cell, using an Autolab PGSTAT302N potentiostat (Metrohm) and a Pine rotating disc electrode (RDE) setup. Glassy carbon electrode was used as working electrode, platinum mesh as counter electrode and reversible hydrogen electrode (RHE) as the reference electrode. The electrolyte in all cases was 0.1 M $HClO_4$ solution prepared from 70% perchloric acid (Sigma-Aldrich). All the potentials were reported with reversible hydrogen electrode (RHE). Metal loadings of 20 $\mu g/cm^2$ were used for all the cyclic voltammetry (CV) and oxygen reduction reaction (ORR) experiments. The ink was prepared by supporting Pt-Cr nanoparticles on the Vulcan support in the ratio 1:1 to make the composition of the catalyst to be 50 wt% Pt-Cr/C in all cases. The ink was sonicated for 30 min to allow the mixing and homogenisation of the catalyst with support. The working electrodes were prepared using a glassy carbon electrode (GCE) that was polished using alumina slurry of 1, 0.3 and 0.05 microns. 10 µl of the catalyst ink was then drop cast on the polished surface and completely dried in a vacuum oven at 40 °C for 12 hours.

3.4.1.1 Cyclic Voltammetry (CV)

CV is a useful electrochemical technique to study the redox reaction and thus advantageous in the present case to determine the electrochemical surface area (ECSA) of the catalyst. As-prepared electrodes were mounted on the Pine rotors and inserted in 0.1 M $HClO_4$ solution. The solution was purged with N_2 gas for 20 min before performing any measurements to saturate the solution with an inert gas. A CV scan for commercial Pt catalyst is shown in figure 3.5. CV scans were performed at 250 mV/s from 0.05 V to 1.1 V to remove the contaminants present on the surface of the catalyst. Cyclic voltammograms were then recorded at a scan rate of 25 mV/s in the same potential range. Electrochemical surface area (ECSA) (m^2/g_{Pt}) was then measured by integrating the hydrogen underpotential desorption (H_{upd}) region (0.05-0.4 V) in the slow scan rate CVs using equation

$$\mathrm{ECSA} = \frac{Q_H}{210\ L_{Pt} A}$$

where Q_H (μC) is the charge measured upon desorption of H_2 in the underpotentially-deposited (UPD) hydrogen region (grey region in figure 3.5), L_{Pt} is the Pt loading (μg/cm^2), A is the geometric area of the GCE (cm^2) and the value of 210 μC/cm^2 corresponds to the charge required to adsorb/desorb a monolayer of H_2 on bulk polycrystalline Pt surface.

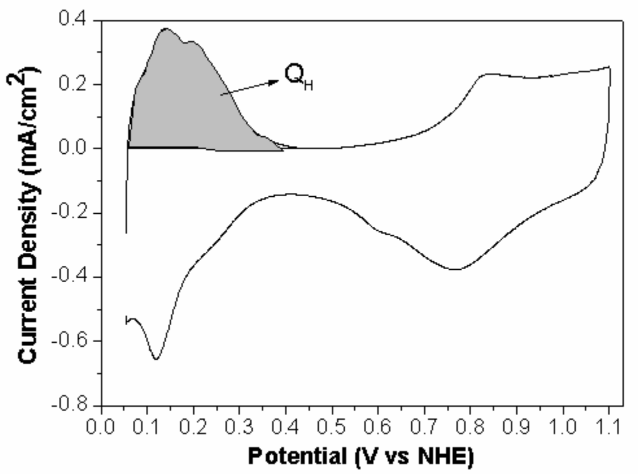

Figure 3.5: Linear CV graph showing the Hupd region (Q_H) which is taken for calculation of electrochemical surface area (ECSA).

3.4.1.2. Linear Sweep Voltammetry (LSV)

After the CV scans, the polarisation curves were recorded between 0.05 to 1.2 V vs RHE at a scan rate of 25 mV/s at room temperature. The sweeps were recorded at rotating speeds of 400, 800, 1200, 1600 and 2000 rpm. The solution was then purged with pure oxygen (O_2) for at 30 mins and the same sweeps were recorded in O_2. It was assumed that the solution was saturated with O_2 based on the trials done for O_2 purging at different purging times ranging from 10-40 mins. It was observed that when the solution was purged for 10, 15 or 20 mins the limiting current for the LSV obtained at different rotation rates tend to overlap and the limiting current value also increased with increase in purge time. However, when the solution was purged for 30 mins or longer, limiting current reached highest value. No overlapping was observed for the LSV curves after that time and no further increase in current with extra purging time. Thus purging time of 30 mins was chosen to get saturated O_2 in the solution for all the experiments. All the sweeps showed a well defined limiting current region below 0.6 V and a diffusion-kinetic region from 0.7- 1.0 V. IR drop was compensated for solution resistance to the LSV data. A representative graph of LSV showing the various steps discussed above is presented in figure 3.6.

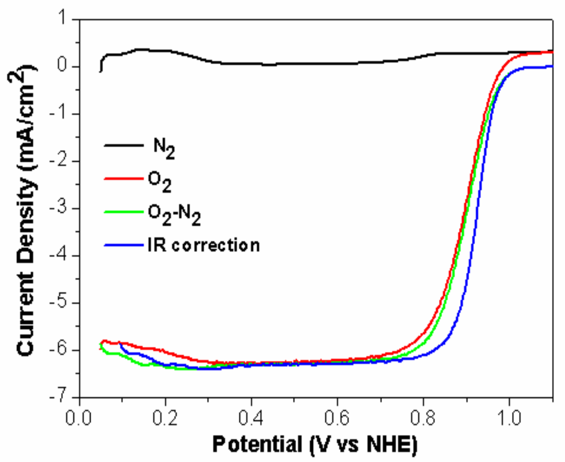

Figure 3.6: Linear sweep voltammograms showing the process followed for analysis of the oxygen reduction reaction (ORR).

3.4.1.3. Accelerated Stress Testing (AST)

Accelerated stress testing (AST) was used to study the degradation behaviour of the standard catalyst as well as the PtCr/C catalyst. The procedure was to measure the ECSA by cyclic voltammetry at 25 mV/s using the H_{upd} method before and after the cycling [13]. Cycling consisted of square wave potential cycle from +0.6 V to 1.0 V holding for 1s at each potential [38]. These potential were chosen in order to reproduce the open circuit and peak power output condition in the PEMFCs. The square wave potential step was chosen over linear potential sweep as this produced highest degradation loss due to Pt dissolution which shortens the test duration[39]. This is also the most widely used test for the degradation study. The ECSA was measured after every 1,200 cycles up to 4,800 cycles. Figure 3.7 shows the representative graph for one cycle of the AST testing.

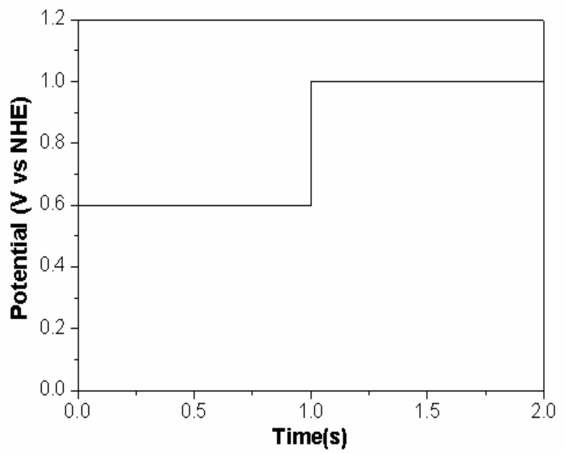

Figure 3.7: Accelerated stress testing used for degradation

3.4.2 In-Situ Electrochemical Characterisation

It involves the testing of the catalyst under simulated PEMFC operating conditions by the fabrication of MEAs and thus the practical utility of the catalyst can be estimated. The testing was done for the catalyst synthesised by the method-2 only due to the formation of alloys in that case whereas the catalyst from method-1 showed only traces of Cr and thus not tested. All the in-situ testing was done using single cell in a Paxitech FC-50 fuel cell test stand.

Ink Preparation:

Different batch of catalysts were synthesised in order to prepare one MEA per batch and thus also check the reproducibility of the synthesis as well as the MEAs. They were synthesised and purified using the method as described in section 3.1.2. After the purification of the catalyst using centrifugation, catalysts were dispersed in water/isopropanol as it gave good results in the RDE experiments and literature has also shown the same for MEAs[38]. Vulcan carbon was added to the catalyst solution to attain a catalyst to carbon ratio of 1:1 so that the catalyst has a loading of 50 wt% in all the cases (i.e. 50% Pt-Cr/C). Nafion® dispersion was added to the Pt/C ink to achieve the optimum Nafion® concentration of 33% Nafion fractional percentage (NFP) whereas no Nafion was added to Pt-Cr/C catalyst inks. Inks were ultrasonicated in an ice-cold water bath for 45 minutes to avoid any changes in the nanoparticles structure which may occur due to heating of the bath.

MEA Fabrication:

MEA consists of a cathode gas diffusion layer, cathode catalyst, membrane, anode catalyst and anode gas diffusion layer. MEAs of the size 4 x 4 cm were used for all the materials with a Nafion® membrane of 5 x 5 cm. The materials used for the present study are discussed as below:

For the preparation of anodes, Nafion dispersion diluted to 1 wt.% with iso-propyl alcohol (IPA) was painted on the catalysed side of commercial gas diffusion electrodes (Johnson Matthey, 0.4 $mg_{Pt}cm^{-2}$ on SGL 34BC) to achieve a Nafion® loading of 33 % NFP, followed by drying in a vacuum oven. The Nafion® loading was calculated by weighing the electrodes before and after painting.

Cathodes were prepared by hand painting catalysts (Pt-Cr/C, Pt/C) on the gas diffusion material (Freudenberg C2) which was dried under a UV lamp. The electrodes were left for drying in vacuum oven overnight and the catalyst loading was determined by weighting electrodes before and after painting.

Nafion® 212 membranes were used as-received without further treatment. Membrane Electrode Assemblies (MEAs) were prepared by hot-pressing anode and cathode GDEs either side of a Nafion® 212 membrane (120ºC, 180 kPa, 120 s).

3.4.2.1 Single Cell Fuel Cell Testing

The single cell fuel cell testing was done using Paxitech FCT-50S PEMFC test stand (Bilogic). The MEA was placed between two gaskets on either side and compressed between the graphite flow field plates with single cell serpentine channels geometry. Gold plated plates were used as current collectors and aluminum end plates were used to control the heating of anode and cathode. A schematic of a PEMFCs single cell is shown in figure 3.8.

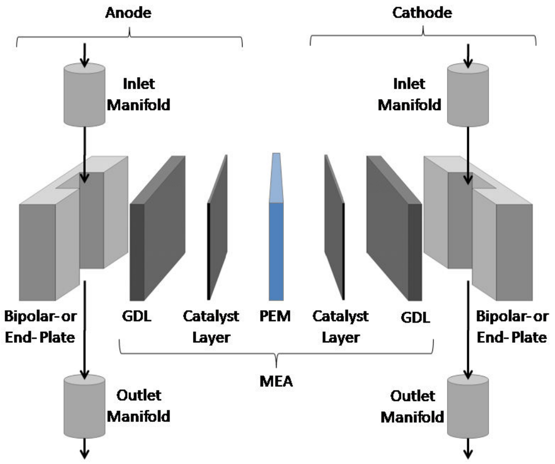

Figure 3.8: Schematic showing different components which form a single cell to be tested in single cell fuel cell.

Activation

For the activation of the MEAs, the cell temperature was brought to 70 ºC and the flow rate of H_2 (120 cm^3/min) and air (300 cm^3/min) at 2 bar backpressure flowing on the anode and cathode, respectively. The cell voltage was maintained at 0.6 V for conditioning until the current is stabilised or at least 12 hours. This is done to completely hydrate the Nafion membrane which results in the maximum performance by reducing ohmic resistance and increasing triple phase boundary [40].

Polarization Curves

After the MEAs were fully activated, the cell was subjected to 50 rapid potential sweep cycles between open circuit potential and 0.25 V. Then a slow potential sweep was performed in the same potential range with 0.01 V increments, 3s per point. All the measurements were taken by maintaining the reactant stoichiometries on the anode and cathode at 1.3 (H_2) and 2.4 (air) respectively, with minimum reactant gas flow rates of 120 cm^3/min (H_2) and 300 $cm^{3/}$min (air).

When electric current is drawn from a fuel cell, the open circuit voltage drop and this is called polarisation. These drops are due to the overpotential which arises because of current and mass transport losses. The total overpotentials, η, can be calculated by the equation between the real voltage E and the theoretical one (E_t)

$$\eta = E - E_t$$

A typical fuel cell polarisation curve, voltage as a function of current density and power density, is shown in Figure 3.9.

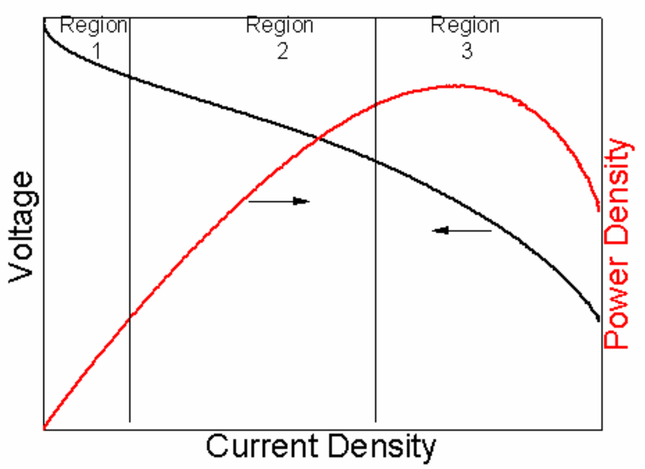

Figure 3.9: Characteristic polarisation and power density curve of a fuel cell.

The polarisation curve shown in figure 3.9 can be divided into 3 regions due to the different overpotential which control the behavior of the curve namely activation, ohmic resistance and mass transport overpotential. Region 1 in Figure 3.9 is activation overpotential controlled and it represents the magnitude of activation energies when the charge transfer reactions propagate. The factors affecting the activation range from the catalyst and electrolyte material, temperature, current density, type of reactions. Anode activation overpotential is neglected during calculations as the hydrogen oxidation overpotential is negligible when compared to the oxygen reduction reaction overpotential [41, 42].

A pseudo-linear behavior can be seen in the region 2 in figure 3.9 with the increase in current density and this is due to the ohmic overpotential which is related to the resistance of fuel cell components. The resistances which contribute towards ohmic overpotentials are the intrinsic resistance to electron due to the interfaces between different components and ionic resistance by electrolyte material[41, 42].

Region 3 is controlled by the mass transfer overpotential. At higher current density, supply of reactants become sluggish due to higher demand of reactants and causes the drop in the cell voltage due to increase current demand.

Electrochemical Impedance Spectroscopy

Electrochemical Impedance Spectroscopy (EIS) is a powerful tool for a) the determination of electrochemical reaction mechanisms and b) measure of kinetic and transport parameters. It is used for the analysis of complicated processes involving surface and solution reactions like electrode and electrolyte in the case of PEMFC. EIS uses a range of low magnitude polarizing alternating current voltages that cycle from peak anodic to cathodic magnitudes and vice versa. Importantly, it allows decoupling of the various losses (Ohmic, activation and mass-transport related) contributing to the overall losses in cell or stack performance.

Electrochemical Impedance Spectroscopy (EIS) was recorded at 2 current densities; low current density (close to OCV) and high current density. Impedance was measured by applying a small AC electrical current or voltage (5% of the DC current or voltage) and measuring the output voltage or current respectively. Measurements are performed at a number of different frequencies usually between 10 kHz and 0.1 Hz. The collected data can be represented as a Nyquist plot which plots imaginary impedance versus real impedance [43-47].

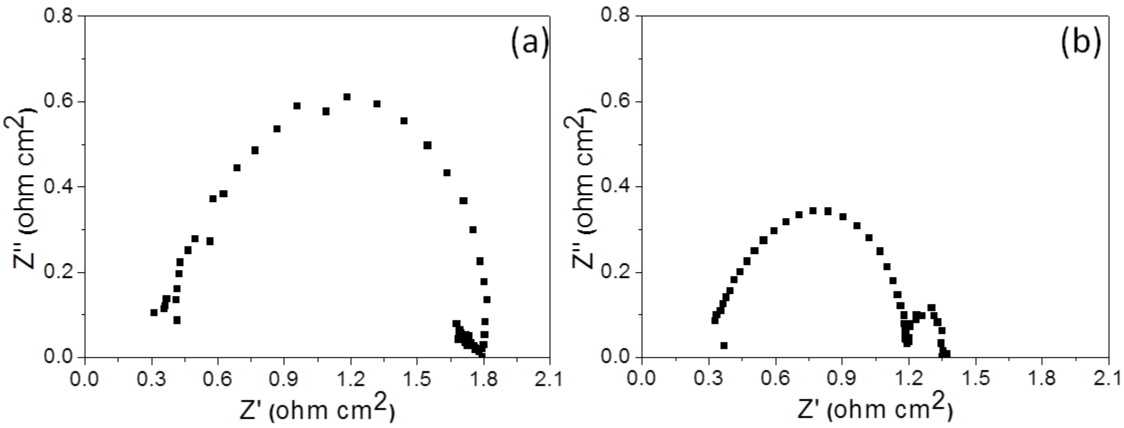

Figure 3.10: Characteristic Nyquist plot for a catalyst at low (a) and high (a) current density

Figure 3.10 shows the characteristic Nyquist plots for a catalyst at low (a) and higher (b) current density. At lower current density, the EIS shows only a single arc whereas at higher current density a second arc is also seen. The height and width of the first arc reduces at higher current density. The changes in behaviour can be better understood with the help of the mechanisms taking place at both current densities outlines in figure 3.11.

Figure 3.11 represent the contribution of the three polarisation processes in the MEA to the impedance values at different current densities. ORR kinetics influences the impedance at the lower potential and results in the formation of a single semicircular arc. The charge transfer resistance which is a measure of the electrode kinetics is represented by the diameter of the semicircle. Ohmic resistance is calculated from the high-frequency impedance value of the curve. A small arc appears at the low frequency region with the increase in the current density. This arc represents the mass transport resistance in the cell (Figure 3.10). The charge transfer resistance decreases with the increase in current density and results in the lowering of diameter of first arc. The size of the mass transport arc increases as a result of increase in mass transport polarisation at higher current density.

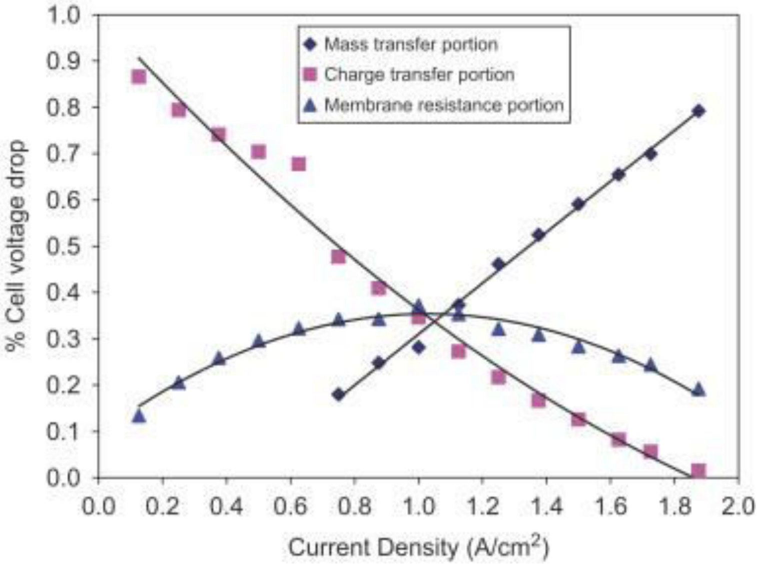

Figure 3.11: Potential loss contribution of the different polarisations with the change in current density. Reproduced with permission from [44]

In this study, only a qualitative comparison has been performed for different catalysts by comparing the ohmic resistance of the cell, the size of the charge transfer arc and mass transport arc.

References

1. Antolini, E., et al., *Carbon supported Pt–Cr alloys as oxygen-reduction catalysts for direct methanol fuel cells.* Journal of Applied Electrochemistry, 2006. **36**(3): p. 355-362.
2. Li, W., et al., *Nano-stuctured Pt–Fe/C as cathode catalyst in direct methanol fuel cell.* Electrochimica Acta, 2004. **49**(7): p. 1045-1055.
3. Antolini, E., et al., *Preparation of carbon supported binary Pt–M alloy catalysts (M=first row transition metals) by low/medium temperature methods.* Materials Chemistry and Physics, 2007. **101**(2-3): p. 395-403.
4. Ghosh, T., et al., *Pt Alloy and Intermetallic Phases with V, Cr, Mn, Ni, and Cu: Synthesis As Nanomaterials and Possible Applications As Fuel Cell Catalysts.* Chemistry of Materials, 2010. **22**(7): p. 2190-2202.
5. Jayasayee, K., et al., *Oxygen reduction reaction (ORR) activity and durability of carbon supported PtM (Co, Ni, Cu) alloys: Influence of particle size and non-noble metals.* Applied Catalysis B: Environmental, 2012. **111-112**: p. 515-526.
6. Liu, Z.L., et al., *Carbon-supported Pt and PtRu nanoparticles as catalysts for a direct methanol fuel cell.* Journal of Physical Chemistry B, 2004. **108**(24): p. 8234-8240.
7. Markovic, N.M., et al., *Oxygen Reduction Reaction on Pt and Pt Bimetallic Surfaces: A Selective Review.* Fuel Cells, 2001. **1**(2): p. 105-116.
8. Min, M.K., et al., *Particle size and alloying effects of Pt-based alloy catalysts for fuel cell applications.* Electrochimica Acta, 2000. **45**(25-26): p. 4211-4217.
9. Oezaslan, M., F.d.r. Hasché, and P. Strasser, *Oxygen Electroreduction on PtCo3, PtCo and Pt3Co Alloy Nanoparticles for Alkaline and Acidic PEM Fuel Cells.* Journal of The Electrochemical Society, 2012. **159**(4): p. B394.
10. Hasché, F.d.r., M. Oezaslan, and P. Strasser, *Activity, Structure and Degradation of Dealloyed PtNi3 Nanoparticle Electrocatalyst for the Oxygen Reduction Reaction in PEMFC.* Journal of The Electrochemical Society, 2012. **159**(1): p. B25.
11. Lázaro, M.J., et al., *Influence of the synthesis method on the properties of Pt catalysts supported on carbon nanocoils for ethanol oxidation.* Journal of Power Sources, 2011. **196**(9): p. 4236-4241.
12. Zignani, S.C., E. Antolini, and E.R. Gonzalez, *Stability of Pt–Ni/C (1:1) and Pt/C electrocatalysts as cathode materials for polymer electrolyte fuel cells: Effect of ageing tests.* Journal of Power Sources, 2009. **191**(2): p. 344-350.
13. Curnick, O.J., P.M. Mendes, and B.G. Pollet, *Enhanced durability of a Pt/C electrocatalyst derived from Nafion-stabilised colloidal platinum nanoparticles.* Electrochemistry Communications, 2010. **12**(8): p. 1017-1020.
14. Celorrio, V., et al., *Electrochemical performance of Pd and Au–Pd core–shell nanoparticles on surface tailored carbon black as catalyst support.* International Journal of Hydrogen Energy, 2012. **37**(8): p. 7152-7160.
15. Adams, B.D., C.K. Ostrom, and A. Chen, *Highly Active PdPt Catalysts for the Electrochemical Reduction of H2O2.* Journal of The Electrochemical Society, 2011. **158**(4): p. B434.
16. Prabhuram, J., et al., *A simple method for the synthesis of PtRu nanoparticles on the multi-walled carbon nanotube for the anode of a DMFC.* Electrochimica Acta, 2007. **52**(7): p. 2649-2656.
17. Lima, F.H.B., et al., *Electrocatalytic Properties of PtCo⁄C and PtNi⁄C alloys for the Oxygen Reduction Reaction in Alkaline Solution.* Journal of The Electrochemical Society, 2007. **154**(4): p. A369.
18. Vinayan, B.P., et al., *Catalytic activity of platinum–cobalt alloy nanoparticles decorated functionalized multiwalled carbon nanotubes for oxygen reduction reaction in PEMFC.* International Journal of Hydrogen Energy, 2012. **37**(1): p. 412-421.

19. Salgado, J.R.C., E. Antolini, and E.R. Gonzalez, *Structure and Activity of Carbon-Supported Pt−Co Electrocatalysts for Oxygen Reduction.* The Journal of Physical Chemistry B, 2004. **108**(46): p. 17767-17774.
20. Salgado, J.R.C., E. Antolini, and E.R. Gonzalez, *Preparation of Pt-Co/C electrocatalysts by reduction with borohydride in acid and alkaline media: the effect on the performance of the catalyst.* Journal of Power Sources, 2004. **138**(1-2): p. 56-60.
21. Salgado, J.R.C., E. Antolini, and E.R. Gonzalez, *Pt-Co/C Electrocatalysts for Oxygen Reduction in H[sub 2]/O[sub 2] PEMFCs Synthesized by Borohydride Method.* Journal of The Electrochemical Society, 2004. **151**(12): p. A2143.
22. Ramossanchez, G., H. Yeemadeira, and O. Solorzaferia, *PdNi electrocatalyst for oxygen reduction in acid media.* International Journal of Hydrogen Energy, 2008. **33**(13): p. 3596-3600.
23. http://www.charleston.k12.il.us/chs/Teachers/KeatingT/Keating's%20Classes_files/Reduction%20Potentials.pdf.
24. Curnick, O., *Ionomer-Stabilised Pt and Pt-Ti Bimetallic Electrocatalysts for the Proton Exchange Membrane Fuel Cell*, in *School of Chemical Engineering*2012, University of Birmingham: Birmingham.
25. Glavee, G.N., et al., *Borohydride Reduction of Nickel and Copper Ions in Aqueous and Nonaqueous Media. Controllable Chemistry Leading to Nanoscale Metal and Metal Boride Particles.* Langmuir, 1994. **10**(12): p. 4726-4730.
26. Jeon, M.K., Y. Zhang, and P.J. McGinn, *Effect of reduction conditions on electrocatalytic activity of a ternary PtNiCr/C catalyst for methanol electro-oxidation.* Electrochimica Acta, 2009. **54**(10): p. 2837-2842.
27. Yang, H., et al., *Tailoring, Structure, and Activity of Carbon-Supported Nanosized Pt−Cr Alloy Electrocatalysts for Oxygen Reduction in Pure and Methanol-Containing Electrolytes.* The Journal of Physical Chemistry B, 2004. **108**(6): p. 1938-1947.
28. Baturina, O.A., S.R. Aubuchon, and K.J. Wynne, *Thermal Stability in Air of Pt/C Catalysts and PEM Fuel Cell Catalyst Layers.* Chemistry of Materials, 2006. **18**(6): p. 1498-1504.
29. Stevens, D.A. and J.R. Dahn, *Thermal degradation of the support in carbon-supported platinum electrocatalysts for PEM fuel cells.* Carbon, 2005. **43**(1): p. 179-188.
30. Ammam, M. and E.B. Easton, *PtCu/C and Pt(Cu)/C catalysts: Synthesis, characterization and catalytic activity towards ethanol electrooxidation.* Journal of Power Sources, 2013. **222**(0): p. 79-87.
31. Samms, S.R., *Thermal Stability of Nafion® in Simulated Fuel Cell Environments.* Journal of The Electrochemical Society, 1996. **143**(5): p. 1498.
32. Williams, D. and C.B. Carter, *The Transmission Electron Microscope*, in *Transmission Electron Microscopy*. 2009, Springer US. p. 3-22.
33. Cullity, B.D. and S.R. Stock, *Elements of X-Ray Diffraction*. Third ed. 1956: Addison-Wesley. 531.
34. Suryanarayana, C. and M.G. Norton, *X-Ray Diffraction: A Practical Approach*. 1998, New York: Plenum Press.
35. Watts, J.F., *An introduction to surface analysis by XPS and AES*. 2003, Chichester: J. Wiley.
36. Fairley, N., *CasaXPS Manual*. 2009.
37. Heide, P.v.d., *X-ray Photoelectron Spectroscopy: An introduction to Principles and Practices*. 2011, Hoboken, NJ, USA: John Wiley & Sons.
38. Takahashi, I. and S.S. Kocha, *Examination of the activity and durability of PEMFC catalysts in liquid electrolytes.* Journal of Power Sources, 2010. **195**(19): p. 6312-6322.
39. Uchimura, M. and S.S. Kocha, *The Impact of Cycle Profile on PEMFC Durability.* 2007. **11**: p. 1215-1226.

40. Silva, V.B. and A. Rouboa, *Hydrogen-fed PEMFC: Overvoltage analysis during an activation procedure.* Journal of Electroanalytical Chemistry, 2012. **671**: p. 58-66.
41. Gasteiger, H.A., et al., *Beginning of life MEA performance-efficiency loss contributions*, in *Handbook of Fuel Cells: Fundamentals, Technology and Applications*, W. Vielstich, A. Lamm, and H.A. Gasteiger, Editors. 2003, Wiley. p. 593.
42. Appleby, A.J. and F.R. Foulkes, *Fuel Cell Handbook*. 1989, New York, USA: van Nostrand Reinhold.
43. Brug, G.J., et al., *The analysis of electrode impedances complicated by the presence of a constant phase element.* Journal of Electroanalytical Chemistry and Interfacial Electrochemistry, 1984. **176**(1–2): p. 275-295.
44. Tang, Y., et al., *Temperature Dependent Performance and In Situ AC Impedance of High-Temperature PEM Fuel Cells Using the Nafion-112 Membrane.* Journal of The Electrochemical Society, 2006. **153**(11): p. A2036.
45. Bard, A.J. and L.R. Faulkner, *Electrochemical Methods: Fundamentals and Applications*. Second ed. 2001, New York: John Wiley & Sons, INC.
46. Ye, F., et al., *Synthesis and Catalytic Performance of PtRuMo Nanoparticles Supported on Graphene-Carbon Nanotubes Nanocomposites for Methanol Electro-Oxidation.* International Journal of Electrochemical Science, 2012. **7**(2): p. 1251-1265.
47. Yu, X. and S. Ye, *Recent advances in activity and durability enhancement of Pt/C catalytic cathode in PEMFC: Part II: Degradation mechanism and durability enhancement of carbon supported platinum catalyst.* Journal of Power Sources, 2007. **172**(1): p. 145-154.

Chapter 4
Nanoparticle Characterisation

The previous chapter explained the different methods used for the synthesis of Nafion-stabilised Pt-Cr nanoparticles and different characterisation techniques that can be used to understand the morphology, size and composition of the nanoparticles. The focus of this chapter is on characterising the synthesised nanoparticles using the techniques discussed in chapter-3. This chapter is important as it forms the link between the nanoparticles which have been synthesised using borohydride reduction method and the electrocatalytic properties they possess (discussed in chapter-5), which can only be understood by the analysis of morphology, composition and size of these particles.

This chapter is divided into two sections on the basis of two different synthesis methods used for Pt-Cr alloys which has been explained in section 3.1 (water and ethanol based).

1) ***Nafion-stabilised Pt-Cr nanoparticles (aqueous)***
2) ***Nafion-stabilised Pt-Cr nanoparticles (ethanol)***

The first characterisation technique that was used to estimate the amount of Nafion and metal present in the final product was thermogravimetric analysis (TGA). After that transmission electron microscopy (TEM) coupled with energy dispersive spectroscopy (EDS) analysis was done to understand the morphology, size, composition of the particles. X-ray diffraction (XRD) was done to study the size as well as the crystalline structure, phases present in the nanoparticles. X-ray photoelectron spectroscopy (XPS) was used to study the atomic composition and oxidation states of the elements present.

4.1. Nafion-stabilised Pt-Cr Nanoparticles (aqueous)

These nanoparticles were synthesised using borohydride reduction method in aqueous solvent. The synthesis method has been described in the previous chapter 3 under section 3.1. The nanoparticles were purified by centrifugation using acetone as the solvent to remove the excess amount of Nafion. The details of the parameters used for purification are reported in the section 3.1. The amount of Nafion showed no change after purification for 3rd and 4th cycle and thus 4 purification cycles were used for all the samples. The nanoparticles are characterised using different techniques to study the amount of Nafion along with particle morphology, size and composition of the Pt-Cr nanoparticles and reported below

4.1.1 Thermogravimetric Analysis (TGA)

The nanoparticles are synthesised with different initial concentrations of Nafion in order to optimise the Nafion content to obtain a good stabilisation, dispersion and less agglomeration of the nanoparticles. The amount of Nafion and Pt-Cr is very important in the preparation of catalyst inks to study the electrochemical behaviour and comparing them to the literature results of the commercial catalysts [1]. TGA is a very useful technique to calculate the change in mass with increasing temperature and can be done in different oxidising or reducing conditions. The conditions used for the present case was air to decompose the Nafion present in the sample. It is expected to give the final amount of Nafion which is attached to the nanoparticles after purification that removed the excess amount of Nafion.

Figure 4.1 shows the thermo gravimetric curve of pure Nafion and different Nafion-stabilised Pt-Cr nanoparticles with varying initial Nafion amount after purification. As can be seen in figure 4.1, the decomposition of pure Nafion occurs between 75-550 °C, in agreement with reports from the literature [2-6]. There is a small loss in the temperature range of 75- 300 °C which corresponds to the loss of residual water in the Nafion. A second more prominent mass loss curve is seen from 300 – 420 °C which corresponds to the loss of sulphur dioxide from the Nafion. The final curve from the temperature range of 420 – 550 °C shows a drastic change in the mass and corresponds to the complete decomposition of the Nafion. The other curves show different behaviour for the decomposition of Nafion and it has been reported in literature that the decomposition temperature of Nafion reduces when Pt is present [7]. Pt-Cr nanoparticles synthesised with 10 times Nafion in the starting step shows only 5 % change in the mass between 75-500 °C which can be related to the decomposition of Nafion. This shows that the binding of Nafion to the nanoparticles is very low.

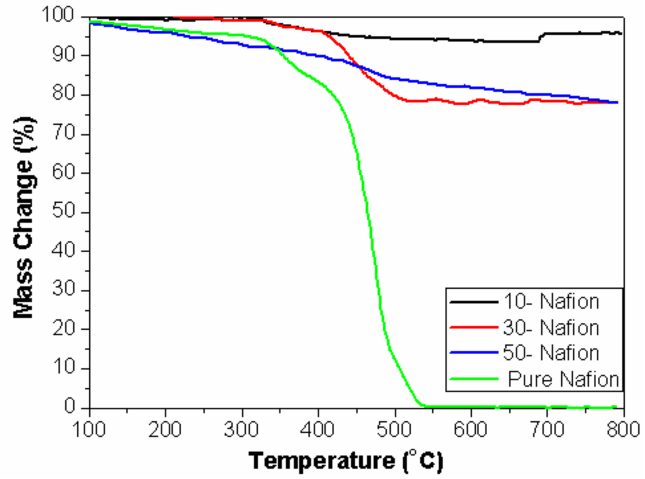

Figure 4.1 Thermogravimetric curve for pure Nafion and Nafion- stabilised Pt-Cr nanoparticles with varying initial Nafion concentration.

The samples with 50 times Nafion in the starting step showed the same behaviour as of the 10 times and drastic decomposition peak is observed between 300-500 °C but the change in mass is only 10 %. This change is very low considering the initial amount of Nafion. It can be said that due to the presence of excess amount of Nafion, the mixing of the Nafion with the nanoparticles was obstructed and thus only very less attachment of nanoparticles to the Nafion took place. Nafion content of 20 times was also tried (results not shown here) and it showed similar behaviour as sample with 10 times Nafion.

The samples with 30 times excess Nafion in the synthesis process showed a completely different behaviour compared to 10 and 50 times samples. It showed a clear decomposition curve for Nafion which started around 75 °C with a small change in mass which is related to the removal of attached water molecules till 300 °C. The second gradual peak which finished around 450 °C relates to the release of sulphur dioxide and then the final decomposition occurred with a drastic change in mass and finished around 550 °C. There is no other mass change observed in the process and thus the decomposition is solely for Nafion. The residual mass is 78 % which can be attributed to the amount of Pt-Cr and mass of Nafion present is 22 %. These results confirm that no impurities are present and it has been further confirmed by XPS and EDS analysis that will be discussed in section 4.1.2 and 4.1.4. Similar results have been reported by Curnick *et al.* [8] and thus the Nafion content of 30 times the amount of metal is selected for carrying out the synthesis. These samples were tested a minimum of three times to check the repeatability and it suggested that there was no proper trend and only the samples with Nafion content of 30 times showed a proper interaction with Pt-Cr.

4.1.2 Transmission Electron Microscopy (TEM)

TEM is a very useful technique to study the particle size, morphology, distribution of the nanoparticles and also the composition when it is coupled with EDS. In the present study, the nanoparticles were stabilised with Nafion and the amount of Nafion, Pt-Cr has been determined by TGA as discussed in the previous section 4.1.1. However, the binding of the

Nafion to the nanoparticles can only be studied by looking at the nanoparticles structure and the composition of Pt and Cr present by the EDS. A sample of Pt/C (TKK) is also studied in order to compare the structure of the commercial catalyst and also its behaviour in the later parts of this study.

Figure 4.2 (a) shows the TEM image of the commercial 46.5 wt. % Pt/C (TKK). The Pt nanoparticles are well dispersed on the carbon support with an average size of 5 ± 1 nm (inset). The particle size is measured by using ImageJ software over different regions of the sample and averaging over 150 particles. The diffraction pattern in figure 4.2 (b) that has been taken over an area of the sample shows different planes (111, 200, 220, 311) which corresponds to the fcc structure of the crystalline Pt but the sharpness of the crystalline nature of Pt has been reduced due to the presence of 55 wt. % C which shows a central amorphous ring. The further confirmation of the crystalline nature of the Pt can be done by the calculation of the lattice parameters from the different planes. This can be done by calculation of the d-spacing for the different planes in the diffraction pattern and then using the following formula for cubic structures.

$$d = \frac{a}{\sqrt{h^2 + k^2 + l^2}}$$

where d is the d-spacing for a given plane, a is the lattice parameter, (h,k,l) are the reciprocal indices of the planes. The lattice parameter calculated for Pt/C is 3.91 Å which matches well with the lattice parameter of the pure crystalline Pt as reported in literature[9, 10].

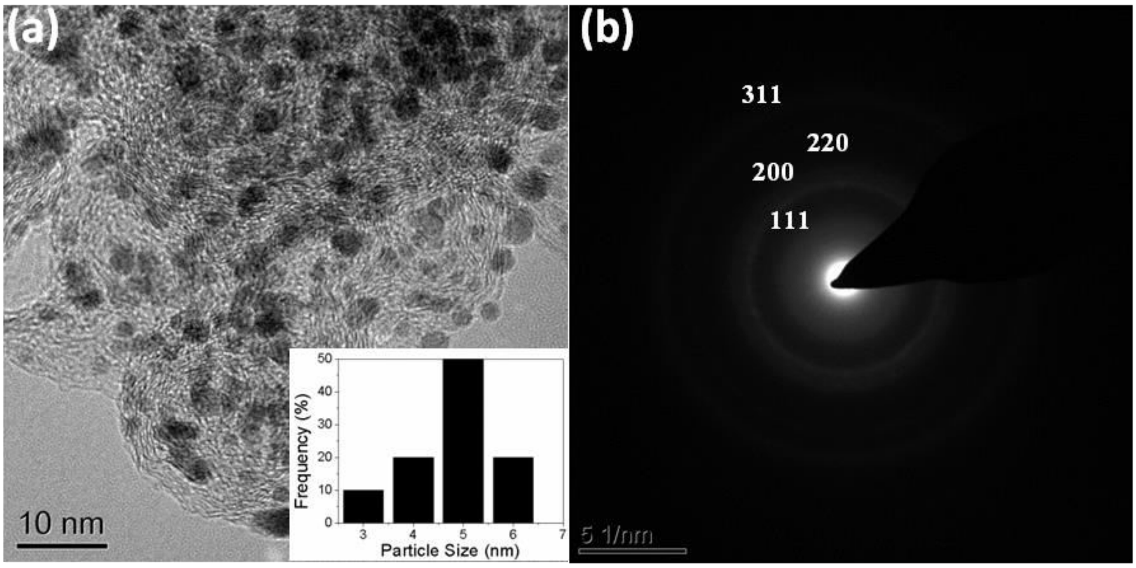

Figure 4.2: (a) TEM image (Inset: Particle size distribution), (b) Selected area diffraction pattern for Pt/C.

Figure 4.3 (a, b) shows the TEM image of Pt-Cr nanoparticles synthesised by the borohydride reduction method in aqueous solvent. The Pt-Cr nanoparticles form an agglomerated network with each other and also they are held together by Nafion which was used as a stabiliser in synthesis. The purpose of Nafion was to form an interconnected interface between the nanoparticles in order to avoid the dissolution of the particles during operation in fuel cells. During centrifugation, the synthesised product is rotated at very high speeds of 20000 rpm at a temperature of 4 °C, which removes the excess Nafion from the sample and the remaining Nafion in the sample is attached with the nanoparticles. Particle size distribution studies as shown in the inset of figure 4.3 (a) revealed a narrow distribution of the particles with an average particle size is 6 ± 2 nm with some agglomerated particles of 10 nm also. The particle size was calculated by averaging about 150 nanoparticles using high resolution images and the ImageJ software. Further analysis of particle size was done by X-ray diffraction which is discussed in section 4.1.3.

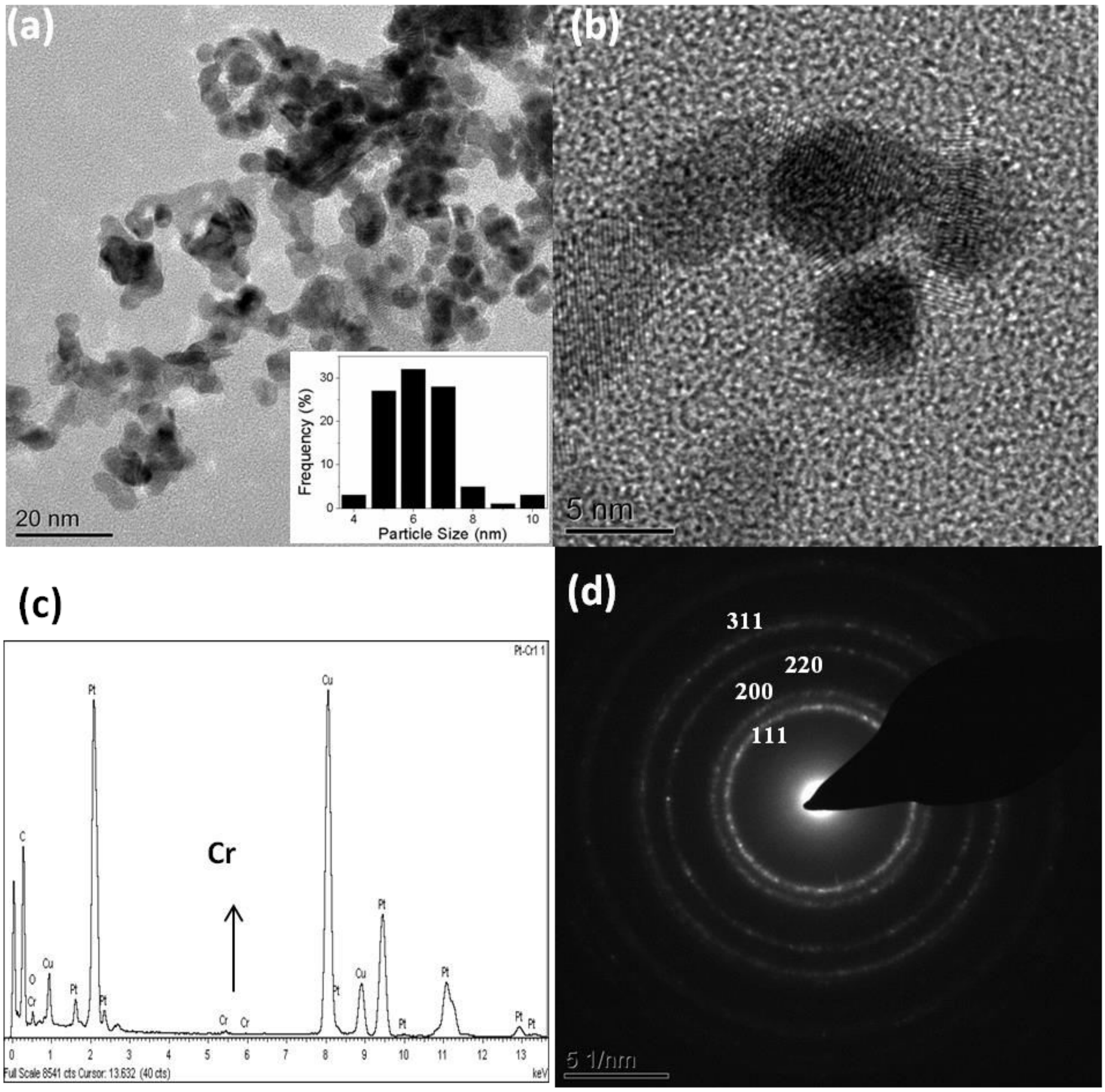

Figure 4.3: (a, b) TEM images, EDS (c) and diffraction pattern (d) for Nafion-stabilised Pt-Cr synthesised by the borohydride reduction method (Inset- particle size distribution).

Interestingly, energy dispersive spectroscopy (EDS) (Figure 4.3 (c)) during the TEM analysis suggested presence of only traces of Cr in the product and not an alloy. There are regions which showed no presence of Cr and thus can be said to contain pure Pt only. Similar observation is also made from XPS analysis which is discussed later (section 4.1.4). This could be due to the very less reduction of Cr during the synthesis. This behaviour can be attributed to a large difference in the driving force for the reduction process with respect to the Pt and Cr precursors. Pt which has a higher redox potential (1.33 V) is preferentially reduced first, whereas the Cr precursor still struggles to undergo reduction to give out Cr (-0.77 V) [11]. This has also been reported in literature and it was further observed by Jeon *et al.* [12] that a very high concentration of reducing agent is required for the reduction of Cr precursor. Moreover, the current reduction process only uses low temperature conditions and relatively weak reducing agents.

Figure 4.3 (d) shows the diffraction pattern obtained over an area of the nanoparticles shown in figure 4.3 (a). The lattice parameters calculated for the ring pattern (~3.91 Å) matches well with the lattice parameter of Pt (3.92 Å) [9, 10] and thus, it can be said that the diffraction pattern is for a face centred cubic structure of polycrystalline Pt with the following planes 111, 200, 220, 311 as we go away from the central ring. This in turn confirms that Pt is present in this case and no Cr.

From the TEM analysis, it can be said that the Nafion stabilised Pt-Cr nanoparticles form an agglomerated network with particle size in the range of 5-8 nm with some particles around 10 nm also. No alloy formation was observed and Cr was present only in trace amounts.

4.1.3 X-ray Diffraction (XRD)

The TEM analysis discussed above in the section 4.1.2 showed agglomerated nanoparticles in the range of 5-8 nm and the presence of traces of Cr and no formation of an alloy of Pt-Cr. XRD is a technique which is useful in studying the crystalline structure of the nanoparticles as well as can give the particle size. Thus it can be useful in validating and supporting the TEM results. The XRD samples are prepared by drying the sample on a silicon substrate and the details of the various parameters used are given in section 3.3.3. A sample of standard Pt/C (TKK) catalyst was also studied in order to compare the results with the catalysts synthesised in the present study.

Figure 4.4 shows the XRD graph for the commercial Pt/C (TKK catalyst) in comparison to the Nafion-stabilised Pt-Cr synthesised in the present case. All the peaks corresponding to various crystalline phases of Pt are present at the same position in both the cases and there is no shifting of the peak which should be seen in case of alloying and thus initial observation suggests that the Pt-Cr in present case is Pt with maybe traces of Cr as suggested by the TEM analysis. However, the peaks are sharp in case of Pt-Cr as compared to standard TKK which suggests the particle size for Pt/C is smaller as compared to Pt-Cr nanoparticles. The crystallite size is calculated using the Scherer equation as described in the chapter 3, section 3.3.3 which is as under:

$$B = \frac{K\lambda}{\beta \mathrm{Cos}\,\theta}$$

where B is the mean crystallite size, K is the dimensionless shape factor constant which is usually taken as unity, λ is the wavelength of the X-rays used (1.5405 Å), β is the line broadening at half the maximum intensity (FWHM) and θ is the Bragg's angle.

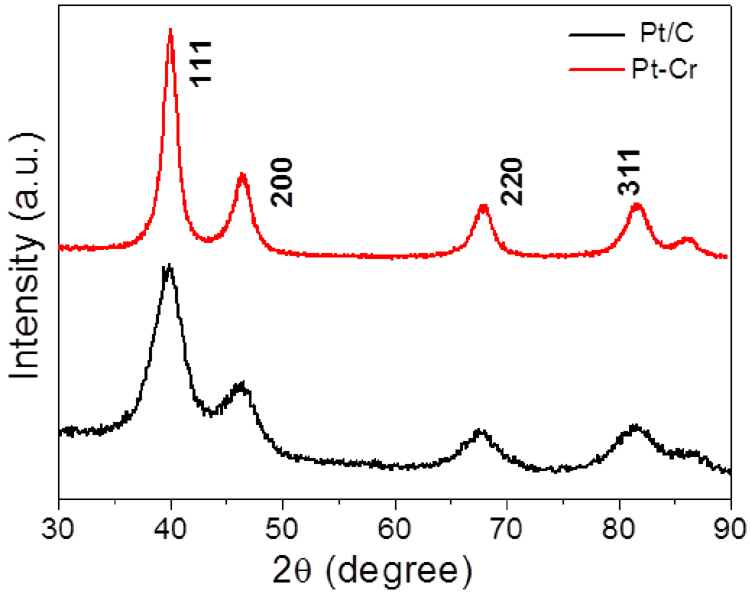

Figure 4.4: XRD graph of Pt/C and Pt-Cr.

The crystallite size is calculated using the 220 peak for Pt as the error in calculation becomes lower as we move towards the higher θ values [9, 10]. The crystallite size for the Pt/C is calculated to be 6 nm which is in line with the particle size calculated from TEM (5 ± 1 nm). However, the crystallite size for the Pt-Cr is 7 nm which is similar to the size calculated from TEM as 6 ± 2 nm with some agglomerates of 10 nm. So, it can be said that the particles are present over a range of 4-10 nm.

For the calculation of lattice parameters, the d-spacing was calculated for the different peak positions using the Bragg's law.

$$n\lambda = 2d\,Sin\theta$$

where n is an integer, λ is the wavelength of the X-ray used (1.5405 Å), d is the d-spacing between the planes, θ is the Bragg's angle of reflection.

After the calculation of d-spacing, the following equation for the calculation of lattice parameter for cubic system is used

$$d = \frac{a}{\sqrt{h^2 + k^2 + l^2}}$$

where d is the d-spacing for a given plane, a is the lattice parameter, (h,k,l) are the reciprocal indices of the planes.

The lattice parameters for both the samples (3.92 Å and 3.90 Å for Pt/C and Pt-Cr, respectively) are also calculated and they match well with the lattice parameters obtained from the TEM analysis discussed in section 4.1.2.

4.1.4 X-ray Photoelectron Spectroscopy (XPS)

TEM and XRD are useful techniques for the study of the particle size, morphology, distribution and composition of the nanoparticles. However, the oxidation states of the elements present is very important to study the amount of metal present in the native state, which will in turn contribute to the electrochemical behaviour of the catalyst. XPS is a surface sensitive technique which can be used to detect the presence of even trace amount of impurities present in the sample along with the oxidation states of the various elements. This technique is used in the present study to find the amount of impurities, verify the presence of Nafion (F, C, and O) and Pt and the oxidation states of Pt. XPS analysis of pure Nafion was done to form a baseline and observe the change in structure of Nafion after the synthesis of nanoparticles. A basic structure of Nafion is given in figure 4.5.

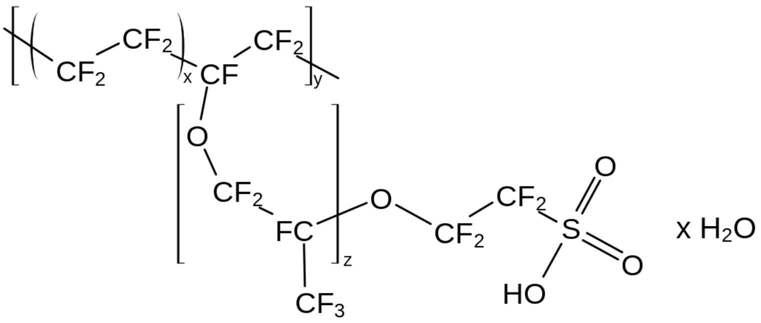

Figure 4.5: Structure of Nafion

Figure 4.6 shows the survey spectrum and high resolution spectra for C, O and F for the Nafion. As per the survey spectra (figure 4.6(a)), no impurities were present and elemental distribution of the different elements present is calculated and reported in table 4.1.

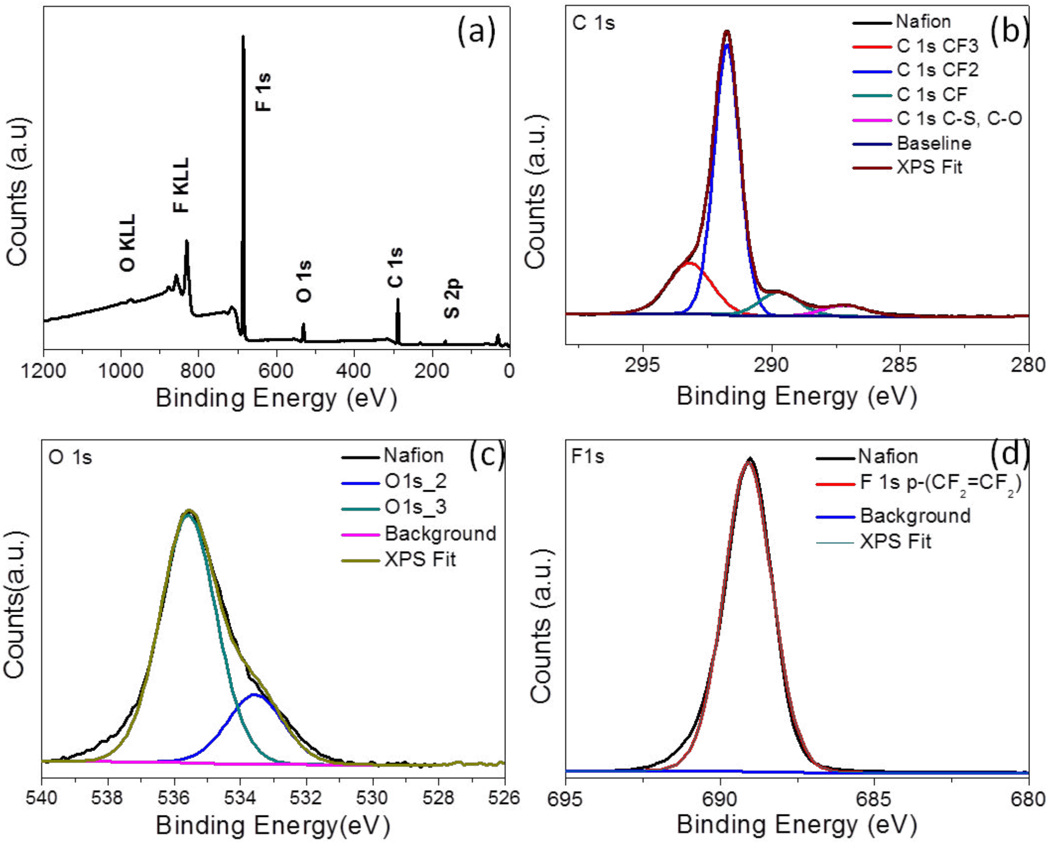

Figure 4.6: XPS spectrum of Nafion (a) survey spectrum (b, c, d) Peak fitting for C 1s, O 1s and F 1s, respectively.

Table 4.1: Atomic distribution of Nafion obtained from survey spectrum in figure 4.6 (a)

Element	C (at. %)	O (at. %)	F (at. %)	S (at. %)
Atomic percent	33.8	6.5	58.2	1.5

The elemental composition of the elements matches well with the theoretical value as per the structure of the Nafion and with the values reported in literature[13]. The high resolution spectrum for the C 1s (figure 4.6 (b)) is deconvoluted to fit the different components present in the structure of the Nafion molecule. The spectrum was normalised by using the peak position of CF_2 at 292 eV. The different components present in the structure are CF_3 (293.4 eV), CF (289.9 eV) and the peak at (287.4 eV) could be attributed to C-S and C-O as further deconvolution is not possible because the bond energies are too close. All the components present matched well with the literature values [13-15]. The O 1s spectrum (figure 4.6(c)) showed the presence of oxygen in the form of two components i.e. sulfonates group (O 1s_2- 533.5 eV) and ether group (O 1s_3- 535.5 eV) which are the different oxygen groups present as per the Nafion structure. The F 1s spectrum (figure 4.6 (d)) showed the presence of one component at 689.1 eV which is p-(CF_2=CF_2) which forms the basic building block for the Nafion structure.

Figure 4.7 shows the survey spectrum and high resolution spectra of F, C, Pt and O for Pt-Cr nanoparticles on Nafion. From the figure 4.7(a), it can be clearly seen that there are no impurities present in the sample and it contains only Pt, Nafion (C, F, O, S) and traces of Na which may be left over from the reducing agent, however the amount of Na is less than 2 at.%. Table-4.2 shows the atomic distribution of elements as calculated from the survey sprectrum. There were no peaks found for Cr which justifies the results obtained from TEM and XRD that there may be traces of Cr only in the catalyst. The F 1s was analysed using CASA XPS software and the results obtained are shown in figure 4.7 (b). It can be inferred from the fitting that only one component is present and the peak position is 689.1 eV. This binding energy corresponds to the p-(CF_2=CF_2) and thus it can be concluded that Nafion is present in the sample as it contains the same structure [16].

Table 4.2: Atomic distribution of Pt-Cr nanoparticles obtained from Figure 4.7 (a)

Element	C (at. %)	O (at. %)	F (at. %)	Pt (at. %)	Na (at. %)
Atomic percent	52.4	12.4	25.7	7.9	1.6

Figure 4.7 (c) shows the peak fitting for the C 1s after deconvolution and the different forms of C which is present can be read from the peak position by comparing it to the XPS handbook [16]. It shows the presence of C in the form of C-C (284.7 eV), C-O (286.2 eV), C-S (288.3 eV), CF (290.37 eV), CF_2 (291.9 eV) and CF_3 (293.6 eV). The structure of Nafion contains C-O, C-S, CF, CF_2 and CF_3 and thus gives further confirmation of the presence of Nafion attachment to the Pt. It is believed that the C-C (284.7 eV) is due to the breakage of the Nafion structure during the synthesis of the nanoparticles by formation of free radicals. It has been reported in the literature the side chains of the Nafion break during the decomposition of the Nafion which gives rise to the formation of C-C bonds and thus an increase in the concentration of C-C components with respect to the other components can be seen[6, 7, 14, 15, 17-21]. The decomposition also changes the concentration of C-O and C-S groups which are present in the side chains of the Nafion structure which can be confirmed from the O 1s spectrum as sulfonates and ether groups.

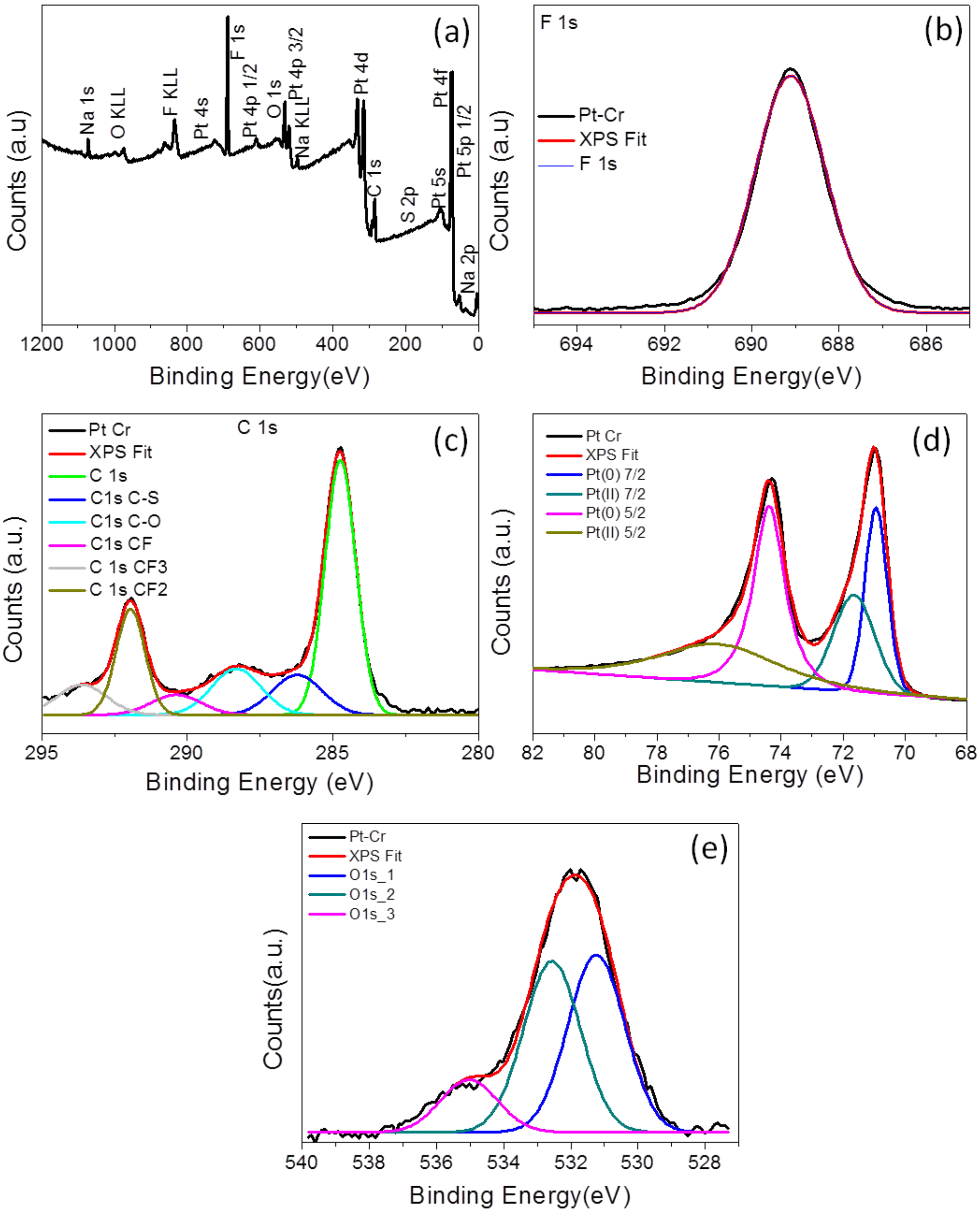

Figure 4.7: XPS spectrum of Pt-Cr nanoparticles (a) survey spectrum (b, c, d, e) Peak fitting for F 1s, C 1s, Pt 4f and O 1s, respectively.

The deconvolution of the high resolution Pt 4f spectrum shown in figure 4.7 (d) below suggests that the maximum amount of Pt is present in pure metallic form Pt^0 (71.1 and 74.4 eV) with some amount in the Pt^{2+} (71.7 and 76.1 eV) form and no Pt is there in the 4+ oxidation state. This confirms that the reduction of Pt precursor has occurred while the Cr precursor is not reduced as no Cr is found. The absence of Cr can be due to the large difference in the driving force for the reduction reaction of Pt and Cr. This has been explained in detail in the section 4.1.2, i.e. Pt has a higher redox potential and is preferentially reduced first, whereas the Cr precursor still struggles to be reduced and form Cr [11]. Figure 4.7 (e) shows the deconvoluted spectrum for the O 1s with different components of metal oxide (O 1s_1-531.2 eV), sulfonates (O 1s_2-532.6 eV) and ether groups (O 1s_3-535.1 eV). The metal oxide is due to the PtO which in turn confirms the presence of Pt in the Pt^{2+} oxidation state. It can be seen that the ratio of the sulfonates to the ether groups has decreased a lot as compared to the original ratio present in the Nafion structure. This is due to the breaking of the side chains of the Nafion structure giving rise to the decrease of the ether groups and also increases the sulfonates groups[15, 22, 23].

Thus, it can be said that there is no presence of any impurities and Cr in the nanoparticles. Pt is present mostly in the native state of Pt^0 with small amount in Pt^{2+} state. Presence of Nafion is also confirmed by the analysis of the peaks of C, F and O which forms the basic building blocks for the Nafion structure.

4.2. Nafion-stabilised Pt-Cr Nanoparticles (ethanol)

The nanoparticles obtained from the aqueous method did not show the presence of Cr and no alloy formation and thus the method was modified in order to obtain alloys of Pt-Cr. The nanoparticles were synthesised using borohydride reduction with ethanol as the solvent and this method has been described in detail in the previous chapter 3 under section 3.1.2. Ethanol was used as solvent in order to obtain better dispersion of the nanoparticles. The purification method for the nanoparticles wass the same as the one done for the nanoparticles synthesised using aqueous method, i.e. centrifugation using acetone as discussed in detail in section 3.1.2. The amount of initial Nafion concentration was kept at 30 times of the metal content in the precursor. This value was selected based on the TGA studies discussed in section 4.1.1.

Different type of nanoparticles were synthesised in this case by changing the amount of the reducing agent from 4 times to 20 times excess of the stoichiometric amount needed to the reduce both Pt and Cr precursor. The nanoparticles were thus labelled as Pt-Cr 4, Pt-Cr 8, Pt-Cr 10 and Pt-Cr 20, depending on the amount of reducing agent. The characterisation techniques used to study the amount of Nafion, morphology, size and composition of the particles as well as the oxidation states of the elements are discussed below.

4.2.1 Thermogravimetric Analysis (TGA)

As discussed in section 4.1.1., the amount of Nafion and Pt-Cr is very important in the preparation of catalyst inks since it has a direct effect on the electrochemical behaviour of these catalysts. All the experiments were done in the presence of air (with N_2 as the carrier gas) to decompose the Nafion and 4 tests were carried for each sample to check the repeatability of the test.

Figure 4.8 shows the thermo gravimetric curves for the various Nafion-stabilised Pt-Cr nanoparticles synthesised using different amount of reducing agent and compared to pure Nafion to calculate the amount of Nafion present. The decomposition behaviour of pure Nafion has already been discussed in section 4.1.1. The different samples of Pt-Cr on Nafion behaved in a similar way showing the decomposition of Nafion from 75-500 °C with a steep change in mass after 450 °C. However, the slope of the decomposition region before 450 °C is different for all the samples. This is due to the breakage of side chains of Nafion during the synthesis process and it is discussed in better detail with the help of XPS results in section 4.2.4. So, the side chains maybe present in different amounts in the samples and thus cause the change in slope. The amount of Nafion is calculated using the mass loss between the two dotted lines shown in the Figure 4.8 and it follows the trend Pt-Cr 10 < Pt-Cr 4 < Pt-Cr 20 <

Pt-Cr 8. Thus, the amount of metal present will follow the opposite trend with Pt-Cr 10 showing the highest amount. The average amount of metal present in the samples was found to be 55% > 48% > 43% > 42% for Pt-Cr 10, Pt-Cr 4, Pt-Cr 20 and Pt-Cr 8, respectively. These samples were repeated a minimum of three times and the error in the residual mass was ±1%.

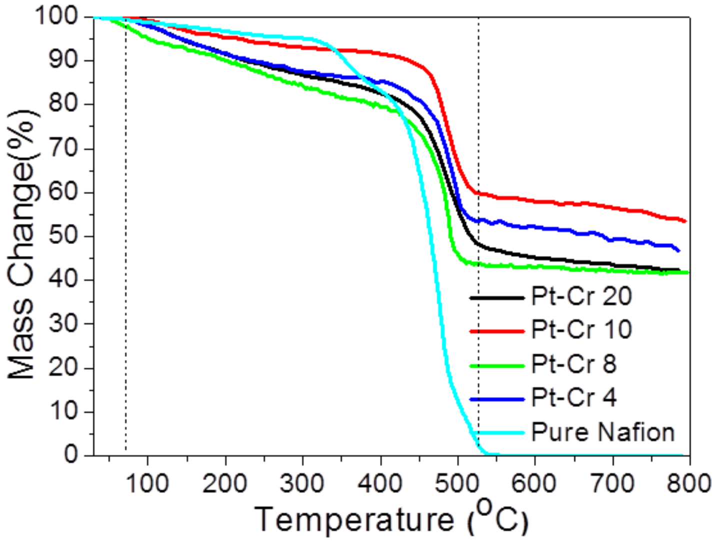

Figure 4.7: Thermo gravimetric curve of pure Nafion and Nafion-stabilised Pt-Cr nanoparticles with different amounts of reducing agent.

4.2.2 Transmission Electron Microscopy (TEM)

TEM coupled with EDS is a very useful technique to study the particle size, morphology, distribution as well as the composition of the nanoparticles. This technique is used in the present case as the different nanoparticles were synthesised by varying the amount of reducing agent and thus a change in the size, distribution and composition was expected. From the TGA results, it was observed that the final amount of Nafion and Pt-Cr was different for all the samples. TEM analysis can give a better insight into the structure and composition of the nanoparticles which can explain the difference in the amount of Pt-Cr.

Figure 4.9 shows the TEM images, energy dispersive spectroscopy (EDS) and diffraction patterns for different catalysts synthesised using borohydride reduction in ethanol solvent. Figures 4.9 (a, d, g and j) show the bright-field TEM images of the Pt-Cr 4, Pt-Cr 8, Pt-Cr 10 and Pt-Cr 20 samples, respectively. In all these images, a common feature observed was the agglomeration of nanoparticles. Such agglomeration of nanoparticles has already been reported in literature with the use of Nafion as the stabiliser [2, 8, 24]. Therefore, we conclude that Nafion acts as a binder in our case too. Nanoparticles with variable size distribution (shown as inset on the TEM bright-field images) from 4 to 10 nm have been observed in our case with a large fraction of particles around 6 ± 2 nm, indicating good control over the particle size using borohyrdide reduction.

Figure 4.9 (b) shows the EDS spectrum obtained on the nanoparticles shown in figure 4.9 (a), which were produced using a reducing agent ratio of 1:4. No Cr peak is observed in the EDS spectrum, indicating very limited or no reduction of Cr precursor. This observation is in agreement with the TEM analysis reported in section 4.1.2. This is attributed to a large difference in the driving force for the reduction process with respect to the Pt and Cr precursors. Moreover, the current reduction process only uses low temperature conditions and relatively weak reducing agents. Consequently, Pt which has a higher redox potential is preferentially reduced first, whereas the Cr precursor still struggles to fully attain the metallic state [11].

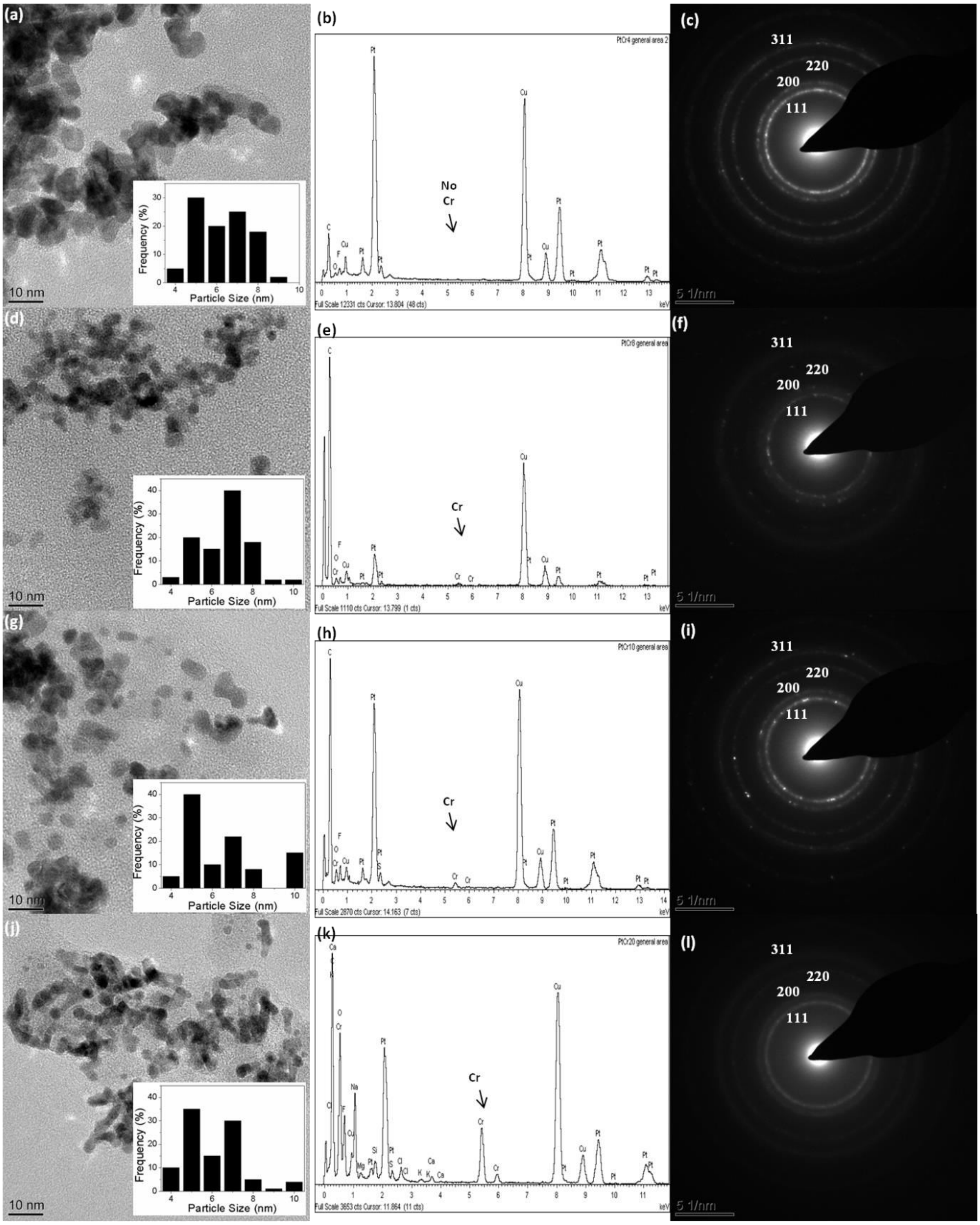

Figure 4.9: The bright field TEM image, EDS and diffraction patterns for: (a-c) Pt-Cr 4; (d-f) Pt-Cr 8; (g-i) Pt-Cr 10; (j-l) Pt-Cr 20.

Figure 4.9 (e) shows the EDS spectrum on the nanoparticles shown in figure 4.9 (d), synthesised using reducing agent ratio of 1:8. The results show presence of Cr in the amounts of 10-15 at.% and thus prove that with the use of excess reducing agent, the redox barrier for the reduction of Cr precursor to metallic Cr can be overcome as has been reported by Jeon *et al.* [12]. However, Cr is not distributed evenly over the whole area which was evident from certain regions which were rich in Pt only. The distribution of Cr was not possible to obtain due to its presence being in very low amount as compared to the Pt and Nafion. Thus, EDS spectra were taken over different areas and particles to get a statistical estimate of Cr. The EDS results showed the presence of mixture of Pt and Pt-Cr nanoparticles. These nanoparticles should be able to highlight the effect of Cr on the electrochemical behaviour of the catalyst.

Figure 4.9 (h) shows the EDS spectrum of the nanoparticles shown in figure 4.9 (g). The results confirmed the presence of Cr in the nanoparticles and it was estimated to be 30 at.%. The regions which showed Pt with no Cr were very low in number as compared to Pt-Cr 8 sample. In order to increase the Cr content using this method, the synthesis was tried using higher reducing agent i.e. 1:20 and the EDS pattern obtained is shown in figure 4.9 (k) on the nanoparticles shown in figure 4.9 (j). However, the amount of Cr present in this case was only 20 at.% which was less than that obtained using 1:10 reducing agent. This may be due to the reduction of Cr at a faster rate relative to Pt causing the surface enrichment of Pt. Jeon *et al.*[12] also observed the similar effect with the increase in $NaBH_4$ concentration for PtNiCr alloys and Hyun *et al.*[25] for PtRu alloys.

Figure 4.9 (c, f, i, l) shows the diffraction patterns corresponding to nanoparticles shown in figure 4.9 (a, d, g, j), respectively for the samples Pt-Cr 4, Pt-Cr 8, Pt-Cr 10 and Pt-Cr 20. From the diffraction ring patterns, lattice parameter for each of the specimen has been estimated to be in the range of 3.85-3.92 Å. As the observed lattice parameters are closer to that of Pt (3.92 Å) [9], it is assumed that the nanoparticles also have a face centred cubic structure like Pt and the rings have been indexed as 111, 200, 220, 311 respectively, as shown in the figure 4.9. The lattice parameters for all the samples are reported in table 4.3 which shows that with the increase in the Cr amount i.e. for sample Pt-Cr 10 and Pt-Cr 20, the lattice parameter value decreased. This change suggests alloying of Pt and Cr.

Thus, it can be inferred from the TEM analysis that agglomerated network of nanoparticles are synthesised in all the cases with an average particle size of 6 ± 2 nm. The alloy formation took place in Pt-Cr 8, Pt-Cr 10 and Pt-Cr 20 whereas the degree of alloying cannot be confirmed and needs further analysis. Also there were regions which contain only pure Pt nanoparticles.

Table 4.3: Parameters calculated from TEM and XRD

Sample	**Particle size (TEM) nm**	**Particle size (XRD) nm**	**Lattice Parameters (TEM) Å**	**Lattice Parameters (XRD) Å**
Pt/C	5 ± 1	6	3.92	3.92
Pt-Cr 4	6 ± 2	6	3.92	3.92
Pt-Cr 8	6 ± 2	5	3.90	3.91
Pt-Cr 10	6 ± 2	5	3.89	3.90
Pt-Cr 20	6 ± 2	4	3.85	3.89

4.2.3 X-ray Diffraction (XRD)

As discussed in the section 4.1.3, XRD is a useful technique to study the crystalline structure of the nanoparticles as well as the particle size which is complimentary to the electron diffraction analysis from TEM. The nanoparticles showed presence of alloying in some cases as discussed in the TEM results in section 4.2.2 and XRD can give confirmation of the alloy formation with the change in the peak positions and broadening of the peaks. The nanoparticles size and lattice parameters of the different samples can also be calculated using XRD.

Figure 4.10 shows the X-ray diffraction graphs obtained for the different catalysts synthesised using borohydride method with ethanol as solvent and compared to the Pt/C commercial catalyst. It can be observed from the graph that the position of Pt (111) peak at 39.8 is similar for all samples and thus the degree of alloying cannot be confirmed from peak position. Further, broadening of the Pt peaks was also observed as we increase the amount of reducing agent. The particle size calculated from the curves using the Scherer equation which takes into account the FWHM for these catalysts is shown in table 4.3. There was slight change in the particle size and it varies from 4-7 nm for all the catalysts. The results relates well with the particle size calculated from the TEM analysis discussed in section 4.2.2 even though agglomeration of particles was observed. From both XRD and TEM, the particle size varies in a range from 4-10 nm. Alloying also affects the broadening as has been reported for Pt-Ru system by Hyun *et al.* [25] that with the increase in the content of Ru, the Pt peak height decreases and broadening of the peaks occur due to alloying. They also reported that degree of alloying increases with the increase in reducing agent. Jeon *et al.* [12] also reported peak broadening and height reduction for Pt in PtNiCr system with the increase in the concentration of reducing agent. The diffusion of peaks was also observed at very higher concentration of reducing agent which is not present in our case. The authors also reported that the degree of alloying increased with increasing the amount of reducing agent. However, the authors did not confirm the extent of alloy formation as the peak positions for Pt did not show much variations. The peak broadening was attributed to the formation of alloys of PtNiCr. In present study, the effect of particle size and alloying cannot be differentiated due to the wide range 4-10 nm in the particle size which is the average particle size of all the samples. Thus, the broadening can be related to both changes in particle size as well as alloying.

Hence, we can say that alloying happens in our Pt-Cr system and degree of alloying should follow the trend Pt-Cr 8> Pt-Cr 10> Pt-Cr 20 but the extent of alloying is not clear. The lattice parameters are calculated for all the samples and reported in the table 4.3, and they are slightly different from the lattice parameters obtained from the TEM analysis. However, the small difference in the lattice parameters can be due to different instruments and the accuracy of the measurement. From the XRD results, it can be confirmed that alloying is present in the case of Pt-Cr 8, Pt-Cr 10 and Pt-Cr 20 samples, however the extent of alloying is still not clear.

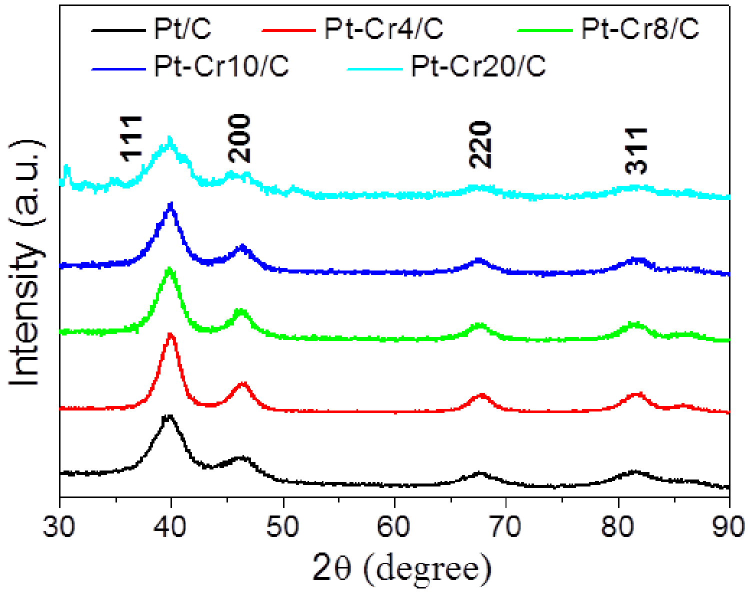

Figure 4.10: XRD graphs of different alloy catalysts

4.2.4 X-ray Photoelectron Spectroscopy (XPS)

It has been discussed in section 4.1.4 that XPS is a surface sensitive technique which is useful to study the atomic composition and oxidation states of the elements present in a sample. From the XRD and TEM results discussed in section 4.2.2 and 4.2.3, respectively, it has been inferred that alloying of Pt-Cr has taken place. However, extent of alloying and the oxidation states of the Pt and Cr is not clear and XPS can give a better insight into this and can also confirm the presence of Nafion which will also substantiate the TGA results.

Figure 4.11 shows the survey spectrum for different catalysts which have been synthesised using borohydride reduction in the ethanol solvent. The peaks corresponding to Pt, Cr and Nafion (C, F, and O) can be seen. It can also be seen that minor impurities of Na is present which is less than 5 at. % (less than 1 wt. %) and thus, should not affect the properties of the nanoparticles. The confirmation of the oxidation states of these elements can be done by peak fitting of the high resolution elemental spectrum. The elemental analysis was done and the amounts of different elements are reported in table 4.4. The ratio of Pt: Cr calculated for all samples prepared has been reported in table 4.5.

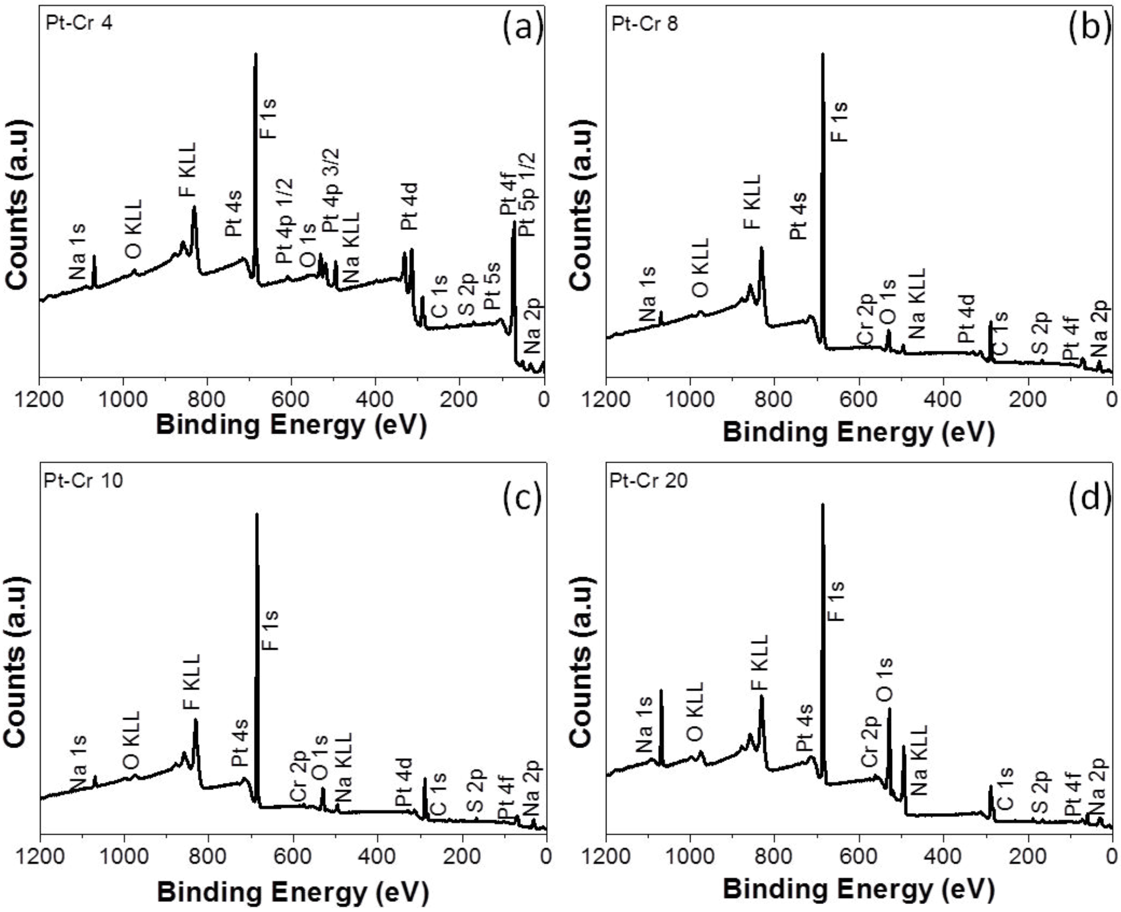

Figure 4.11: Survey XPS spectra for different catalysts.

Table 4.4: Atomic percentage of different elements present in the catalysts

Sample **Elements**	**Pt-Cr 4**	**Pt-Cr 8**	**Pt-Cr 10**	**Pt-Cr 20**
Pt (at. %)	5	0.6	0.6	0.6
Cr (at. %)	0	0.2	0.3	0.2
C (at. %)	34	33	35	33
O (at. %)	8	8	9	20
F (at. %)	49	55	53	40
Na (at. %)	3	1.4	1.1	5.4
S (at. %)	1	1.8	1.1	0.8

Table 4.5 shows that Cr content in the as-synthesised samples increases in the following order Pt-Cr 4< Pt-Cr 8< Pt-Cr 10 which is directly proportional to the amount of reducing agent i.e. as reducing agent increases, Cr content in the sample increases. It can also be observed that no reduction of Cr precursor took place for the sample Pt-Cr 4 (absence of Cr peak in figure 4.11(a)) which is in agreement with the results obtained for Pt-Cr reported in section 4.1.4. This confirms that the reduction reaction has taken place completely for Pt precursor while the Cr precursor was not reduced due to higher reduction barrier for Cr. This is in agreement with the TEM results discussed in section 4.2.2. Even after increasing the concentration of the reducing agent by 20 times, the amount of Cr was only 20-30 at. %. This shows that the redox potential makes a huge difference for the reduction of Cr precursor and also a very high amount of energy is needed for this reduction reaction. It can be seen from table 4.5 that with the increase in the amount of reducing agent, the Cr content increases which is due to increase in reduction rate of Cr. However, the Cr content is decreased for Pt-Cr 20 sample; this is due to the fast reduction rate of Cr relative to Pt causing Pt enrichment on the surface. This behaviour has been observed by Jeon *et al.*[12] for PtNiCr system and Hyun *et al.*[25] for Pt-Ru system. This results correlates well with the TEM analysis as discussed in section 4.2.2. Only very small area in the range of few nm was used for XPS analysis, it can be concluded that Pt-Cr were present in close vicinity and thus suggest a strong possibility of alloy formation in the case of Pt-Cr 8, Pt-Cr 10 and Pt-Cr 20 samples.

Table 4.5: XPS Ratio of Pt:Cr obtained for the different catalysts

Sample	Ratio of Pt:Cr
Pt-Cr 4	100:0
Pt-Cr 8	80:20
Pt-Cr 10	70:30

Pt-Cr-20	80:20

Figure 4.12 shows the Pt 4f XPS spectrum obtained for the different catalysts synthesised in this study and the peak fitting for the different components. It can be clearly seen from the fitting that the spectra consisted of only pure Pt and no Pt^{2+} or Pt^{4+} peaks are present. This can be attributed to the presence of Cr in the system which has the tendency to oxidise more quickly, thus preventing the oxidation of Pt. The lower binding energy doublet with Pt 4f 7/2 at 71.2 eV (Pt-Cr 4), 71.2 eV (Pt-Cr 8), 71.2 eV (Pt-Cr 10), 71.1 eV (Pt-Cr 20) for all the catalysts agrees well with the published value of Pt metal at 71.1 eV [16, 23, 26-29].

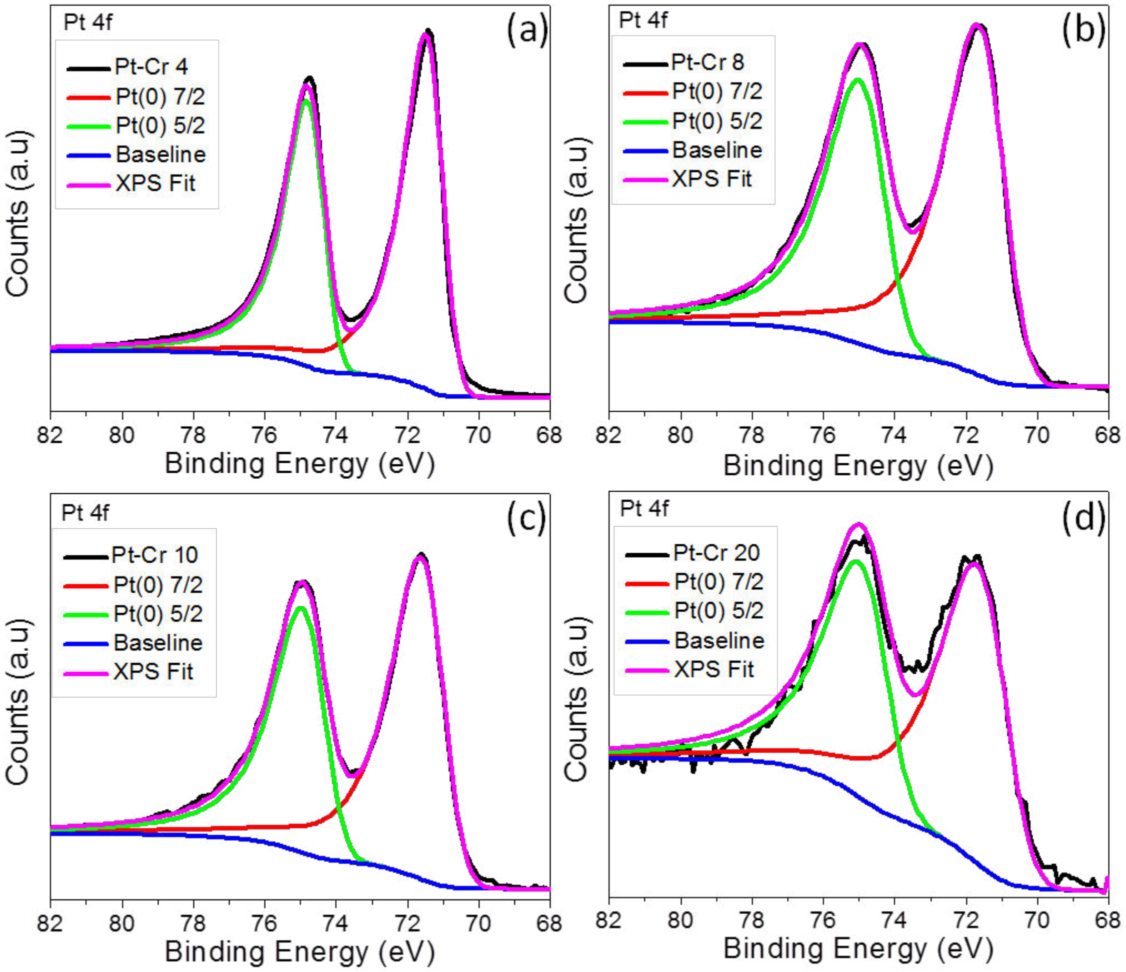

Figure 4.12: XPS spectra of Pt 4f for different catalysts.

Figure 4.13 shows the XPS spectra of Cr 2p for the different catalysts which have been synthesised in this study. There was no Cr observed in the case of Pt-Cr 4 and the spectrum is a flat line (figure 4.13(a)). From the spectra, it is clear that Cr species has two components which were identified as Cr^0 and Cr^{3+} [30]. Table 4.6 shows the relative intensity for these components at the binding energy for Cr 2p 3/2. This can give a clear idea of the amount of oxide and pure metal present. It can be seen that the amount of oxide in case of Pt-Cr 20 increase as compared to Pt-Cr 8 and Pt-Cr 10 samples.

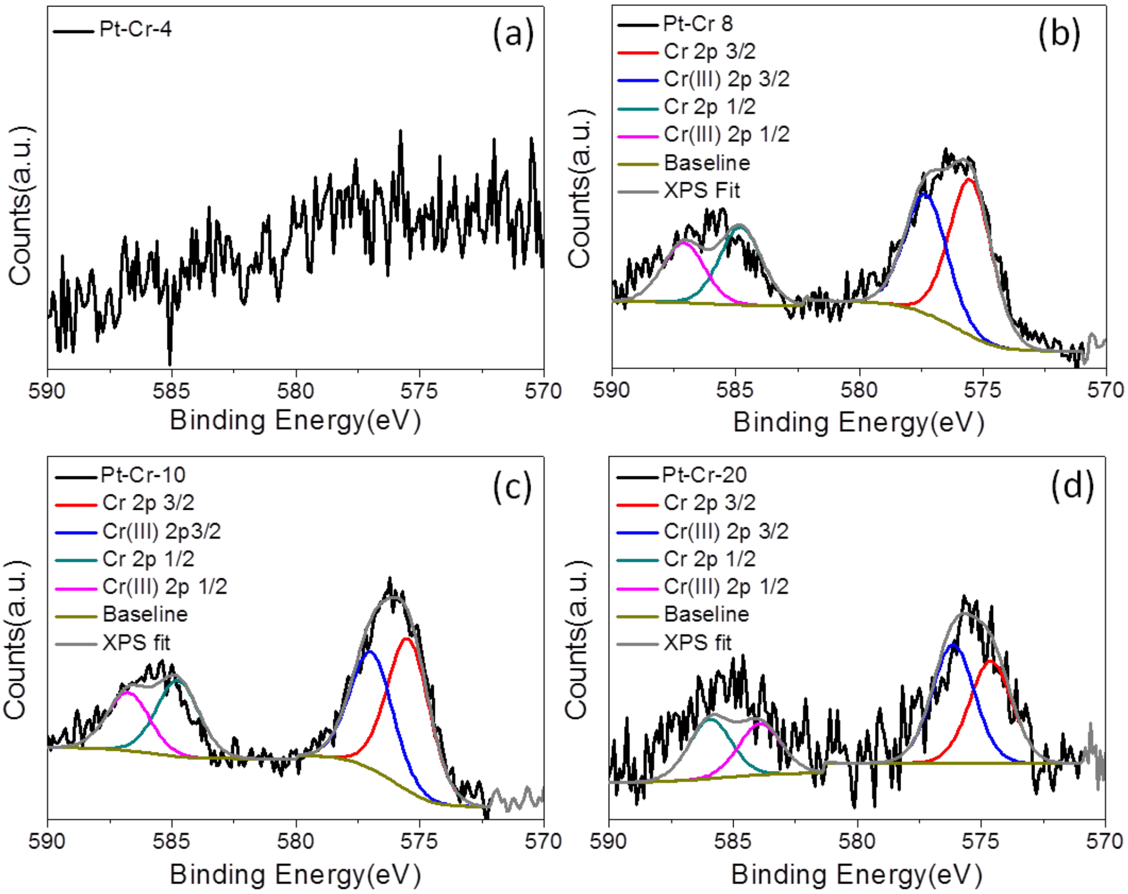

Figure 4.13: XPS spectra of Cr 2p for different catalysts

Table 4.6: Binding energies and relative intensities of different Cr components as observed from Cr 2p XPS spectra of different electrocatalysts as shown in figure 4.13

Sample	Components	Binding Energy of 2p 3/2 eV	Relative Intensity %
Pt-Cr 8	Cr	575.51	56.6
	Cr^{3+}	577.31	43.4
Pt-Cr 10	Cr	575.47	56.5
	Cr^{3+}	576.96	43.5
Pt-Cr 20	Cr	574.62	46.3
	Cr^{3+}	576.13	53.7

Figure 4.14 shows the XPS spectra for C 1s for the different Pt-Cr catalysts. Peak fitting was done using CASA XPS. The different components compare well with the structure of the Nafion which contains the CF_2, CF_3, CF, C-O, C-S bonds. The peak positions of the components present in the different catalysts is given in the table 4.7. The presence of C 1s component around 285 eV is due to disintegration of the Nafion during the synthesis which removes the side chains and it has been observed in the TGA analysis also as discussed in section 4.2.1. The various components are present in different concentration for the different samples that are due to the use of varying amount of reducing agent during the synthesis process. It follows the trend with the addition of C-C peak and the reduction of CF_3 and CF peaks which are present in the side chains. The presence of C-C peak suggests that even though the side chains of the Nafion are breaking, the broken chains are still attached with the nanoparticles or left trapped in the Nafion chains and thus form the part of the structure. The exact amount of breakage is not known. However, a trend emerges which is the increase of the C-C, C-S component as we increase the concentration of reducing agent. It even causes the splitting of the C-O/C-S component into two identifiable peaks in the case of sample which is prepared by the use of 20 times of the excess reducing agent that is attributed to the

breakage of the sulfonate chains. This mechanism can be further analysed from the XPS spectra of the O 1s which can give the ratio of the sulfonates and ether groups.

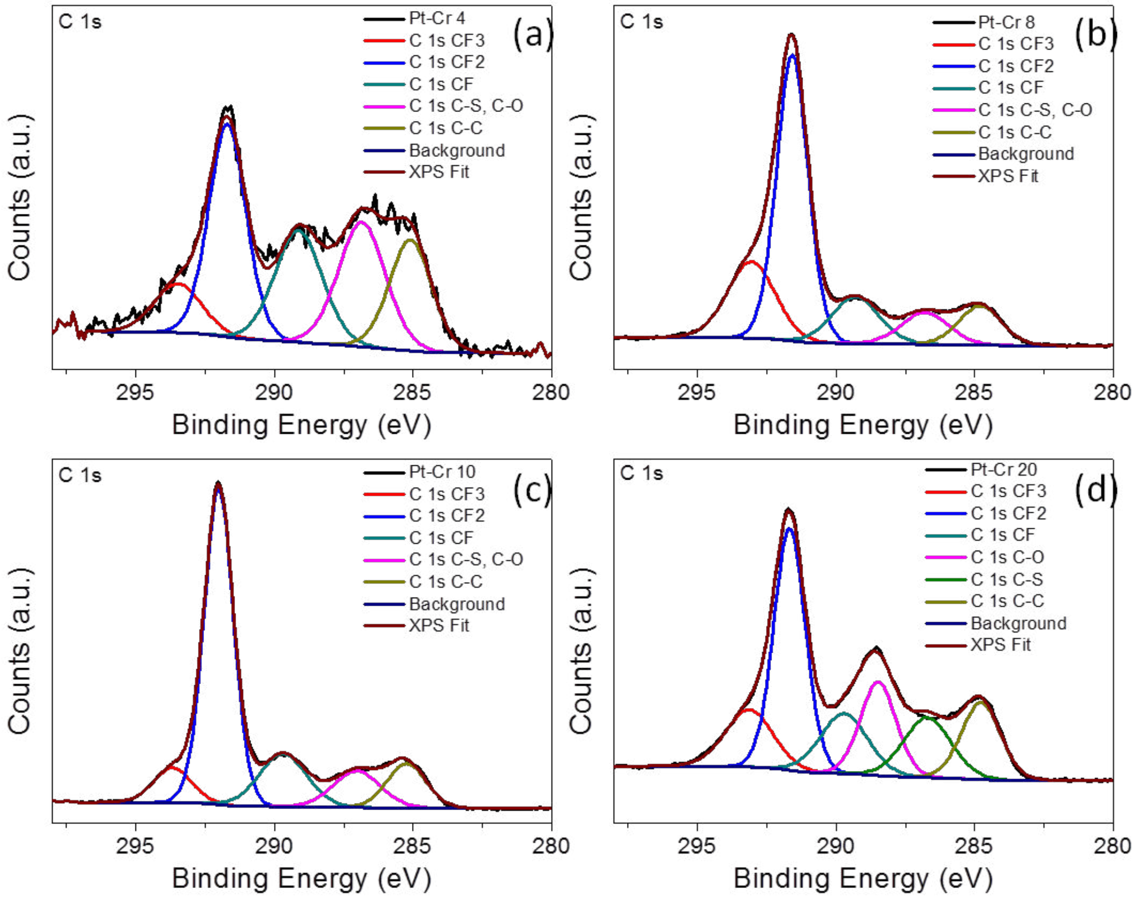

Figure 4.14: XPS spectrum of C 1s for different catalysts

Table 4.7: Binding energies of different C components for the catalysts

Component Sample	CF_3 (eV)	CF_2 (eV)	CF (eV)	C-O, C-S (eV)	C-C (eV)
Pt-Cr 4	293.4	291.7	289.1	286.9	285.1
Pt-Cr 8	293.1	291.6	289.3	286.8	284.8
Pt-Cr 10	293.6	292	289.7	287	285.2
Pt-Cr 20	293.1	291.7	289.7	288.5,286.7	284.8

Figure 4.15 shows the XPS spectra for F 1s for the different catalysts synthesised in this study and the various components that can be fitted. The main component present in all the samples is p-(CF_2=CF_2) which is basic building block in the Nafion structure and thus further confirms the presence of Nafion in all the samples[14]. The origin of the peak at 684 eV is not well understood and thus I do not want to speculate further at this point.

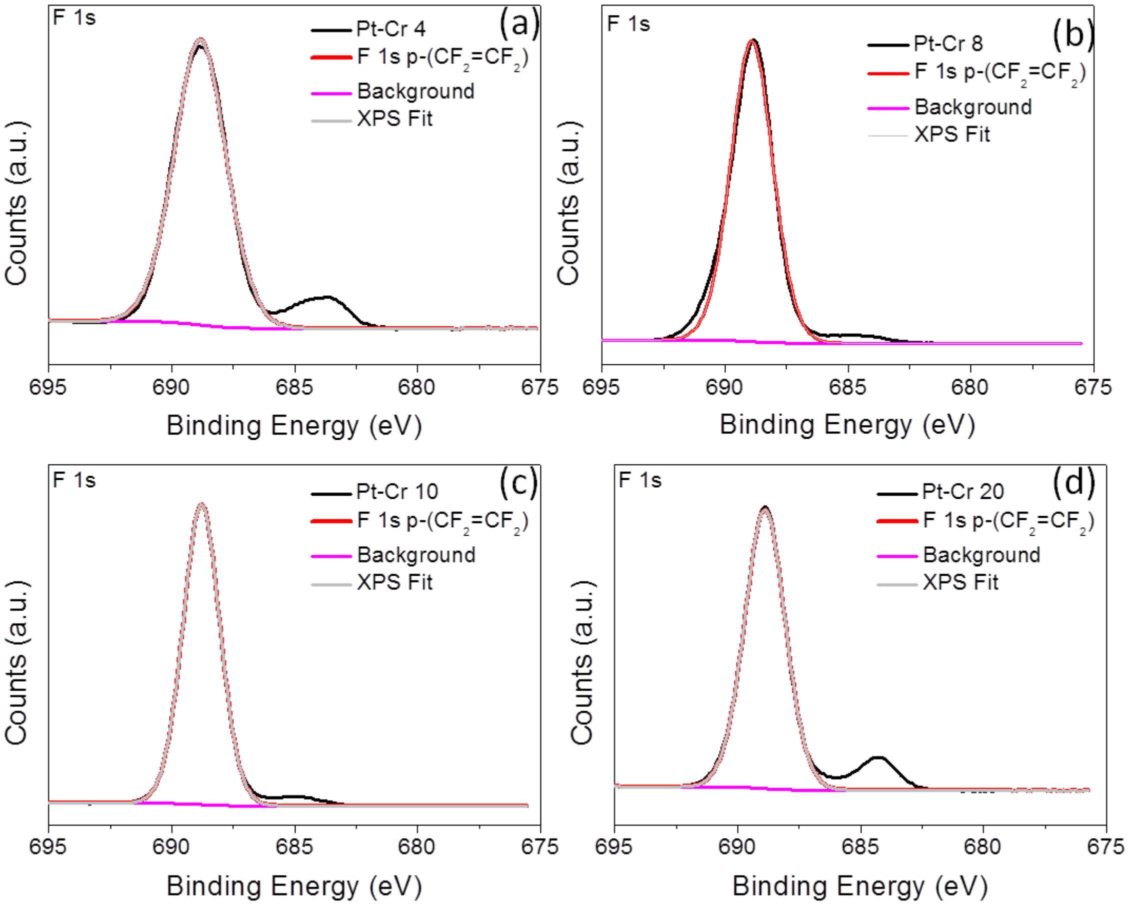

Figure 4.15: XPS spectra of F 1s for different catalysts

Figure 4.16 shows the XPS spectra for O 1s obtained for different catalysts and the different components were fitted. It can be seen that all the catalyst have three components and the details of these component have been reported in table 4.8. The different components in this system arises due to sulfonates (O 1s_2), ethers (-(C-O-C)- O 1s_3) at binding energies between 532-535 eV and metal oxide (O 1s_1) like species are reported at binding energies around 530 eV [22, 31]. In Pt-Cr 4 sample, no metal oxide was present and O1s_1 was close to 531 eV which corresponds to the hydroxide peak and it can be assumed that the peak is coming from the residual water content present in the Nafion. Table 4.8 clearly shows that the amount of metal oxide increased with the increase in the amount of Cr. Even though the amount of Cr was less in the sample with 20 times reducing agent, the oxide content was higher which is clear from the spectrum for Cr discussed above.

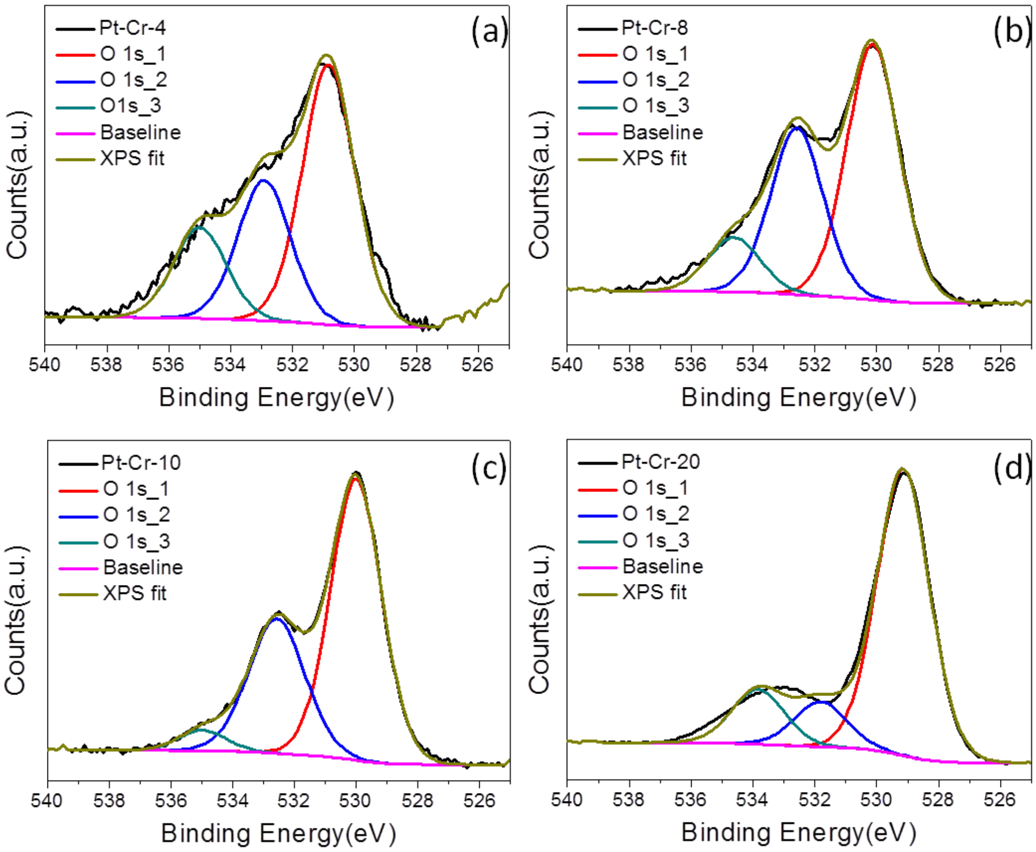

Figure 4.16: XPS spectra for O 1s for different catalysts

It is interesting to note the change in the concentration of the sulphonates and ether groups with the increase in the reducing agent. With the increase in the reducing agent, the concentration of ether groups decreases and reaches a minimum for the Pt-Cr 10 sample. This further confirms the breakage of the side chains or ether bonds as discussed during the analysis of C 1s peaks and thus giving rise to more C-C bonds. This has been reported in literature that the ether bonds and sulfonates bonds breaks during the decomposition of Nafion [14, 15, 22, 32]. For the Pt-Cr 20 samples, there is drastic reduction in the sulfonate peak which can be due to the breakage of the sulfonic group present in the side chain of Nafion structure and the rearrangement of the C-S bonds which was observed with the splitting of the C-S, C-O peak for the same sample in the C 1s spectrum.

Table 4.8: Binding energies and relative intensities of different oxygen components as observed from O 1s spectra of different electrocatalysts as shown in figure 4.16

Sample	**Components**	**Binding Energy of O1s eV**	**Relative Intensity %**
Pt-Cr 4	-OH	530.8	52
	$-SO_3H$	532.9	28
	-(C-O-C)	535	18
Pt-Cr 8	M-O	530.1	53
	$-SO_3H$	532.6	35
	-(C-O-C)	534.6	12
Pt-Cr 10	M-O	530	64
	$-SO_3H$	532.6	31
	-(C-O-C)	534.8	5
Pt-Cr 20	M-O	529.1	74
	$-SO_3H$	531.8	12
	-(C-O-C)	533.8	14

From the XPS analysis discussed above, it can be said that with the increase in the reducing agent, Cr concentration increased upto 30 at.% in the case of Pt-Cr 10. With the further increase in the amount of reducing agent, the rate of reaction for Cr reduction increased relative to Pt and the surface enrichment of Pt occurred and thus we get a higher concentration of Pt i.e. 80 at.% in case of Pt-Cr 20. Also, there is strong possibility of formation of an alloy of Pt and Cr in the case of Pt-Cr 8, Pt-Cr 10 and Pt-Cr 20.

4.3. Conclusions

An attempt to synthesise Nafion-stabilised PtCr nanoparticles aqueous solvent using sodium borohydride as reducing agent has been reported. The average particle size of the nanoparticles was estimated to be 6 ± 2 nm (TEM) compared to 5 ± 1 nm (TEM) for Pt/C. The lower particle size for Pt/C may result in higher surface area and better electrochemical properties. There were only traces of Cr present in the nanoparticles and no alloy formation was observed which was confirmed from the XRD, XPS and TEM analysis. Thus, there was a need for change in the synthesis method.

Nafion-stabilised Pt-Cr alloy nanoparticles were successfully synthesised using borohydride reduction method with ethanol as the solvent. When the amount of reducing agent was low, Cr precursor was not reduced and thus the need for higher reducing agent to overcome the redox barrier. The nanoparticles were agglomerated in all the cases with an average particle size of 6 ± 2 nm (TEM), 4-6 nm (XRD). The broadening of peaks in the XRD graphs, EDS analysis and XPS confirmed the possibility of alloy formation in case of Pt-Cr 8, Pt-Cr 10 and Pt-Cr 20 samples. The degree of alloying was not confirmed and need further studies. The presence of Nafion was confirmed from the TGA and XPS analysis and from the bright field TEM images agglomeration of the nanoparticles was observed which is due to the binding of the nanoparticles with Nafion. Pt was present in metallic form due to the presence of Cr which gets oxidised first and thus prevents Pt from oxidation as seen by the high resolution XPS spectra for Pt 4f.

Nafion decomposition was also observed during the synthesis process. This was confirmed by the TGA analysis that showed the change in slope of the curve below 450 °C. XPS analysis also confirmed the decomposition of Nafion i.e. breaking of side chains which resulted in the presence of C-C and reduction of side chains. The presence of C-C peak suggests that even though the side chains of the Nafion are breaking, the broken chains are still attached with the nanoparticles or left trapped in the Nafion chains and thus form the part of the structure.

References

1. Takahashi, I. and S.S. Kocha, *Examination of the activity and durability of PEMFC catalysts in liquid electrolytes.* Journal of Power Sources, 2010. **195**(19): p. 6312-6322.
2. Sarma, L.S., et al., *Carbon-supported Pt–Ru catalysts prepared by the Nafion stabilized alcohol-reduction method for application in direct methanol fuel cells.* Journal of Power Sources, 2005. **139**(1-2): p. 44-54.
3. Liu, Z., Z.Q. Tian, and S.P. Jiang, *Synthesis and characterization of Nafion-stabilized Pt nanoparticles for polymer electrolyte fuel cells.* Electrochimica Acta, 2006. **52**(3): p. 1213-1220.
4. Baturina, O.A., S.R. Aubuchon, and K.J. Wynne, *Thermal Stability in Air of Pt-C Catalysts and PEM Fuel Cell Catalyst Layers.* Chem Mater, 2006. **18**(1498-1504).
5. Chu, D., et al., *Infrared reflectance absorption spectroscopy (IRRAS). Study of the thermal stability of perfluorinated sulphonic acid ionomers on Pt.* Journal of Applied Electrochemistry, 1990. **20**(1): p. 157-162.
6. Surowiec, J. and R. Bogoczek, *Studies on the thermal stability of the perfluorinated cation-exchange membrane Nafion-417.* Journal of thermal analysis, 1988. **33**(4): p. 1097-1102.
7. Samms, S.R., S. Wasmus, and R.F. Savinell, *Thermal Stability of Nafion® in Simulated Fuel Cell Environments.* Journal of The Electrochemical Society, 1996. **143**(5): p. 1498.
8. Curnick, O., *Ionomer-Stabilised Pt and Pt-Ti Bimetallic Electrocatalysts for the Proton Exchange Membrane Fuel Cell*, in *Chemical Engineering*2012, University of Birmingham, UK: Birmingham, UK. p. 230.
9. Cullity, B.D., *Elements of X-ray diffraction*. 1956, Reading, Massachusetts: Addison-Wesley Publishing Company, Inc.
10. Suryanarayana, C. and M.G. Norton, *X-Ray Diffraction: A Practical Approach*. 1998, New York: Plenum Press.
11. Yang, H., et al., *Tailoring, Structure, and Activity of Carbon-Supported Nanosized Pt−Cr Alloy Electrocatalysts for Oxygen Reduction in Pure and Methanol-Containing Electrolytes.* The Journal of Physical Chemistry B, 2004. **108**(6): p. 1938-1947.
12. Jeon, M.K., Y. Zhang, and P.J. McGinn, *Effect of reduction conditions on electrocatalytic activity of a ternary PtNiCr/C catalyst for methanol electro-oxidation.* Electrochimica Acta, 2009. **54**(10): p. 2837-2842.
13. Martínez de Yuso, M.V., et al., *A Study of Chemical Modifications of a Nafion Membrane by Incorporation of Different Room Temperature Ionic Liquids.* Fuel Cells, 2012. **12**(4): p. 606-613.
14. Schulze, M., et al., *XPS analysis of the degradation of Nafion.* Fresenius Journal of Analytical Chemistry, 1999. **365**(1-3): p. 106-113.
15. Huang, C., et al., *XRD and XPS analysis of the degradation of the polymer electrolyte in H2–O2 fuel cell.* Chemical Physics Letters, 2003. **371**(1-2): p. 80-85.
16. Moulder, J.F., et al., *Handbook of X-ray Photoelectron Spectroscopy*, ed. J. Chastein and J. Roger C. King. 1995, Minnesota, United States of America: Physical Electronics, Inc.
17. Ghassemzadeh, L., et al., *Chemical Degradation of Nafion Membranes under Mimic Fuel Cell Conditions as Investigated by Solid-State NMR Spectroscopy.* The Journal of Physical Chemistry C, 2010. **114**(34): p. 14635-14645.
18. Yu, T.H., et al., *Mechanism for degradation of Nafion in PEM fuel cells from quantum mechanics calculations.* J Am Chem Soc, 2011. **133**(49): p. 19857-63.
19. Chen, C., et al., *XPS investigation of Nafion® membrane degradation.* Journal of Power Sources, 2007. **169**(2): p. 288-295.
20. Chen, C. and T.F. Fuller, *The effect of humidity on the degradation of Nafion® membrane.* Polymer Degradation and Stability, 2009. **94**(9): p. 1436-1447.

21. Deng, Q., et al., *TGA–FTi.r. investigation of the thermal degradation of Nafion® and Nafion®/[silicon oxide]-based nanocomposites.* Polymer, 1998. **39**(24): p. 5961-5972.
22. López, G.P., D.G. Castner, and B.D. Ratner, *XPS O 1s binding energies for polymers containing hydroxyl, ether, ketone and ester groups.* Surface and Interface Analysis, 1991. **17**(5): p. 267-272.
23. Aricò, A.S., et al., *An XPS study on oxidation states of Pt and its alloys with Co and Cr and its relevance to electroreduction of oxygen.* Applied Surface Science, 2001. **172**(1-2): p. 33-40.
24. Curnick, O.J., P.M. Mendes, and B.G. Pollet, *Enhanced durability of a Pt/C electrocatalyst derived from Nafion-stabilised colloidal platinum nanoparticles.* Electrochemistry Communications, 2010. **12**(8): p. 1017-1020.
25. Hyun, M.-S., et al., *Effect of NaBH4 concentration on the characteristics of PtRu/C catalyst for the anode of DMFC prepared by the impregnation method.* Catalysis Today, 2008. **132**(1-4): p. 138-145.
26. Sharma, S., et al., *Rapid Microwave Synthesis of CO Tolerant Reduced Graphene Oxide-Supported Platinum Electrocatalysts for Oxidation of Methanol.* The Journal of Physical Chemistry C, 2010. **114**(45): p. 19459-19466.
27. Casella, I.G. and E. Desimoni, *XPS, SEM and electrochemical characterization of a platinum-based glassy carbon modified electrode. Electrocatalytic oxidation of ethanol in acidic medium.* Electroanalysis, 1996. **8**(5): p. 447-453.
28. Shukla, A.K., et al., *An XPS study on binary and ternary alloys of transition metals with platinized carbon and its bearing upon oxygen electroreduction in direct methanol fuel cells.* Journal of Electroanalytical Chemistry, 2001. **504**(1): p. 111-119.
29. Sarkar, A. and A. Manthiram, *Synthesis of Pt@Cu Core-Shell Nanoparticles by Galvanic Displacement of Cu by Pt4+ Ions and Their Application as Electrocatalysts for Oxygen Reduction Reaction in Fuel Cells.* Journal of Physical Chemistry C, 2010. **114**(10): p. 4725-4732.
30. Salvi, A.M., et al., *Peak fitting of the chromium 2p XPS spectrum.* Applied Surface Science, 1995. **90**(3): p. 333-341.
31. Aricò, A.S., et al., *Optimization of operating parameters of a direct methanol fuel cell and physico-chemical investigation of catalyst–electrolyte interface.* Electrochimica Acta, 1998. **43**(24): p. 3719-3729.
32. Hong, Y.-J. and S.M. Oh, *Fabrication of polymer electrolyte fuel cell (PEFC) H2 sensors.* Sensors and Actuators B: Chemical, 1996. **32**(1): p. 7-13.

Chapter 5
Electrochemical Characterisation of Nafion-stabilised Pt-Cr/C Catalysts

The characterisation of the different catalysts synthesised by borohydride reduction method in aqueous and ethanol solvents were discussed in the chapter-4. This chapter focuses on the electrochemical testing of these catalysts in 0.1 M $HClO_4$ which simulates the environment for the fuel cell testing. This section is divided into two parts

(a) Section 5.1: Electrochemical testing of PtCr/C (aqueous)

(b) Section 5.2 : Electrochemical testing of Pt-Cr/C (ethanol)

The synthesis of these catalysts using borohydride reduction method has been discussed in chapter-3 with different solvents. Each part consists of the analysis of different electrochemical testing procedures carried out, starting with the study of the electrochemical surface area of the catalyst which was done by the cyclic voltammetry. Then, the oxygen reduction reaction rate was studied by using linear sweep voltammetry and analysis was done using Koutecky-Levich and Tafel plots to report the specific activity and mass activity of the catalyst. As the alloys were obtained only in the case of ethanol based synthesis, these catalysts were further tested for degradation analysis and in-situ fuel cell testing.

5.1 Electrochemical Testing of PtCr/C Catalyst (aqueous)

Nafion stabilised Pt-Cr nanoparticles have been synthesised using borohydride reduction method with Nafion as a stabiliser and water as the solvent. The method has been described in chapter-3 under the section 3.1. The characterisation of these nanoparticles using different techniques was discussed in chapter-4 like thermogravimetric analysis, transmission electron microscopy, X-ray diffraction, X-ray photoelectron spectroscopy to study the composition, particle size, morphology of the nanoparticles and also the oxidation states of the elements present. The nanoparticles were supported on the Vulcan XC-72 to study the electrochemical behaviour as catalysts in fuel cells. Aliquot of the catalyst was dropped on the glassy carbon electrode that forms the working electrode. The working electrode was then tested in 0.1 M $HClO_4$ solution with reversible hydrogen electrode and a platinum mesh as reference and counter electrode, respectively. The detailed procedure has been discussed in section 3.3. A standard Pt/C (TKK) catalyst has been studied alongside these catalysts to compare the behaviour. The different electrochemical techniques used and the analysis is discussed below:

5.1.1 Cyclic Votammetry (CV)

Cyclic Voltammetry is a very useful electrochemical technique to study the various redox reaction or reversible reactions. One of the important parameter in the study of catalysts is the electrochemical surface area which can be determined by studying the hydrogen adsorption/desorption reaction. This region usually occurs between 0.0-0.4 V vs NHE and the area under the graph gives the charge of the monolayer of hydrogen desorbed which can be converted to electrochemical surface area using equation 3.1 as reported in section 3.3.

Figure 5.1 shows the cyclic voltammograms of Pt/C and PtCr/C in N_2 saturated 0.1 M $HClO_4$ solution at 25 °C with the current normalised to the geometrical surface area of the electrode (0.196 cm^2). The normal behaviour of hydrogen adsorption and desorption was clearly visible in both the catalysts in the potential range 0.05-0.4 V. Two different peaks were visible in this region which corresponds to Pt (110) and Pt (100) facets in the range 0.1-0.2 V and 0.2-0.3 V, respectively. The peak corresponding to Pt (110) peak was higher in the case of Pt/C confirming higher surface area Pt compared to PtCr/C. This was confirmed when considering the measured ECSA. The ECSA of both the catalyst were calculated using the equation reported in section 3.3.1.1 and is shown below also:

$$\text{ECSA}= \frac{Q_H}{210\ L_{Pt}A}$$

where Q_H (µC) is the charge measured upon desorption of hydrogen in the underpotentially-deposited (UPD) hydrogen region, L_{Pt} is the Pt loading (µg/cm^2), A is the geometric area of the working electrode (cm^2) and the value of 210 C/cm^2 corresponds to the charge required to adsorb/desorb a monolayer of H_2 on bulk polycrystalline Pt surface.

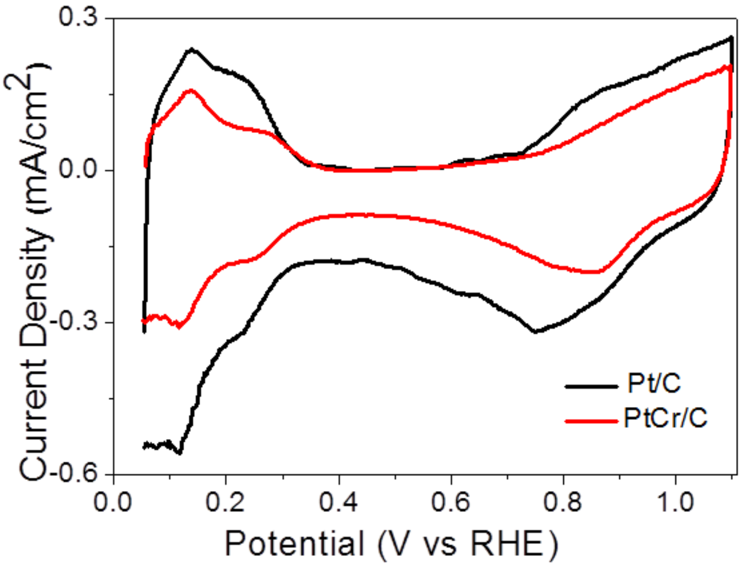

Figure 5.1: Cyclic Voltammograms of catalysts in 0.1M $HClO_4$ at 25 °C. Current normalised to the geometrical area of working electrode

The ECSA for Pt/C was determined to be 58 m^2/g_{Pt}, which is in agreement with the literature values [1, 2]. However, the ECSA of the PtCr/C catalyst was observed as 26 m^2/g_{Pt} which is considerably lower compared to Pt/C. This is possibly due to the agglomeration of the PtCr as reported in TEM images in section 4.2 (figure 4.3) which suggests the average particle size of 6 ± 2 nm as compared to 5 ± 1 nm for Pt/C catalyst (figure 4.2). However, Curnick *et al[3]* have reported higher ECSA (35 m^2/g_{Pt}) for the Nafion stabilised Pt/C synthesised by the same procedure. The reason for the variation in the performances of the two systems could be the presence of traces of Cr in current catalyst which needs to be investigated further. The double layer region for the PtCr/C is smaller as compared to the Pt/C, which shows less resistance for the transfer of the electrons and may contribute to the improved activity.

5.1.2 Oxygen Reduction Reaction (ORR)

ORR forms an important part of the catalyst study as it is the most sluggish reaction and forms the limiting step for the fuel cell operation. Thus, a lot of catalyst is being used on the cathode side to improve the ORR kinetics and in order to reduce the loading of Pt, alloys and core-shell structures are being studied. Linear sweep voltammetry (LSV) is a useful technique to study the ORR reaction mechanism which in turn can be used to calculate the performance of a catalyst by the use of Koutecky-Levich and Tafel plots. LSV curves are obtained in 0.1M $HClO_4$ solution with O_2 purging to study the ORR mechanism. The detailed procedure has been discussed in section 3.3.

Figure 5.2 shows the linear sweep voltammograms for Pt/C and PtCr/C in O_2 saturated 0.1 M $HClO_4$ solution. The current is normalised to the geometrical surface area of the electrode. This data has been subtracted from the LSV curves obtained for N_2 saturated solution and also normalised to IR drop. It is clear from the above figure that ORR is diffusion controlled below a potential of 0.7 V and beyond this ORR is controlled by mixed diffusion and kinetics in the potential region of 0.7- 1.0 V. The onset of ORR has slighted shifted to the higher potential in the case of PtCr/C which may contribute to the higher activity of this catalyst as compared to Pt/C.

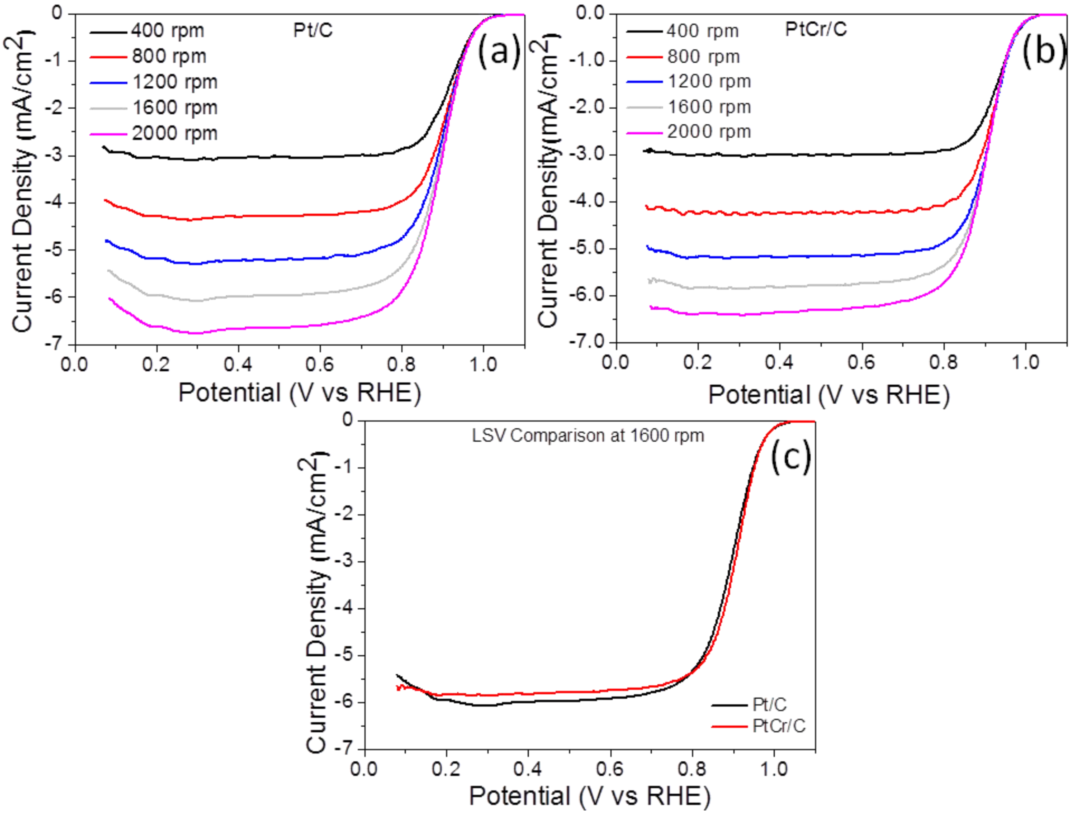

Figure 5.2: Linear Sweep Voltammograms of Pt/C (a) and PtCr/C (b) catalysts in 0.1M $HClO_4$ at 25 °C, (c) comparison at 1600 rpm. Current normalised to the geometrical area of working electrode

Furthermore, the Koutecky-Levich plots (figure 5.3) for these catalysts show a linear relationship between 1/I and $1/\omega^{-1/2}$. The slopes for these lines are same and the number of electrons calculated from the slopes is 4. This indicates that both these catalysts follow the same 4 electron reduction of oxygen leading to water formation. The slope is calculated using the Levich equation which is

$$I_{\mathrm{lim}} = 0.62\ n\ A\ F\ C\ D^{2/3} v^{-1/6}\ w^{1/2}$$

where I_{lim} is the limiting current, n is the number of electrons for the reaction, A is the electrode area (0.196 cm^2), F is Faraday's constant (96500 C/mol), C is the concentration (1.26×10^{-6} mol cm^{-3}), D is the diffusion coefficient of oxygen (1.93×10^{-5} cm^2/s), v is the kinematic viscosity (0.009 cm^2/s), and w is the rotation rate of the electrode.

It can also be seen from the figure 5.3(a) that the slope is similar for all the potential reported for Pt/C whereas the slope changes for the PtCr/C when it reaches the potential of 0.9 V that suggests the reaction kinetics is changing from 4 electrons process at that potential.

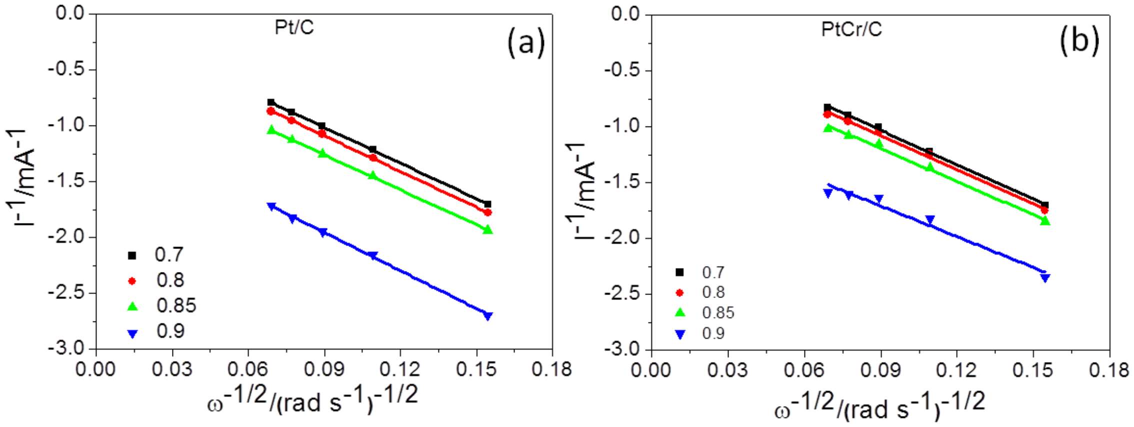

Figure 5.3: Koutecky-Levich graphs for (a) Pt/C and (b) PtCr/C

Figure 5.4 shows the Tafel plots for Pt/C and PtCr/C with the mass normalised kinetic current. Tafel slopes can be calculated from the figure which shows two regions. The Tafel slopes obtained at higher potentials (>0.9 V) for Pt/C and PtCr/C catalysts are 75 and 67 mV/decade, respectively. The Tafel slope did not show any dependence on the composition and structure of the catalysts and thus all the catalysts follow the same reaction pathway. It is evident from the figure that the specific activity (SA) of the catalyst presented in this work follows the order PtCr/C > Pt/C. The increase in the SA for PtCr/C at 0.9 V is almost three times that of Pt/C. The same order was followed for the mass activity, i.e. PtCr/C > Pt/C. All the electrochemical parameters calculated from the figures 5.1-5.4 are reported in table 5.1. It has been reported in literature for the Pt based alloys (Pt-Ni, Pt-Co, Pt-Cr etc.) that there is kinetic activity enhancement by a factor of 1.5-3 as compared to Pt [4]. However, since an alloy is not present in this case, the activity enhancement in PtCr/C is attributed to the improved triple phase boundary as Nafion is binding the PtCr which can be seen from the TEM images as shown in figure 4.2. This is in agreement with the results obtained by Liu *et al.* [5] for the Nafion stabilised Pt/C.

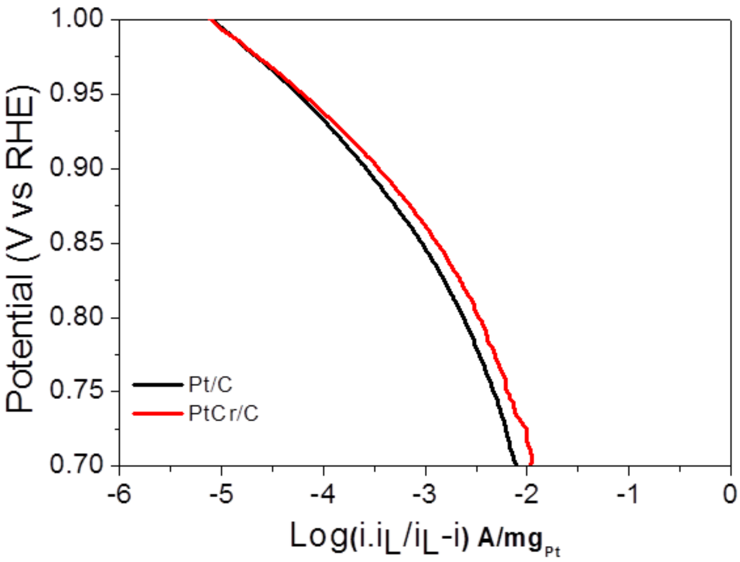

Figure 5.4: Tafel comparison for Pt/C and PtCr/C in 0.1M $HClO_4$ at 25 °C

Table-5.1: Electrochemical parameters calculated from figures 5.1- 5.4

	Pt/C	**PtCr/C**
ECSA (m^2/g$_{Pt}$)	58	26
Tafel Slope	75	67
Specific Activity at 0.9 V (mA/cm^2$_{Pt}$)	0.45	1.4
Mass Activity at 0.9 V (mA/mg$_{Pt}$)	260	350

5.2 Electrochemical Testing of Pt-Cr/C Catalyst (ethanol)

Nafion stabilised Pt-Cr nanoparticles were synthesised with Nafion as stabiliser in ethanol solvent using borohydride reduction method. The method has been described in details in chapter-3 under the section 3.1. These nanoparticles were characterised using different techniques as discussed in chapter-4 from section 4.2.1- 4.2.4 like thermogravimetric analysis, transmission electron microscopy, X-ray diffraction, X-ray photoelectron spectroscopy to study the composition, particle size, morphology of the nanoparticles and also the oxidation states of the elements present. After the purification of the nanoparticles, they were supported on the Vulcan XC-72 to study the electrochemical behaviour as catalysts in fuel cells. A working electrode was made by dropping aliquot of the catalyst ink on the glassy carbon electrode. The working electrode was then tested in 0.1 M $HClO_4$ solution with normal hydrogen electrode and a platinum mesh as reference and counter electrode, respectively. The detailed procedure has been discussed in section 3.3. A standard Pt/C (TKK) catalyst has been studied alongside these catalysts to compare the behaviour. The different electrochemical techniques used and the analysis is discussed below:

5.2.1 Cyclic Votammetry (CV)

As discussed in section 5.1.1 that CV is a very useful technique to study the reversible and redox reactions taking place in an electrochemical system. In the present case, CV is used to the study the electrochemical surface area (ECSA) of the Pt-Cr catalysts synthesised using borohydride reduction method as discussed in section 3.1. ECSA of the catalyst is calculating using equation 3.1 reported in section 3.3 and is given as

$$\mathrm{ECSA} = \frac{Q_H}{210\ L_{Pt}A}$$

where Q_H (µC) is the charge measured upon desorption of H2 in the underpotentially-deposited (UPD) hydrogen region, L_{Pt} is the Pt loading (µg/cm^2), A is the geometric area of the GCE (cm^2) and the value of 210 C/cm^2 corresponds to the charge required to adsorb/desorb a monolayer of H_2 on bulk polycrystalline Pt surface.

Figure 5.5 shows the cyclic voltammograms of different alloys of PtCr/C and commercial Pt/C in N_2 saturated 0.1 M $HClO_4$ solution at 25 °C. All the catalysts show the similar behaviour of hydrogen adsorption and desorption in the potential range of 0.05-0.4 V. This region can be identified easily for commercial Pt/C and Pt-Cr 4/C only as they show two different peaks in this region which corresponds to Pt (110) and Pt (100) facets in the range 0.1-0.2 V and 0.2-0.3 V, respectively. However, for the other alloys, there was no sharp peak and the bump for the second peak was more flat. The Pt (110) peak was sharper and higher in the case of Pt/C and Pt-Cr 4/C which contributes to the overall high surface area Pt in these catalysts whereas other Pt-Cr samples have a lower Pt surface area. The values for the electrochemical surface area were calculated using the equation which takes into consideration the area under the hydrogen desorption peak. The values obtained for all the catalysts are reported in the table 5.2. Table 5.3 shows the elemental distribution of Pt and Cr in the catalysts as calculated using TEM and XPS.

The utilisation of these catalysts was calculated as the ratio of electrochemical surface area to physical surface area. The physical surface was taken as an approximate from the particle size of 6 nm. Pt/C showed utilisation of around 80% whereas the alloy catalysts showed utilisation of 140% (Pt-Cr 4/C), 32% (Pt-Cr 8/C), 59% (Pt-Cr 10/C) and 41% (Pt-Cr 20/C). However, due to the amount of agglomeration present in the nanoparticles this is an approximate. A better utilisation calculation will be possible after reducing the amount of agglomeration in these nanoparticles.

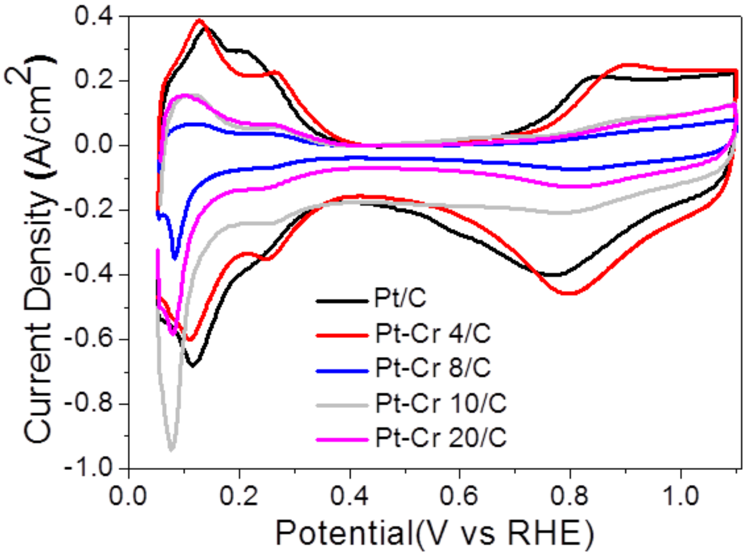

Figure 5.5: Linear CV graph of different catalyst in 0.1 M $HClO_4$ solution at 25°C. Current is normalised to geometrical surface area of working electrode

Table-5.2: Electrochemical parameters calculated from Figures 5.5-5.9

	Pt/C	**Pt-Cr 4/C**	**Pt-Cr 8/C**	**Pt-Cr 10/C**	**Pt-Cr 20/C**
ECSA (m^2/g_{Pt})	58	66	15	27	19
Tafel Slope	75	62	59	73	62
Specific Activity at 0.9 V (mA/cm^2_{Pt})	0.45	0.73	0.71	0.42	0.69
Mass Activity at 0.9 V (mA/mg_{Pt})	260	470	106	118	130

Table 5.3: Elemental distribution of Pt, Cr in different catalyst from TEM and XPS

Sample	**Pt (at. %)**	**Cr (at. %)**	**Cr in oxide form (% of Cr)**
Pt-Cr 4/C	100	0	0
Pt-Cr 8/C	80	20	43.4
Pt-Cr 10/C	70	30	43.5
Pt-Cr 20/C	80	20	53.7

The ECSA for Pt-Cr 4/C was highest among all samples including the commercial Pt/C catalyst. This high value can be attributed to the maximum amount of Pt reduction during the synthesis in the presence of Cr precursor and presence of very less agglomeration. However, as the amount of Cr was increased to 15 at.% in the Pt-Cr 8/C sample, the ECSA value decreased considerably. This is due to the uneven distribution of Pt and Cr over the whole area that has been observed using the TEM analysis as discussed in section 4.2.2. Thus, leaving patches of pure Pt, Cr, and Pt-Cr alloy which will not be sufficient to give the exact behaviour of catalyst. The ECSA value increased with the increase in the percentage of Cr for the Pt-Cr 10/C catalyst in which 30 at.% of Cr is present. As discussed in section 4.2, the nanoparticles form an alloy of Pt-Cr with very few small patches of pure Pt at some places and thus better distribution which can give rise to improved ECSA. However, for the Pt-Cr 20/C catalyst, enrichment of Pt on the surface of the catalyst was observed as discussed in section 4.2.2-4.2.4. The reduction of ECSA can be due to the higher amount of Nafion present in this case compared to Pt-Cr 10/C.

5.2.2 Oxygen Reduction Reaction (ORR)

As discussed in section 5.1.2, the ORR is a sluggish reaction and attempts are being made to improve the reaction rate, reduce the amount of Pt. Linear sweep voltammetry is an electrochemical technique which is quite useful in studying the kinetics of the ORR and thus can determine whether a catalyst is suitable for use in the fuel cell. In the present case, the catalysts being studied were the Nafion stabilised Pt-Cr alloys synthesised by borohydride reduction method. LSV curves were obtained in 0.1 M $HClO_4$ solution with O_2 purging to study the ORR mechanism. The detailed procedure has been discussed in section 3.3.

Figure 5.6 shows the linear sweep voltammograms of commercial Pt/C catalyst and different Pt-Cr/C alloy catalysts (a-e) and a final graph (e) comparing all catalysts at rotation speed of 1600 rpm. These voltammograms were recorded in O_2 saturated 0.1 M $HClO_4$ solution and then the corresponding component which recorded in N_2 saturated solution was subtracted. Then the data was normalised to remove the effect of IR drop. The LSV is dominated by the diffusion controlled region below 0.7 V for all the catalysts whereas it is under the influence of both kinetic and diffusion above 0.7 V.

It can be seen from the graphs that the onset of ORR for Pt-Cr 4/C has moved to higher potential as compared to the commercial Pt/C catalyst which may result in the improvement of catalytic activity of this catalyst. However, the curves for other catalysts have moved towards lower potentials which suggest a reduction in the activity.

From the graph (figure 5.6 (f)) showing the comparison of all catalysts at 1600 rpm, it can be seen that limiting current density for Pt-Cr 8/C and Pt-Cr 10/C was higher as compared to all other catalysts which have same current density. The possible reasons for the limiting current density are presence of some surface defects on the electrode, non uniform layer of catalyst on the electrode.

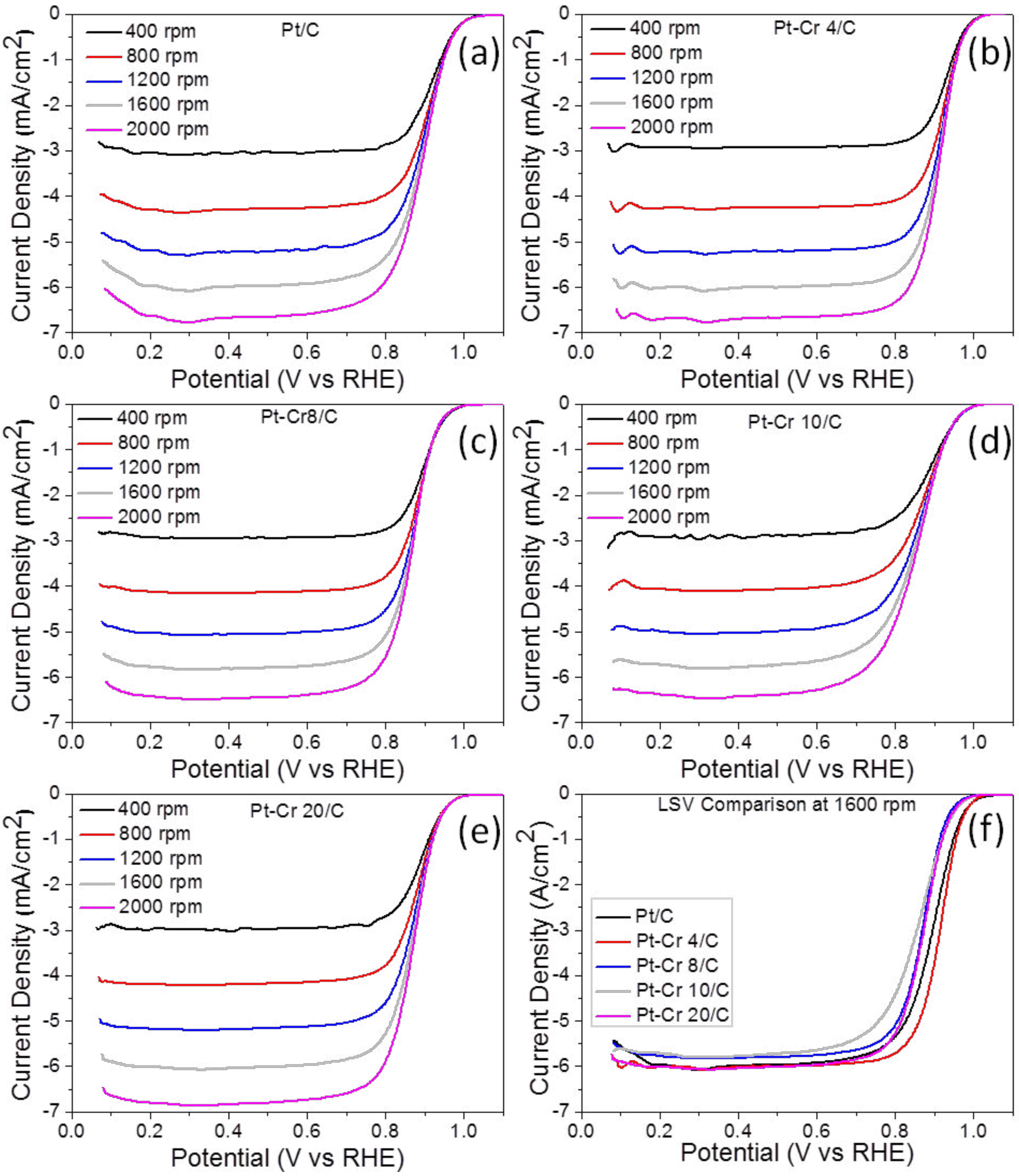

Figure 5.6: LSV graphs of the catalysts at different rotation rates in 0.1 M $HClO_4$ solution at 25°C. Current is normalised to geometrical surface area of working electrode.

The Koutecky-Levich graph as shown in Figure 5.7(a-e) suggest that all the catalysts show a linear relationship with the same slope as the 4 electron process for oxygen reduction. The number of electrons taking part in the oxygen reduction reaction for all the catalysts for the different potential shown in K-L graphs is calculated. Figure 5.7(f) show the change in number of electrons for the catalyst over the potential window of 0.7 V - 0.9 V.

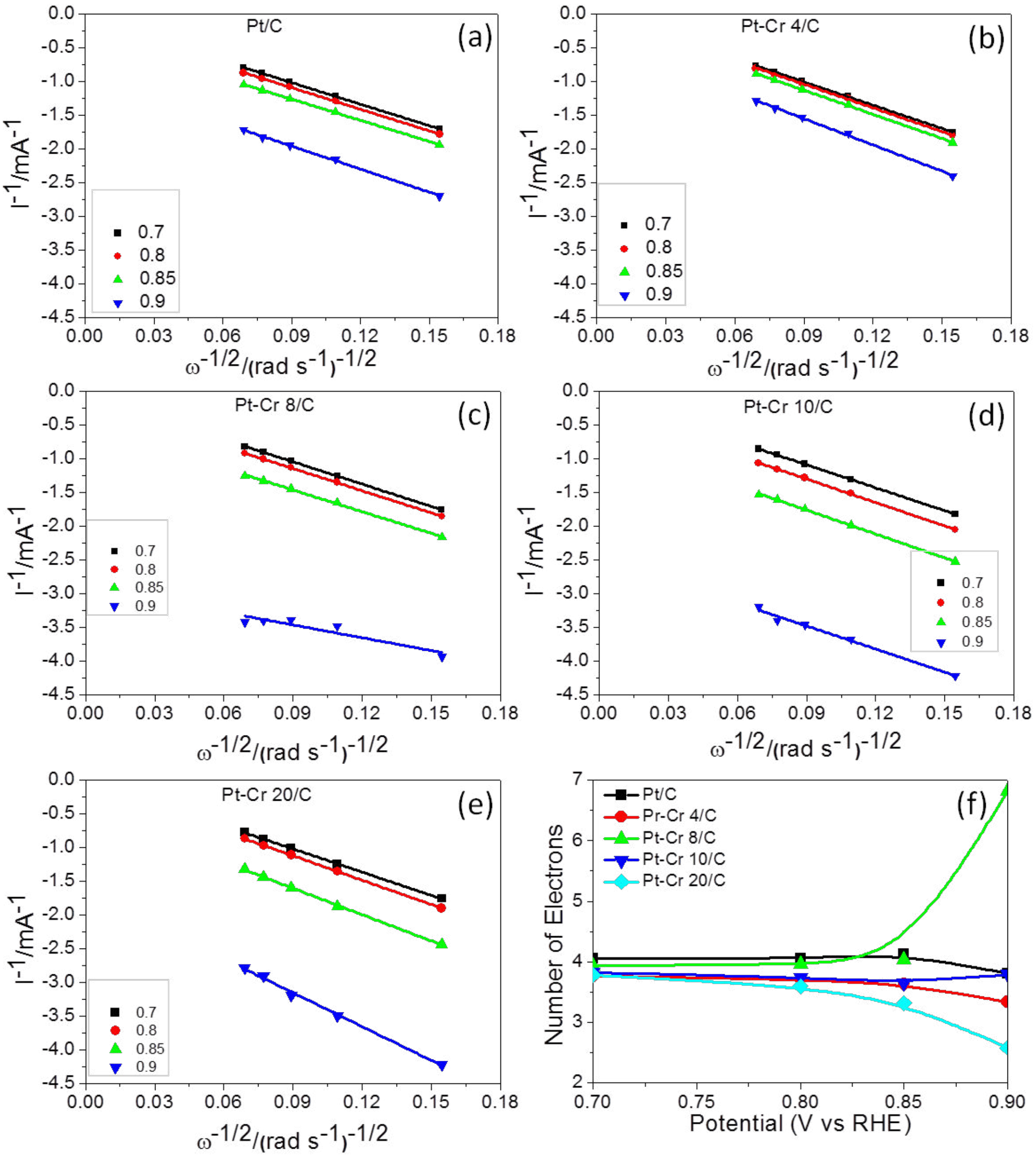

Figure 5.7: Koutecky-Levich plots for different catalysts (a-e) and number of electrons for all catalysts at different potentials (f)

It can be seen from the figure 5.7 (f) that the number of electrons is 4 for the potential 0.7 V-0.85 V for all the catalysts. However, Pt-Cr 8/C shows a deviation at the 0.9 V which is in agreement with change in slope observed in K-L graph shown in figure 5.7 (c) and also the LSV curve(figure 5.6(c) which showed shifting of onset potential to lower potentials. This behaviour is completely different from other catalysts and need further studies. Similar behaviour is observed for Pt-Cr 20/C catalyst also which showed change in slope for K-L curve (figure 5.7(e)) and onset potential shifting to lower potentials for LSV curve (figure 5.6(e)). Other catalyst did not show any change in slope and the number of electrons are 4 over the potential window which is in agreement with the LSV curves (figure 5.6).

Figure 5.8 shows the mass normalised Tafel plots for all the Pt-Cr catalysts in comparison to the commercial Pt/C catalyst. All catalysts show two slopes, one in the low overpotential region and other in the higher overpotential region. In the low over potential region, a slight change in the potential corresponds to a big change in the current density. However, for the high over potential region, an opposite trend is observed and the current density changes very less even with big change in the potential. Thus, it can be said that the slope in the low over potential region is smaller as compared to the slope in the higher over potential region. The slopes, as calculated for all the catalysts have been reported in table 5.2.

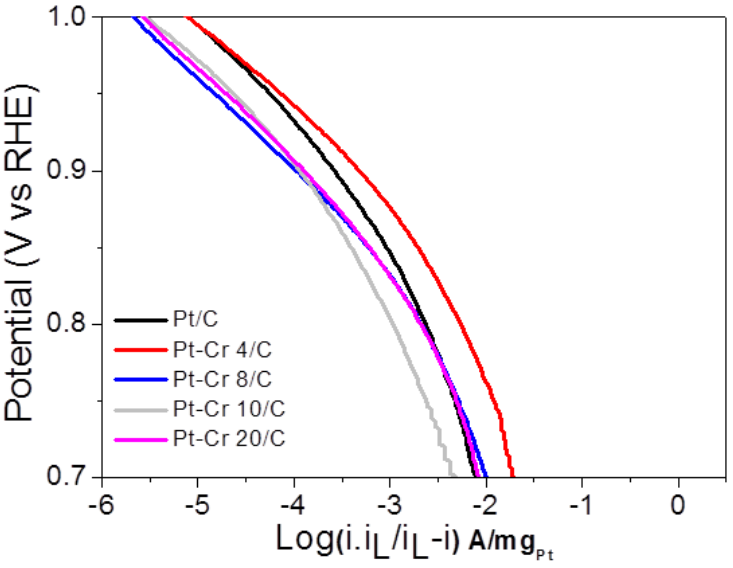

Figure 5.8: Tafel comparison for different alloy catalysts of Pt-Cr/C and commercial Pt/C

Specific and mass activity for all the catalysts were calculated at 0.9 V. Mass activity for Pt-Cr 4/C is the highest as can also be seen from the figure 5.8 followed by Pt/C. The mass activities for Pt-Cr 8/C, Pt-Cr 10/C and Pt-Cr 20/C are all in the same range and much lower than that of commercial Pt/C. However, all the Nafion stabilised catalysts showed better specific activity as compared to Pt/C. This activity enhancement can be related to two factors, 1) improved triple phase boundaries due to Nafion stabilisation and 2) formation of Pt-Cr alloys. It has been reported in literature that the formation of alloys lead to the improved activity by 1.5- 3 times which is in agreement with the results obtained in present case except Pt-Cr 10/C which showed similar specific activity as Pt/C [6-9]. This result could have been better explained with the extent of alloying as amount of alloying plays an important part in the activity of the catalysts.

5.2.3 Degradation Study

Degradation is a very important parameter which determines the lifetime of a catalyst. It can be termed as the change in the performance of the catalyst over period of time. Accelerated stress testing is a useful technique to study the degradation of a catalyst over different cycle of operation. In this technique, a catalyst is cycled between 0.6 V and 1.0 V which forms the peak power output and the open circuit potential for PEMFCs, respectively. The degradation is recorded by the change in the electrochemical surface area after every 1200 cycles till 4800 cycles. The commercial catalyst Pt/C is used as a reference in order to compare the degradation behaviour of the Nafion stabilised Pt-Cr catalysts synthesised in present case.

Figure 5.9 shows the cyclic voltammograms of different catalysts which were subjected to degradation cycle as mentioned in section 3.3.1.3. CV was recorded after every 1200 cycles to calculate the amount of degradation for each catalyst which in turn provided the reduction in the ECSA. The ECSA values obtained for each catalyst over the 4800 cycles are plotted and shown in the figure 5.9(f). The commercial catalyst degraded to a large extent and about 50% of the ECSA was left after 4800 cycles. It has been reported in literature that the degradation of Pt/C happens due to various reasons which range from increase in the particle size of the Pt, dissolution of the catalysts and also carbon corrosion [10-14].

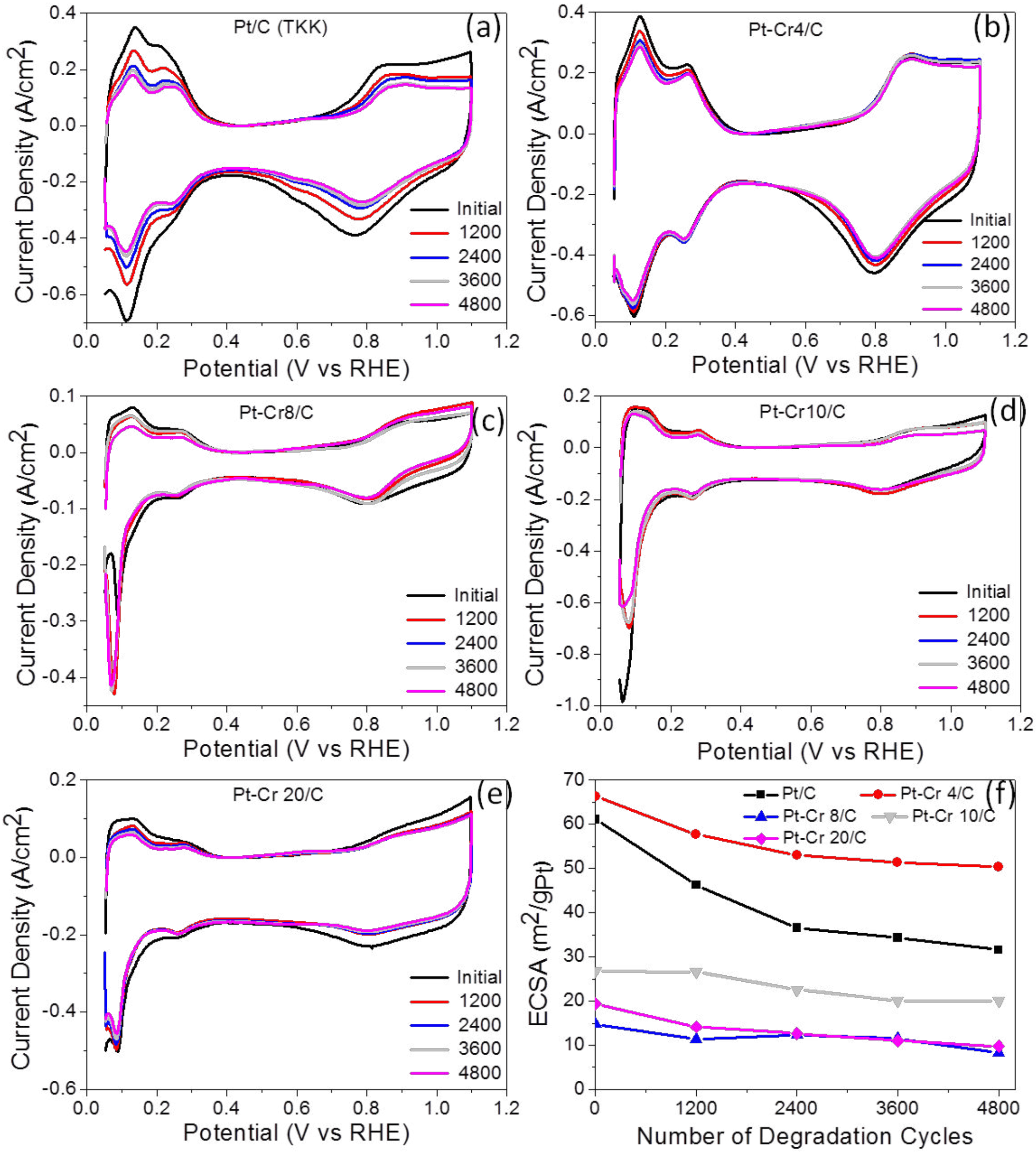

Figure 5.9: Degradation graphs of different catalysts over 4800 cycles

A 20-25% reduction in the ECSA is observed for the Nafion stabilised catalysts. This suggests that Nafion keeps the catalyst particles together which in turn helps in reducing the dissolution of the catalyst particle. The small loss of the ECSA can be due to the particle growth; however it was not possible to do TEM analysis of the catalyst ink after the degradation cycle was completed. However, the loss in ECSA for Pt/C is around 50% that is double the amount as observed for Nafion stabilised catalysts. Thus, it can be said that Nafion stabilisation is a possible solution to help control the degradation of the catalyst during the fuel cell operation. It has also been reported in literature that Nafion stabilisation helps in preventing the degradation of the catalyst [3, 5, 15-17]. However, the effect of amount of Cr on the degradation could not be separated as all the Pt-Cr samples degraded by similar amount.

5.2.4 Polarisation Behaviour of Catalysts

Figure 5.10 shows the relationship between voltage and power density with respect to current density for different catalyst materials synthesised using ethanol based borohydride reduction method. The performance of these catalysts has been compared to the commercial Pt/C catalyst. The commercial catalyst Pt/C (TKK) gives the best performance in this case followed by decreasing performance trend Pt-Cr 20/C > Pt-Cr 10/C > Pt-Cr 4/C > Pt-Cr 8/C respectively. The commercial catalyst showed highest peak current density of 1.52 A/cm^2 and maximum power density of 0.6 W/cm^2. The performance of the all the MEAs tested in present case was very low compared to the similar materials reported in the literature. Power densities of 0.85 W/cm2 at 0.6 V was obtained for E-Tek and TKK catalysts by Gastgeiger *et al.* [18]. In order to improve the performance of the MEAs in current study, significant improvements have to be done to the materials as well as the processing methods. Decal method for depositing catalyst layer directly on the membrane has shown significant performance improvement than coating on the gas diffusion layer and can in turn imorove the ionic conductivity between catalyst layer and membrane[19, 20]. The method used for the preparation of MEA in present case is hand painting and it has been described in detail in section 3.3.2. Current density and power density has been normalised to the Pt loading (0.3-0.4 mg/cm^2) for an MEA of 16 cm^2 area and the resulting graph is shown in figure 5.10 (b).

It can be seen from the figure 5.10 (a) that the open circuit potential (OCP) for the commercial catalyst (Pt/C) is higher as compared to all the catalysts synthesised in this study. This shows a drop in the performance of the catalysts that can be due to various reasons like the catalyst-support, synthesis method for the catalysts preparation and activation losses. However, it can also be seen that the value of OCP is constant for all the synthesised catalysts, which shows that the reason for performance losses is common to all of them; thus these catalysts can be easily compared amongst themselves.

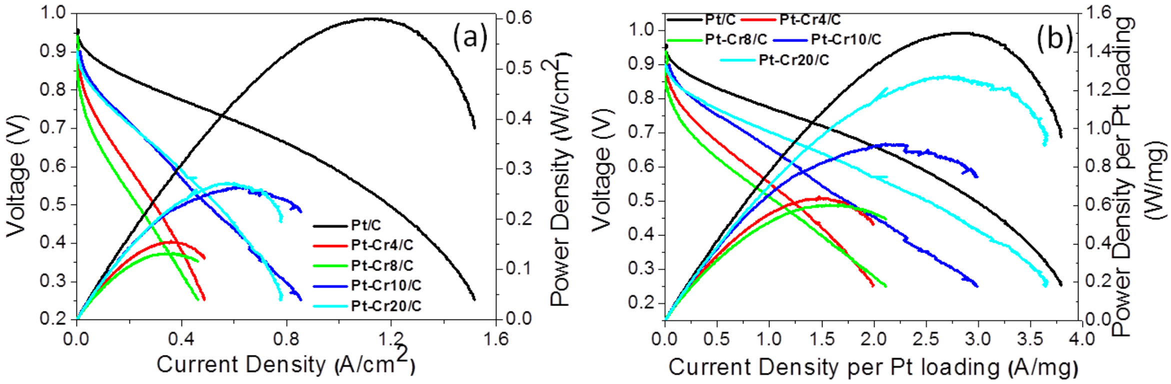

Figure 5.10: IV and PI curves for different catalyst as obtained from a single cell test (a) normalised with electrode area, (b) normalised with Pt loading

From figure 5.10(a), Pt-Cr 4/C catalyst showed a highest current density of 0.45 A/cm^2 and maximum peak power density of 0.15 W/cm^2 at a current density of 0.38 A/cm^2. The peak power density of 0.13 W/cm^2 was measured at a current density of 0.37 A/cm^2 for Pt-Cr 8/C. The maximum current density of 0.46 A/cm^2 was observed for this catalyst.

The figure 5.10 (a) shows low performance achieved when using Pt-Cr 4/C and Pt-Cr 8/C as the cell potential drops rapidly with increasing the current density. The maximum current density achieved for Pt-Cr 4/C was ~ 0.45 A/cm^2, which is very low compared to the commercial catalyst. However, the performance of the Pt-Cr 10/C and Pt-Cr 20/C catalysts is better as compared to Pt-Cr 4/C and Pt-Cr 8/C catalyst although still less than the commercial catalyst. There is a sudden drop in the current density at the low potential for Pt-Cr 10/C and Pt-Cr 20/C which can be due to the limitation in the oxygen mass transport through the catalyst layer. This is also seen in the performance of the Pt/C catalyst.

With further increase in the amount of Cr in the Pt-Cr 10/C sample, alloy formation and better distribution of these alloys over the whole area with only few regions of pure Pt are observed as discussed in chapter-4 section 4.2. Thus, Pt-Cr 10/C catalyst is showing better performance as compared to the Pt-Cr4/C and Pt-Cr8/C catalyst. It has been reported in literature also that alloy of Pt tend to show better performance than Pt [21-25]. However, when comparing this alloy with the Pt/C, the performance of alloy catalyst is almost half to that obtained in Pt/C. There are various reasons which can contribute to the lower performance:

1) The amount of Pt is less in alloy and thus the catalyst may not be properly distributed on the MEA and can have some areas with no or low catalyst concentration.
2) The nanoparticles in this case are agglomerated and thus have low ECSA which was shown during the RDE testing also. This can also contribute to low performance of the catalyst.
3) The amount of Nafion was higher in the case of alloy catalyst and may cause blocking of some of the catalysts.

The peak power density of 0.26 W/cm^2 was observed for Pt-Cr 10/C at the current density of 0.67 A/cm^2 which is half than the Pt/C catalyst but I believe that the performance of alloy catalyst can be improved by optimising the various parameters ranging from reducing agglomeration to optimising the amount of Nafion.

Pt-Cr 20/C catalyst showed slightly better performance than all other catalysts synthesised in the present case even though the amount of Cr was less as compared to Pt-Cr 10/C. This can be attributed to the Pt enrichment on the surface of the catalyst and thus, more Pt available for electrochemical reactions. Also the amount of Cr_2O_3 was higher in Pt-Cr 20/C which can further enhance the performance. There have been studies that suggest presence of metal oxides improves the performance of the catalyst by the dissolution of metal oxide and thus exposing more Pt for participation in electrochemical reaction [26-28]. However, extent of alloying in the catalyst plays an important role in the performance of catalyst.

The in-situ results obtained for all these catalysts can be compared to the ex-situ results obtained using the rotating disc electrode testing. From the electrochemical behaviour as observed using rotating disc electrode testing, it was believed that the Pt-Cr 4/C will show the best performance with respect to other catalysts as well as commercial Pt/C. However, it showed the worst performance which may be due to various reasons like a) uneven distribution of the catalyst, b) blocking of Pt sites by the Nafion present in the catalyst and c) non-uniform supporting of the Pt on the carbon support. Similar behaviour is observed for the Pt-Cr 8/C, Pt-Cr 10/C and Pt-Cr 20/C catalysts. The results obtained from RDE testing (section 5.2) are completely different from the fuel cell testing. This is due to the random distribution of the catalyst over the MEA as it uses higher amount of catalyst and thus all the regions present in the catalyst can be seen i.e. regions of pure Pt, Cr and Pt-Cr alloy which may not be present in the case of RDE due to the amount of catalyst used. These tests are repeated a minimum of three times to check the repeatability of the preparation of MEA and also the behaviour of the catalysts.

5.2.5 Electrochemical Impedance Spectroscopy (EIS) of Catalysts

Figure 5.11 shows the ac-impedance spectra obtained for all the catalyst in a low current density region and high current density region. The low current density value (0.05 A/cm^2) was same for all catalysts, however the high current density value changed depending on the performance of the catalyst and it was chosen as the value where maximum peak power was obtained. So this value may not fall into the mass transport region for some cases and thus the effect will only be due to the charge transfer resistance which dominates in the low current density region.

In the high current density region, we can clearly see two semi circles, one in the high frequency region and a second in the low frequency region. These similar trends have been widely reported in the literature [29, 30].The intercept of the arc on the Z' axis gives the value of the cell resistance (mainly influenced by membrane) in the high frequency region which is 0.1 ohm cm^2 which is true for the Nafion 112 membrane used in the present study. The main contribution to the first semicircle comes from the cathodic oxygen reduction process and thus this semicircle represents the fuel cell reaction kinetics. Whereas, the main contributor for the second semicircle is the diffusion of the oxygen to the Pt active surface area within the cathodic catalyst layer and thus this semicircle represents the mass transfer process. The first semi circle is dominant in the case of low current density (close to OCP) region, thus suggesting that the reaction process is limited by kinetics. When comparing the behaviour of all the catalysts in the low current density region, it can be seen that the semi circle arc follows the same trend as seen in the I-V curve shown in figure 5.10 that is Pt/C < Pt-Cr 20/C < Pt-Cr 10/C < Pt-Cr 4/C < Pt-Cr 8/C. The semi circle arc has increased in this trend and thus the charge transfer resistance for oxygen reduction which is the dominant mechanism in this region also follows the same trend. The mass transport region which is dominant at the low frequency region is not present and doesn't contribute to the impedance. These results verify the trend observed during the I-V curve which shows that catalyst performance is lowest for the Pt-Cr 8/C as the barrier to overcome the oxygen reduction reaction is very high whereas it is lowest for the Pt/C catalyst.

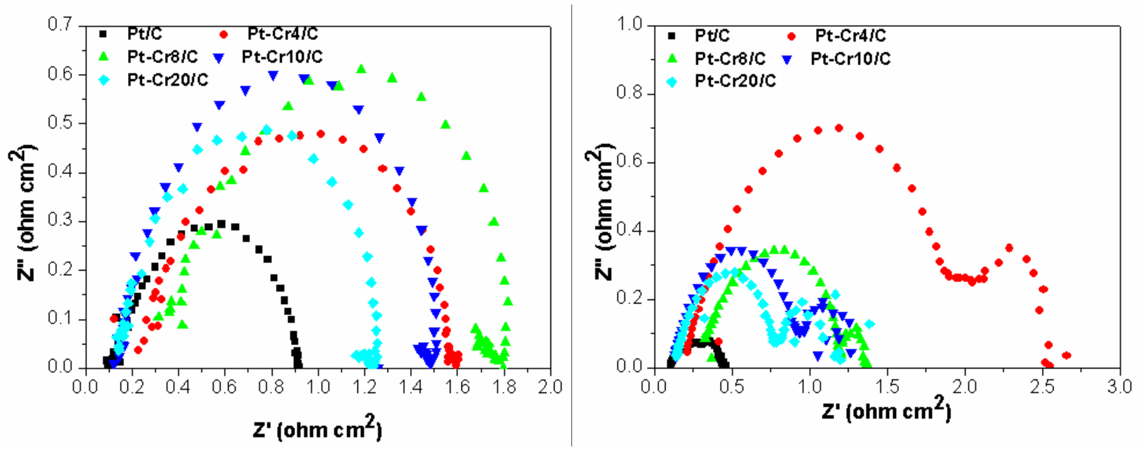

Figure 5.11: Ac-impedance spectra of all catalysts in the low current density and high current density region

In the high current density region, we also see two semi-circles, the high frequency region is dominant by the oxygen reduction reaction kinetics and the low frequency region is dominated by the mass transport of oxygen to the catalyst layer. With the increase in the current density, the first semi-circle gets shortened and the second semi-circle starts to broaden up as mass transport begins to dominate at the higher current density. This can be seen from the behaviour of Pt/C which is the commercial catalyst, the first semi-circle which ends around 0.9 ohm cm^2 is moved to 0.3 ohm cm^2 and the second semi-circle starts dominating from there which is mass transport controlled. However, the maximum intercept it reached is only 0.45 ohm cm^2 which is almost half of the intercept as it reached in the low current density region.

The same behaviour is true for all other catalysts also as the first semi circle gets shortened and we can clearly distinguish the second semi circle which was almost negligible in the low current density region. However, the Pt-Cr 4/C shows an opposite trend as even though we are saying it is high current density region, it never reaches the current density where the mass transport should be dominant. Thus, the charge transfer resistance is still dominant and the first semi circle further increases. The same behaviour was expected for the Pt-Cr 8/C catalyst, based on its performance in the I-V curve but it showed a decrease in the first semi circle and a slight region of second semi circle. The change in this behaviour is not completely understood and needs further studies.

Pt-Cr 10/C and Pt-Cr 20/C show reduction in the charge transfer resistance and also visible second semi circle which is due to the mass transport of oxygen to catalyst layer. Even though this is termed as high current density region, it still falls in the current density region where charge transfer, membrane and mass transfer resistance contribute almost equally to the performance of the cell and thus the behaviour is mixed which can be seen clearly from the impedance spectra.

5.3 Conclusions

Nafion stabilised Pt-Cr were synthesised using aqueous based method-1 with an average particle size of 6 ± 2 nm. No clear alloy formation was observed and only traces of Cr were present in the aqueous based synthesis. The ECSA of the PtCr/C catalyst was smaller compared to that of commercial Pt/C catalyst. However, PtCr/C catalyst showed an improved specific activity, almost three times higher relative to the Pt/C. Both the catalysts followed the same 4 electron process for the oxygen reduction, proving that Pt based materials follow same reaction pathway which leads to the formation of water. There was a small amount of Cr present in these nanoparticles and so another method was used successfully to improve Cr percentage in the alloys.

Different concentration of Pt-Cr alloys were synthesised with ethanol based reduction method-2 ranging from traces of Cr to 20-30 at.% Cr. The particle size as calculated from TEM and XRD was in the range of 4-10 nm. There was a huge variation in the ECSA for all these catalysts which followed the trend Pt-Cr 4/C > Pt/C > Pt-Cr 10/C > Pt-Cr 20/C > Pt-Cr 8/C. The catalyst with traces of Cr showed highest ECSA which can be due to the complete reduction of Pt and uniform distribution of this Pt over the whole area. However, as the Cr content increased, the ECSA value decreased which can be attributed to non-uniform distribution of the catalyst as well as presence of regions which are enriched in Pt, Cr or Pt-Cr alloy as seen in the TEM images. A different trend was observed for the specific activity and mass activity of these catalysts with the Pt-Cr 4/C showing highest activity amongst all samples including the commercial Pt/C. The specific activity of Pt-Cr 10/C was in the same range as Pt/C, however mass activity was much smaller. Pt-Cr 8/C and Pt-Cr 20/C showed almost double the specific activity but mass activity was only half as compared to Pt/C. The ex-situ degradation study showed that all the Nafion stabilised catalysts showed better durability as compared to the commercial Pt/C. The reduction in the ECSA was observed to be only 20-25% for the Nafion stabilised Pt-Cr/C catalysts as compared to almost 50% for Pt/C. These results confirm that the Nafion stabilised Pt-Cr/C can be used as catalysts for fuel cells. However, the effect of Cr on the degradation was not clear.

The catalysts followed the trend Pt/C > Pt-Cr 20/C > Pt-Cr 10/C > Pt-Cr 4/C > Pt-Cr 8/C in terms of performance during the study of I-V curves. This trend was due to various parameters such as amount of Cr present, alloying ratios, distribution of the catalyst layer, dissolution and corrosion of the support. This trend was further verified using the ac-impedance spectra recorded at low current density region and high current density region. The low current density region spectra were dominated by the cathodic oxygen reduction process which is fuel cell reaction kinetics. The high current density spectra showed varying trends and were dominated by different parameters for the catalysts. The charge transfer component was dominant in the case of Pt-Cr 4/C catalyst whereas charge transfer, membrane and mass transfer resistance contributed equally to the impedance in the case of Pt-Cr 10/C and Pt-Cr 20/C as the current density region never reached the complete mass transport region. However, the trend for Pt-Cr 8/C was completely different as predicted from the IV curve and needs to be further studied which is out of the scope of current study.

References

1. Garsany, Y., et al., *Experimental methods for quantifying the activity of platinum electrocatalysts for the oxygen reduction reaction.* Anal Chem, 2010. **82**(15): p. 6321-8.
2. Takahashi, I. and S.S. Kocha, *Examination of the activity and durability of PEMFC catalysts in liquid electrolytes.* Journal of Power Sources, 2010. **195**(19): p. 6312-6322.
3. Curnick, O.J., P.M. Mendes, and B.G. Pollet, *Enhanced durability of a Pt/C electrocatalyst derived from Nafion-stabilised colloidal platinum nanoparticles.* Electrochemistry Communications, 2010. **12**(8): p. 1017-1020.
4. Yang, H., et al., *Tailoring, Structure, and Activity of Carbon-Supported Nanosized Pt−Cr Alloy Electrocatalysts for Oxygen Reduction in Pure and Methanol-Containing Electrolytes.* The Journal of Physical Chemistry B, 2004. **108**(6): p. 1938-1947.
5. Liu, Z., Z.Q. Tian, and S.P. Jiang, *Synthesis and characterization of Nafion-stabilized Pt nanoparticles for polymer electrolyte fuel cells.* Electrochimica Acta, 2006. **52**(3): p. 1213-1220.
6. Qian, Y.D., et al., *PtM/C catalyst prepared using reverse micelle method for oxygen reduction reaction in PEM fuel cells.* Journal of Physical Chemistry C, 2008. **112**(4): p. 1146-1157.
7. Stamenkovic, V.R., et al., *Improved oxygen reduction activity on Pt3Ni(111) via increased surface site availability.* Science, 2007. **315**(5811): p. 493-7.
8. Yano, H., et al., *Oxygen reduction activity of carbon-supported Pt-M (M = V, Ni, Cr, Co, and Fe) alloys prepared by nanocapsule method.* Langmuir, 2007. **23**(11): p. 6438-45.
9. Zignani, S.C., E. Antolini, and E.R. Gonzalez, *Evaluation of the stability and durability of Pt and Pt–Co/C catalysts for polymer electrolyte membrane fuel cells.* Journal of Power Sources, 2008. **182**(1): p. 83-90.
10. Yu, X. and S. Ye, *Recent advances in activity and durability enhancement of Pt/C catalytic cathode in PEMFC.* Journal of Power Sources, 2007. **172**(1): p. 145-154.
11. Stevens, D.A. and J.R. Dahn, *Thermal degradation of the support in carbon-supported platinum electrocatalysts for PEM fuel cells.* Carbon, 2005. **43**(1): p. 179-188.
12. Shao, Y., G. Yin, and Y. Gao, *Understanding and approaches for the durability issues of Pt-based catalysts for PEM fuel cell.* Journal of Power Sources, 2007. **171**(2): p. 558-566.
13. Shao, Y., et al., *Durability Study of Pt⁄C and Pt⁄CNTs Catalysts under Simulated PEM Fuel Cell Conditions.* Journal of The Electrochemical Society, 2006. **153**(6): p. A1093.
14. Wang, Z.-B., et al., *Durability studies on performance degradation of Pt/C catalysts of proton exchange membrane fuel cell.* International Journal of Hydrogen Energy, 2009. **34**(10): p. 4387-4394.
15. Sarma, L.S., et al., *Carbon-supported Pt–Ru catalysts prepared by the Nafion stabilized alcohol-reduction method for application in direct methanol fuel cells.* Journal of Power Sources, 2005. **139**(1-2): p. 44-54.
16. Cheng, N., et al., *Improved lifetime of PEM fuel cell catalysts through polymer stabilization.* Electrochemistry Communications, 2009. **11**(8): p. 1610-1614.
17. Yin, S., et al., *A highly stable catalyst for PEM fuel cell based on durable titanium diboride support and polymer stabilization.* Applied Catalysis B: Environmental, 2010. **93**(3-4): p. 233-240.
18. Gasteiger, H.A., et al., *Activity benchmarks and requirements for Pt, Pt-alloy, and non-Pt oxygen reduction catalysts for PEMFCs.* Applied Catalysis B: Environmental, 2005. **56**(1-2): p. 9-35.
19. Bender, G., T.A. Zawodzinski, and A.P. Saab, *Fabrication of high precision PEFC membrane electrode assemblies.* Journal of Power Sources, 2003. **124**(1): p. 114-117.
20. Xie, J., et al., *Porosimetry of MEAs Made by "Thin Film Decal" Method and Its Effect on Performance of PEFCs.* Journal of The Electrochemical Society, 2004. **151**(11): p. A1841.

21. Yang, H., et al., *High Methanol Tolerance of Carbon-Supported Pt-Cr Alloy Nanoparticle Electrocatalysts for Oxygen Reduction.* Journal of The Electrochemical Society, 2005. **152**(4): p. A704.
22. Markovic, N.M., et al., *Oxygen Reduction Reaction on Pt and Pt Bimetallic Surfaces: A Selective Review.* Fuel Cells, 2001. **1**(2): p. 105-116.
23. Jeon, M.K., et al., *Combinatorial search for oxygen reduction reaction electrocatalysts: A review.* Journal of Power Sources, 2012. **216**: p. 400-408.
24. Greeley, J., et al., *Alloys of platinum and early tranisition metals as oxygen reduction electrocatalysts.* Nature Chemistry, 2009.
25. Jayasayee, K., et al., *Oxygen reduction reaction (ORR) activity and durability of carbon supported PtM (Co, Ni, Cu) alloys: Influence of particle size and non-noble metals.* Applied Catalysis B: Environmental, 2012. **111-112**: p. 515-526.
26. Seo, A., et al., *Performance and stability of Pt-based ternary alloy catalysts for PEMFC.* Electrochimica Acta, 2006. **52**(4): p. 1603-1611.
27. Park, K.-W., et al., *Chemical and Electronic Effects of Ni in Pt/Ni and Pt/Ru/Ni Alloy Nanoparticles in Methanol Electrooxidation.* The Journal of Physical Chemistry B, 2002. **106**(8): p. 1869-1877.
28. Zhang, J., ed. *PEM Fuel Cell Electrocatalysts and Catalyst Layers : Fundamentals and Applications*. 2008, Springer.
29. Tang, Y., et al., *Temperature Dependent Performance and In Situ AC Impedance of High-Temperature PEM Fuel Cells Using the Nafion-112 Membrane.* Journal of The Electrochemical Society, 2006. **153**(11): p. A2036.
30. Ahn, C.Y., et al., *Effects of ionomer content on Pt catalyst/ordered mesoporous carbon support in polymer electrolyte membrane fuel cells.* Journal of Power Sources, 2013. **222**: p. 477-482.

Chapter 6
Investigation Towards the Formation of Core-Shell Nanoparticles of Pt-Cr

The chapters 4 and 5 were focussed on the synthesis, characterisation and electrochemistry of Pt-Cr alloy electrocatalysts which were synthesised by borohydride reduction method. This chapter is focussed on attempting to synthesise and then characterise Pt-Cr core-shell nanoparticles with Cr as the core. The chapter will start with the description of the proposed route (synthesis method has been discussed in Chapter 3, section 3.2) followed by the characterisation techniques used for the analysis of the molecule and the nanoparticles are described. The final section details the electrochemical testing of these nanoparticles as PEMFC ORR catalyst using rotating disc electrode setup.

6.1 Proposed Strategy for the Synthesis of Pt/Cr Shell/Core Nanoparticles

In the current study, a new strategy has been proposed for the synthesis of Pt/Cr shell/core nanoparticles with the aim of using them as electrocatalysts in proton exchange membrane fuel cells (PEMFCs). The general strategy involves the formation of an intermediate Pt ion-containing supramolecular complex/non-noble metal nanomaterial which is later reduced to Pt/non-noble metal core/shell nanomaterial. The experimental procedure consists of 3 main steps:

Step 1 - Synthesis of ligands, which contain two terminal functional groups, namely: i) core surface-active head-group that will interact with the core non-noble material through weak non-covalent interactions using amines, carboxylic acids, etc or strong chemical bonds such as thiolate linkages using thiols or metal-carbon covalent bonds using diazonium derivatives; and ii) Pt-chelating moiety such as bipyridine, tripyridine, and acetylene [1-3].

Step 2 - Formation of the ligand/non-noble metal core nanomaterial using the reduction strategy described above for the synthesis of alloys is followed by immersion into the Pt-ion-containing solution. As a result, Pt ions adsorb on to the surface of the core by forming a complex with the chelating moiety.

Step 3 – The adsorbed Pt ions, on the intermediate Pt ion-containing supramolecular complex/non-noble metal, are reduced chemically to its zero-valent state to form Pt/non-noble metal core/shell nanostructured materials.

The detailed synthesis of Pt/Cr shell/core nanoparticles has been discussed in chapter-3 in section 3.2. The organic ligand employed for this study are the diazonium compounds which are reactive intermediates and characterised by the diazonium ion $N\equiv N^+$, usually attached to an aromatic ring as shown in Figure 6.1

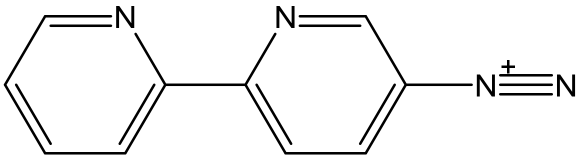

Figure 6.1: Chemical structure of a diazonium compound, namely [2, 2'-bipyridine]-5-diazonium (D-BiPy)

Grafting of diazonium derivatives to metals, metal oxides, polymers can be done easily by reduction[4]. An extremely reactive radical is formed after the reduction of a diazonium salt with the release of N2 and this radical can form a covalent bond with any available material e.g. metals like Pd[5], Au[6], Pt[6], Ti [7] and Cr in the present study. Metallic nanoparticles were formed after the reduction of metal precursor which was present alongwith diazonium derivatives and these nanoparticles were covalently bonded to the diazonium derivative. Diazonium derivatives are prone to react quickly due to the presence of highly reactive radical and thus it should be prepared immediately prior to use. Sodium nitrite is mostly used for the preparation of diazonium derivate by the oxidation of an amine precursor in acidic aqueous solution. As the process of diazonium derivative formation is done in aqueous solution, the product need to dried thoroughly prior to use in the synthesis of Cr nanoparticles.

6.2 Characterisation

The various characterisation techniques are reported in chapter-3 i.e thermogravimetric analysis (TGA), transmission electron microscopy (TEM), X-ray diffraction (XRD), X-ray photoelectron spectroscopy (XPS). Nuclear magnetic resonance (NMR) and fourier transformed infrared spectroscopy (FTIR) were used to study the formation of diazonium compound in this case whereas TGA, TEM, XRD and XPS are used to study the Pt/Cr shell/core nanoparticles. The analysis done using each technique is discussed below:

6.2.1 Nuclear Magnetic Resonance (NMR)

This technique is used to study the molecular structure of the NH_2-BiPy that is used to functionalise the Cr nanoparticles and act as a stabiliser to prevent oxidation of Cr. Figure 6.2 shows the H^1 NMR spectra of the NH_2-BiPy and D-BiPy. The solvent used for all the samples was MeOD and the peaks at the position 3.3 and 4.7 ppm resembles the solvent.

Water peak is mixed with the solvent peak for the D-BiPy sample at 4.6 ppm. The remaining peaks were all assigned to the hydrogen atoms in the bipyridine molecule. Disappearance of amine peak can be clearly seen in the figure 6.2 (b) at the position 4.25 ppm which suggests that the amine has been reduced to the diazonium moiety. This can be further confirmed by the shifting of the entire spectra to higher ppm. The peak shifting is the result of replacement of NH_2 by N_2^+ which is an electron withdrawing group. One such shift of the peak is highlighted in blue colour in the spectra i.e. from 7.9 ppm to 9.6 ppm.

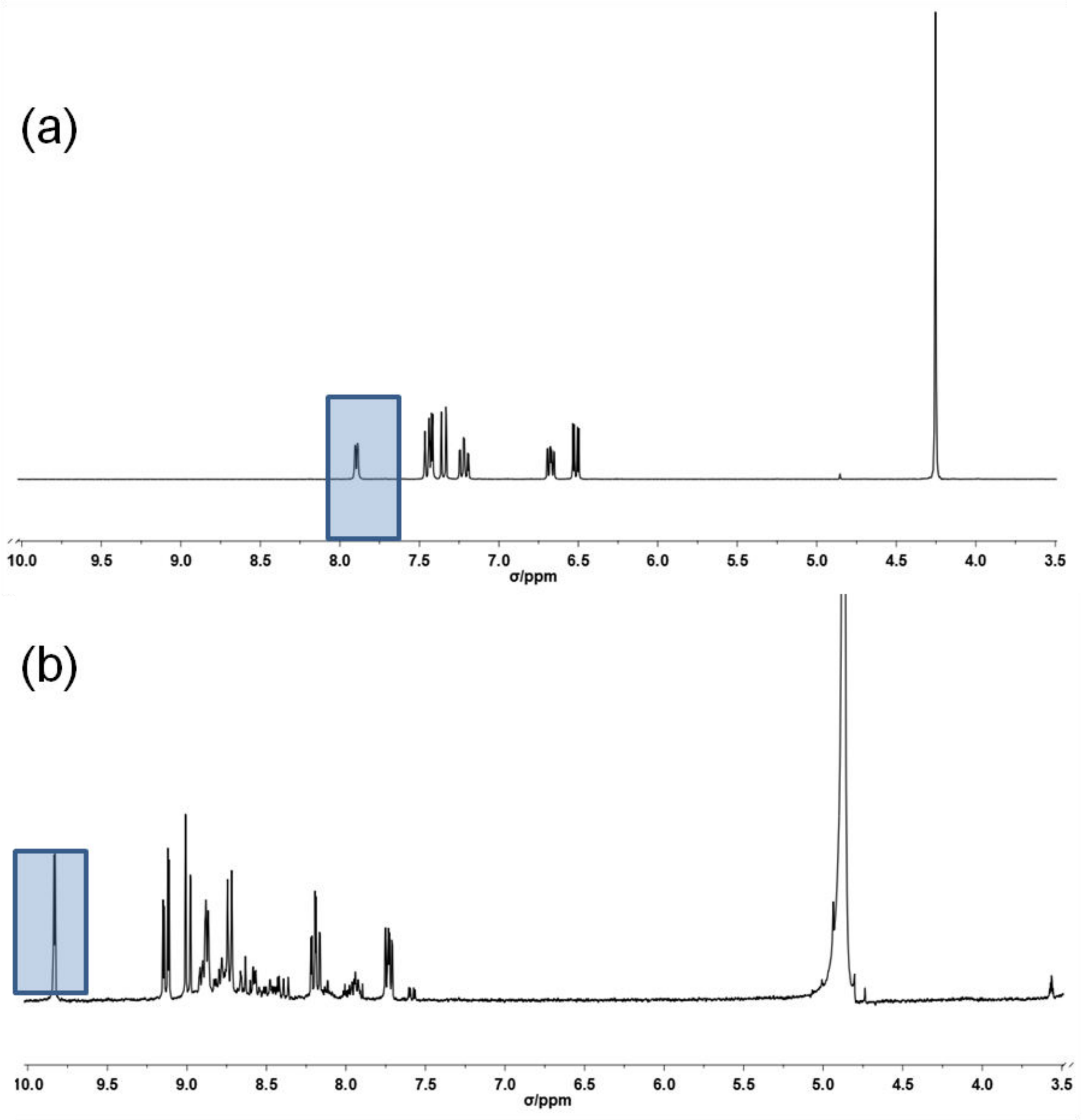

Figure 6.2: NMR spectra for (a) NH_2-BiPy (b) D-BiPy

6.2.2 Fourier Transformed Infrared Spectroscopy (FTIR)

FTIR is a useful technique to study the different bond structures present in a molecule as every bond has a specific wavenumber and thus change in the position can be related to the change in the structure. Figure 6.3 shows the FTIR spectra in the range of 2000- 2500 cm^{-1} to study the diazonium region for the NH_2-BiPy and D-BiPy. The appearance of a peak at 2290 cm^{-1} confirms the formation of diazonium ion $N{\equiv}N^+$.

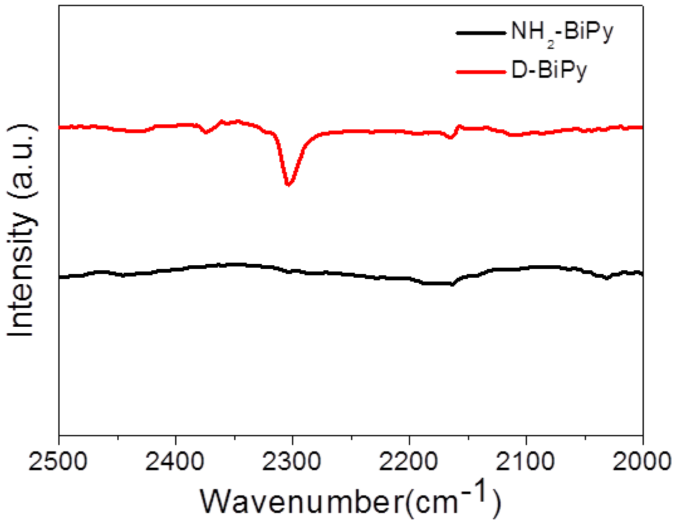

Figure 6.3: FTIR spectra of NH_2-BiPy and D-BiPy

Formation of D-BiPy is also confirmed from the mass spectrometer analysis which gave the mass as 187.1 which is equal to theoretical mass of D-BiPy.

6.2.3 Thermogravimetric Analysis (TGA)

The synthesis of Pt/Cr shell/core nanoparticles involved the use of the NH_2-BiPy which does not contribute to the electrochemistry. In order to calculate the amount of Pt and Cr, the molecule has to be decomposed completely. TGA is a useful technique which records the change in mass with increasing temperature and thus can record the decomposition of bipyridine molecule attached with the nanoparticles. The conditions used for the decomposition include a temperature range from 30 to 600 °C and a heating rate of 10 °C/min with air as the environment.

Figure 6.4 shows the TGA graph for the NH_2-BiPy and Pt/Cr shell/core nanoparticles synthesised as described above. A drastic change in mass can be seen for the bipyridine molecule between 150 °C and 260 °C. After this temperature, the mass is almost negligible and all of the bipyridine is decomposed. For the Pt/Cr shell/core nanoparticles, a drastic change in mass can be observed between 60- 150 °C which can be attributed to the water present in the system. After 150 °C, there was only a slight change in the mass (<5%) and it can be due to the decomposition of bipyridine molecule attached to the nanoparticles as the decomposition temperature for bipyridine is between 150-260 °C. So the amount of nanoparticles present in the dried sample was found to be 80 wt. % with the rest being water and bipyridine molecule. This percentage of Pt/Cr in the nanoparticles was used for the preparation of catalyst ink to study the electrochemical behaviour.

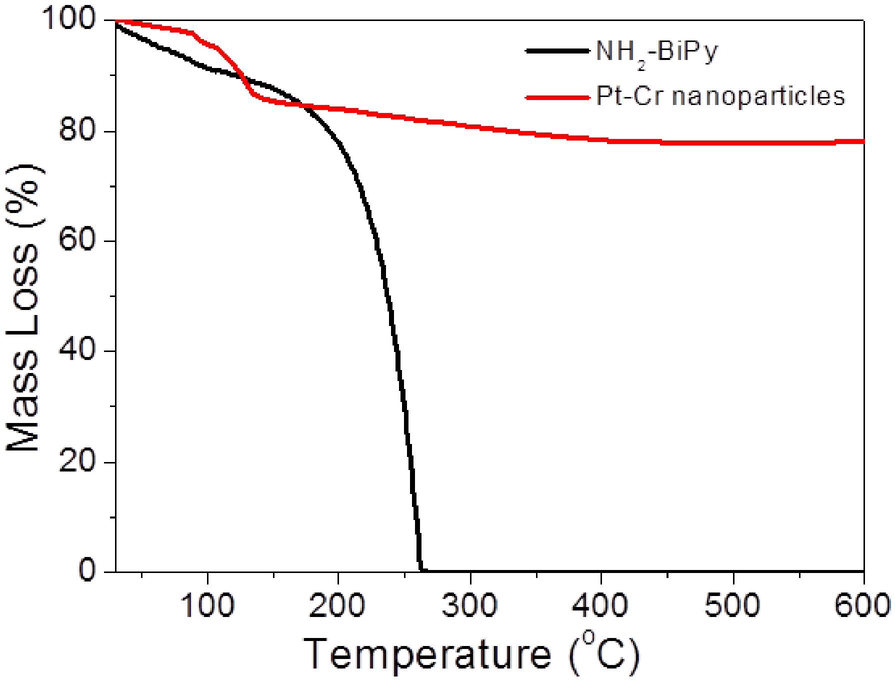

Figure 6.4: TGA of NH_2-BiPy and Pt/Cr shell/core nanoparticles

6.2.4 Transmission Electron Microscopy (TEM)

TEM is a very useful technique to study the particle size, morphology, distribution of the nanoparticles and also the composition when it is coupled with EDS. In the present case, Pt/Cr shell/core nanoparticles were synthesised employing the bipyridine derivative which acts as stabiliser for the Cr core. TEM study was done on the Cr core and Pt/Cr shell/core to determine the size, morphology and composition of the nanoparticles.

Figure 6.5 shows the TEM images (a, c) and corresponding EDS spectra (b, d) on the Cr and Pt/Cr shell/core nanoparticles, respectively. The Cr nanoparticles were dispersed and do not form any agglomerates. The average particle size was found to be 1.8 ± 0.3 nm. The particle size was calculated by ImageJ software over different areas and by analysing 100 particles. EDS spectra (figure 6.5 (b)) confirms the presence of Cr on the nanoparticles. Figure 6.5 (c) shows the TEM image of Pt/Cr shell/core nanoparticles synthesised by reducing Pt precursor on the Cr core. The nanoparticles were well dispersed and do not form any agglomerates and size distribution was very narrow (inset figure 6.5(c)). The average particle size of the nanoparticles was 2.5 ± 0.5 nm. EDS spectrum (figure 6.5(d)) taken over an area of (c) shows the presence of both Pt and Cr in the nanoparticles and the composition analysis suggested the ratio of Pt: Cr was 70:30. The core/shell formation of these nanoparticles cannot be confirmed with TEM and it requires use of aberration corrected STEM or super STEM that are not accessible currently and this will be done in future studies.

Thus we can say we have Pt-Cr nanoparticles with an average size of 2.5 nm and presence of Pt and Cr in the ratio of 70:30.

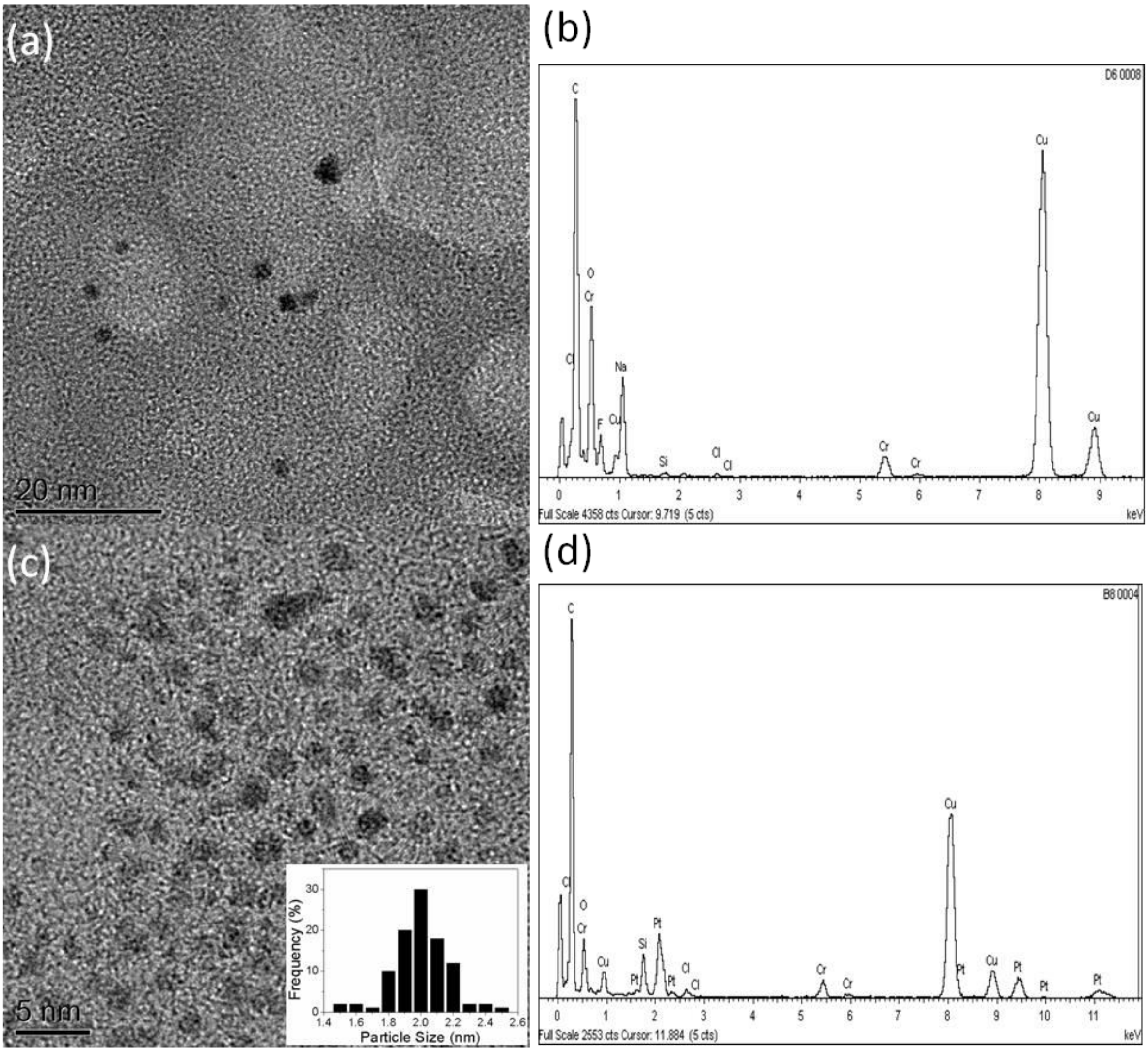

Figure 6.5: TEM images of Cr (a) and Pt/Cr (c) nanoparticles and EDS spectra Cr (b) and Pt/Cr (d) nanoparticles

6.2.5 X-Ray Diffraction (XRD)

XRD is a useful technique to study the crystalline structure of the nanoparticles as well as calculate the particle size. The XRD samples are prepared by putting powder sample on an aluminium substrate which has a small cavity and the details of the various parameters used are given in section 3.2.3. The samples studied in this part are the Pt nanoparticles and Pt/Cr shell/core nanoparticles synthesised by the same procedure as described in section 3.2.

Figure 6.6 shows the XRD graphs for Pt and Pt/Cr shell/core nanoparticles. The peaks corresponding to the FCC structure of Pt are all present in both the cases and these are all labelled accordingly. The extra peak around 58 degree was from the substrate material. The crystallite size was calculated using the Scherer equation as described in the chapter 3, section 3.2.3 which is as under:

$$B = \frac{K\lambda}{\beta \mathrm{Cos}\,\theta}$$

where B is the mean crystallite size, K is the dimensionless shape factor constant which is usually taken as unity, λ is the wavelength of the X-rays used (1.5405 Å), β is the line broadening at half the maximum intensity (FWHM) and θ is the Bragg's angle.

The crystallite size was calculated using the Pt (220) peak as the error in calculation becomes lower as we move towards the higher θ values [8, 9]. The crystallite size for Pt was 2 nm and for Pt/Cr shell/core was 2.3 nm. This is in agreement with the size calculated from TEM analysis discussed in section 6.2.4.

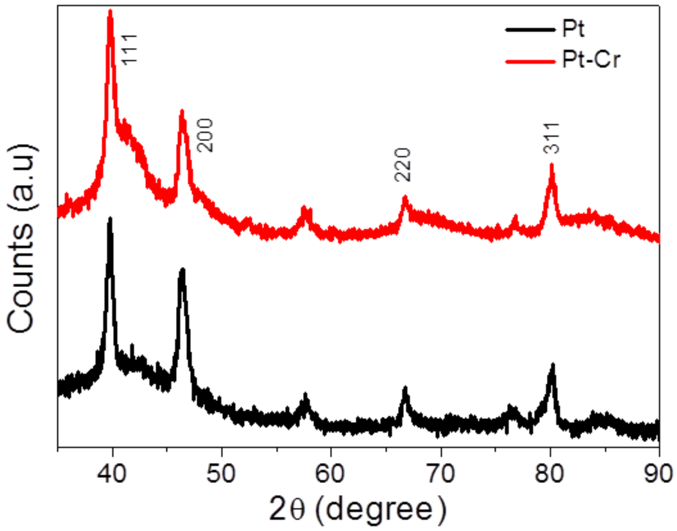

Figure 6.6: XRD graph for Pt and Pt/Cr shell/core nanoparticles

For the calculation of lattice parameters, the d-spacing was calculated for the different peak positions using the Bragg's law.

$$n\lambda = 2d\ Sin\theta$$

where n is an integer, λ is the wavelength of the X-ray used (1.5405 Å), d is the d-spacing between the planes, θ is the Bragg's angle of reflection.

After the calculation of d-spacing, the following equation for the calculation of lattice parameter for cubic system is used

$$d = \frac{a}{\sqrt{h^2 + k^2 + l^2}}$$

where d is the d-spacing for a given plane, a is the lattice parameter, (h,k,l) are the reciprocal indices of the planes.

The lattice parameters for both the samples calculated using the above equations were 3.92 Å and 3.91 Å for Pt and Pt/Cr, respectively. The lattice parameters for both the samples were similar to the normal lattice parameters for Pt.

6.2.6 X-Ray photoelectron Spectroscopy (XPS)

The techniques discussed in section 6.2.4 and 6.2.5 i.e. TEM and XRD are useful techniques for the study of the particle size, morphology, distribution and composition of the nanoparticles. However, the oxidation states of the elements present was very important to study the amount of metal present in the native state, which will in turn contribute to the electrochemical behaviour of the catalyst. XPS is a surface sensitive technique which can be used to detect the presence of even trace amount of impurities present in the sample along with the oxidation states of the various elements.

Figure 6.7 (a) shows the survey spectrum of the Pt/Cr nanoparticles. The elemental analysis done on the survey spectra shows the presence of Pt and Cr in the ratio of 1.2:1. The other elements present in the spectrum are C (bipyridine molecule), O (metal oxide), N (bipyridine, $NaNO_2$ residues), Na ($NaBH_4$, $NaNO_2$ residues), F (HBF_4) and B (HBF_4, $NaBH_4$ residues). Bipyridine molecule was expected to be present due to the entrapment of the molecule between Pt and Cr. However, the amount of impurities of Na, F and B were in very high amount and thus the synthesis method and purification needs improvement. The elemental distribution obtained has been reported in the table 6.1. It is to be noted here that this was one of the various samples tested and some samples just suggested presence of pure Pt and no Cr.

Table 6.1: Elemental distribution of Pt/Cr nanoparticles

Element	Pt	Cr	C	O	N	Na	F	B
At %	1.2	1	35.6	26.7	1.7	11.3	18.5	4

Figure 6.7 (b) shows the elemental high resolution XPS spectrum for C 1s with peak fitting for different components present. It shows the presence of 3 components which were C-C (284.7 eV), C-N (288.2 eV) and the third component C 1s_3 (292.2 eV) could not be resolved and thus needs further analysis. However, it was outside the scope of current studies due to time constraints. The two components C-C and C-N form the basic building blocks for the bipyridine molecule and thus it proves the presence of bipyridine in the final nanoparticles.

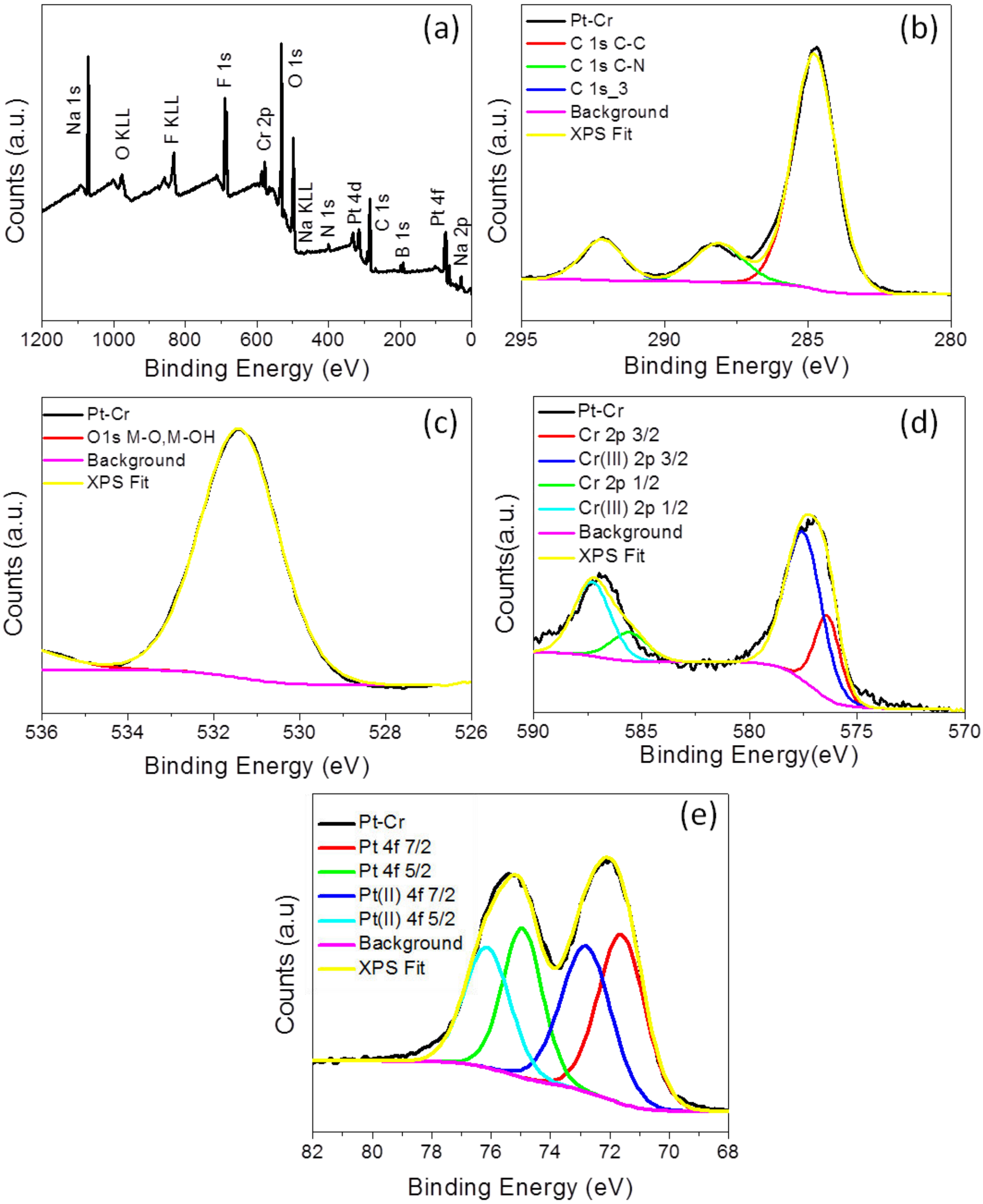

Figure 6.7: XPS spectra of Pt/Cr shell/core nanoparticles

Figure 6.7 (c) shows the XPS spectrum for the oxygen with peak fitting for the different components. The peak at 531.4 eV has been assigned to the metal oxide peak which can be due to the oxidation of Cr or Pt. The analysis of Cr and Pt high resolution spectra is shown in figure 6.7 (d and e) respectively. The Cr spectrum shows presence of around 80 % of Cr_2O_3

(577.5 eV and 587.3 eV) component and only 20 % pure Cr (576.4 eV and 585.6 eV). The analysis of Pt spectrum suggested the presence of pure Pt (71.6 eV, 74.9 eV) and almost similar amount of Pt $(OH)_2$ (72.8 eV, 76.1 eV). This suggests the presence of hydroxide component in the oxygen spectrum. Since the binding energy for hydroxide falls in the range of 531- 532 eV which was very near to the binding energy of metal oxide, it was possible that both peaks are overlapping and cannot be resolved. So the oxygen component at 531.4 eV can be assigned to metal oxide and metal hydroxide mixture. Thus it can be said that the nanoparticles have 55% pure Pt and 20% pure Cr and presence of bipyridine molecule was also confirmed. It has been reported in literature that Pt^0 contributes to the electrochemical activity for ORR and if the content of Pt^0 decrease, the catalytic activity decreases [10-12]. So only this 55% pure Pt will contribute to the electrochemistry of the nanoparticles.

6.3 Electrochemical Testing of Pt-Cr/C

Pt-Cr nanoparticles were synthesised using bipyridine derivative as the stabiliser with an aim to produce core/shell structure of Cr/Pt. Though, we can confirm the formation of Pt/Cr nanoparticles with presence of bipyridine derivative from the analysis of the different characterisation data discussed in the section 6.2 (TGA, TEM, XRD, XPS), the formation of core/shell structure cannot be confirmed. In order to study the electrochemical behaviour of these nanoparticles, they were supported on Vulcan XC-72 to form the catalyst and then a small amount of Nafion was also added in the mixture. Aliquot of the catalyst was dropped on the glassy carbon electrode that forms the working electrode. The working electrode was then tested in 0.1 M $HClO_4$ solution with a normal hydrogen electrode and a platinum mesh as reference and counter electrode, respectively. The detailed procedure has been discussed in section 3.4. A standard Pt/C (TKK) catalyst has been studied alongside these catalysts to compare the behaviour. The different electrochemical techniques used and the analysis is discussed below.

6.3.1 Cyclic Voltammetry (CV)

Cyclic Voltammetry is a very useful electrochemical technique to study redox reactions. One of the important parameters in the study of catalysts is the electrochemical surface area which can be determined by studying the hydrogen adsorption/desorption reaction. This region usually occurs between 0.05-0.4 V vs NHE and the area under the graph gives the charge of the monolayer of hydrogen desorbed which can be converted to electrochemical surface area using equation 3.1 as reported in section 3.4.

Figure 6.8 shows the cyclic voltammograms of Pt/C and Pt-Cr/C in N_2 saturated 0.1 M $HClO_4$ solution at 25 °C with the current normalised to the geometrical surface area of the electrode. Hydrogen adsorption and desorption region was present in the range of 0.05-0.4 V. Two clear peaks were visible in the Pt/C catalysts whereas the peaks could not be resolved properly for the Pt-Cr/C catalyst. Also, the current density for Pt/C was very high compared to Pt-Cr/C which suggests that the electrochemical surface area will be higher for Pt/C. Table-6.2 shows the value of the ECSA as calculated from the equation reported in section 3.4.1.1 and shown below:

$$\mathrm{ECSA}=\frac{Q_H}{210\ L_{Pt}A}$$

where Q_H (μC) is the charge measured upon desorption of H_2 in the underpotentially-deposited (UPD) hydrogen region, L_{Pt} is the Pt loading (μg/cm^2), A is the geometric area of the working electrode (cm^2) and the value of 210 C/cm^2 corresponds to the charge required to adsorb/desorb a monolayer of H_2 on bulk polycrystalline Pt surface.

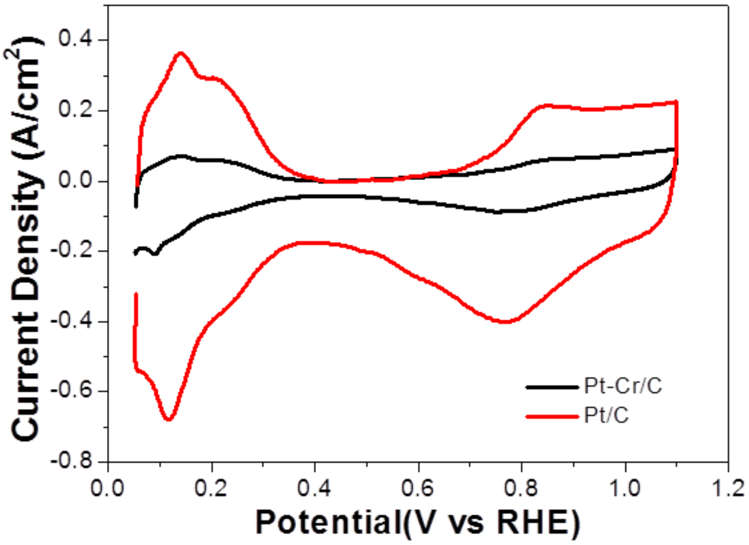

Figure 6.8 Cyclic voltammograms of Pt/C and Pt-Cr/C catalysts in 0.1 M $HClO_4$ solution at 25 °C. The current is normalised to the geometrical electrode area

Table 6.2: Electrochemical parameters calculated for Pt/C and Pt-Cr/C from figure 6.8- 6.11

	Pt/C	**Pt-Cr/C**
ECSA (m^2/g_{Pt})	58	16.5
Tafel Slope	75	66
Specific Activity at 0.9 V (mA/cm^2_{Pt})	0.51	0.63
Mass Activity at 0.9 V (mA/mg_{Pt})	250	88.9

The ECSA for Pt/C was determined to be 58 m^2/g_{Pt}, which is in agreement with the literature values [13, 14]. The ECSA for the Pt-Cr/C catalysts was 16.5 m^2/g_{Pt} which was very low compared to Pt/C catalyst. The possible reason was the low amount of Pt actually participating in the electrochemical reaction as some of it may be shielded by the oxides and also the biypridine molecule. So the ECSA reported here was only an approximation with 80 % Pt-Cr present in the nanoparticles as calculated from TGA analysis.

6.3.2 Oxygen Reduction Reaction (ORR)

ORR forms an important part of the catalyst study as it is the most sluggish reaction and forms the limiting step for the fuel cell operation. Thus, a lot of catalyst is being used on the cathode side to improve the ORR kinetics and in order to reduce the loading of Pt, alloys and core-shell structures are being studied. Linear sweep voltammetry (LSV) is a useful technique to study the ORR reaction mechanism which in turn can be used to calculate the performance of a catalyst by the use of Koutecky-Levich and Tafel plots. LSV curves were obtained in 0.1 M $HClO_4$ solution with O_2 purging to study the ORR mechanism. The detailed procedure has been discussed in section 3.4.

Figure 6.9 shows the linear sweep voltammograms for Pt/C and Pt-Cr/C in O_2 saturated 0.1 M $HClO_4$ solution. The current was normalised to the geometrical surface area of the electrode. This data has been subtracted from the LSV curves obtained for N_2 saturated solution and also normalised to IR drop. It was clear from the figure 6.9 that ORR is diffusion controlled below a potential of 0.7 V and beyond this ORR was controlled by mixed diffusion kinetics in the potential region of 0.7- 1.0 V. The diffusion limited current density for both catalysts was almost similar except for rotation speed of 400 rpm. The onset of ORR in case of Pt-Cr/C has shifted to lower potentials which contribute to lower activity as compared to Pt/C catalyst.

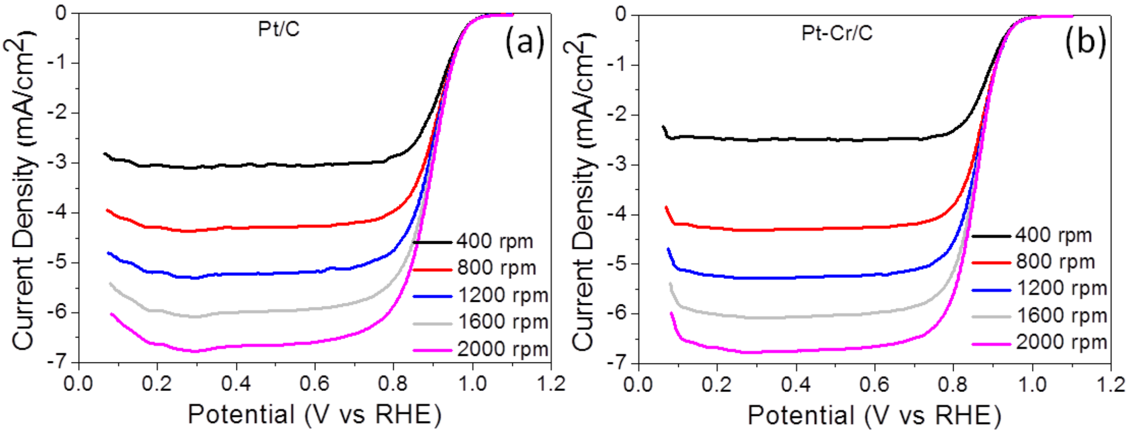

Figure 6.9: Linear Sweep Voltammograms of Pt/C (a) and Pt-Cr/C (b) catalysts in 0.1M $HClO_4$ at 25 °C. Current normalised to the geometrical area of working electrode

Furthermore, the Koutecky-Levich plots (figure 6.10) for these catalysts show a linear relationship between 1/I and $1/\omega^{-1/2}$. Both the catalysts show different slopes and thus it can be said the mechanism of oxygen reduction was different for both catalysts. The slope was calculated using the Levich equation which is

$$I_{lim} = 0.62\ n\ A\ F\ C\ D^{2/3} v^{-1/6}\ w^{1/2}$$

where I_{lim} is the limiting current, n is the number of electrons for the reaction, A is the electrode area (0.196 cm^2), F is Faraday's constant (96500 C/mol), C is the concentration (1.26 x 10^{-6} mol cm^{-3}), D is the diffusion coefficient of oxygen (1.93 x 10^{-5} cm^2/s), v is the kinematic viscosity (0.009 cm^2/s), and w is the rotation rate of the electrode.

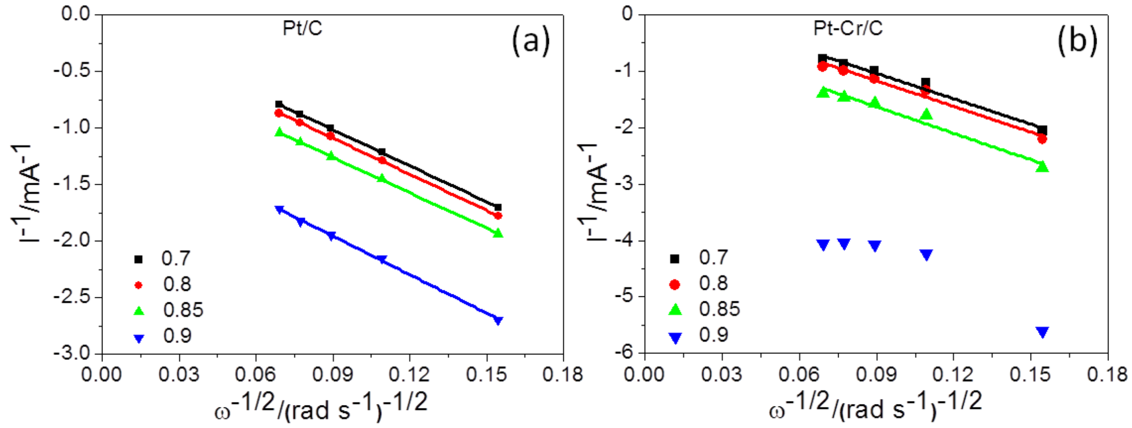

Figure 6.10: Koutecky-Levich graphs for (a) Pt/C and (b) Pt-Cr/C

The number of electrons was calculated for both catalysts from the analysis of the Levich equation. It was found that Pt/C has 4 electrons for the oxygen reduction reaction whereas Pt-Cr/C has only 2-3 electrons. Thus, the mechanism of oxygen reduction reaction was different. It suggests that the bipyridine molecule maybe interfering with the ORR reaction. There have been various studies on catalysts with M-N_2, M-N_4 (M- a metal, N- nitrogen from pyridine, other chelating agents) type of arrangement where nitrogen also participates in the ORR reaction and the kinetics was different from the 4 electron process [15-20]. Even though there has been no studies on Pt-N_2 or Pt-N_4 arrangements but it is possible that the same behaviour of transition metal arrangement can be applied in this case also where the nitrogen from the pyridine, bipyridine will take part in the ORR and thus the kinetics will be different compared to pure Pt behaviour.

Figure 6.11 shows the Tafel plots for Pt/C and Pt-Cr/C with the mass normalised kinetic current. Tafel slopes can be calculated from the figure which shows two regions. The Tafel slopes obtained at higher potentials (>0.9 V) for Pt/C and Pt-Cr/C catalysts were 75 and 66 mV/decade, respectively. It was evident from the figure that the mass activity (SA) of the Pt/C catalyst was much higher than Pt-Cr/C catalyst and the values of the mass activity as reported in table 6.2 suggests the same. Pt-Cr/C shows a mass activity which was almost one third of the Pt/C catalyst. However, Pt-Cr/C shows a slightly higher specific activity. There have been some reports suggesting the improved activity for catalysts having surface oxides in this case Cr_2O_3. This happens due to the dissolution of oxides resulting in the enrichment of surface with Pt and thus increased activity [21-23]. However, to understand the behaviour of the catalysts, the detailed analysis for nanoparticles need to be done using aberration corrected STEM.

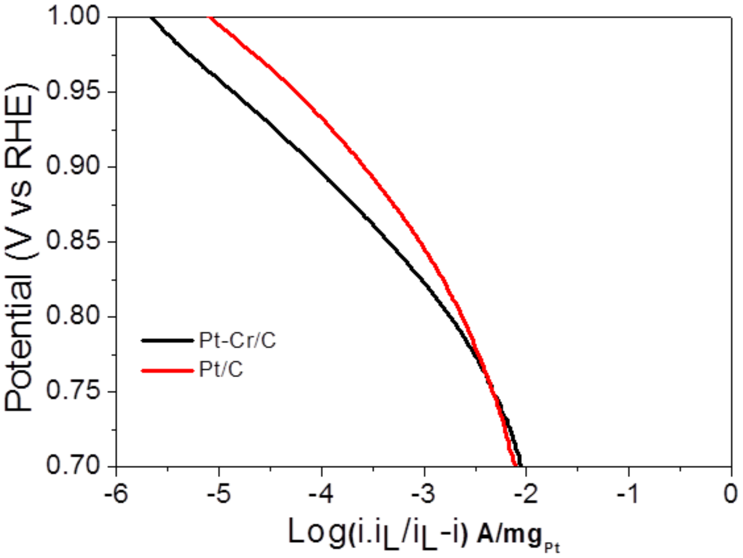

Figure 6.11: Tafel comparison for Pt/C and Pt-Cr/C in 0.1M $HClO_4$ at 25 °C

The possible reasons for the poor electrochemical behaviour of these catalysts can be due to the formation of different structure as illustrated in figure 6.12. These include incomplete coverage of the Cr core by the Pt shell (figure 6.12 a and b), thus exposing more Cr for electrochemical behaviour. Bipyridine molecule can also cause the blockage of the Pt shell from electrochemical behaviour by forming a layer on top of the shell (figure 6.12 c). Formation of different arrangement like Pt-N_2 and Pt-N_4 (figure 6.12 d and e) which can contribute to 2-3 electron process as evident from the electrochemical results discussed in section 6.3. Thus, further studies need to be done to study the exact structure of these nanoparticles by aberration corrected STEM.

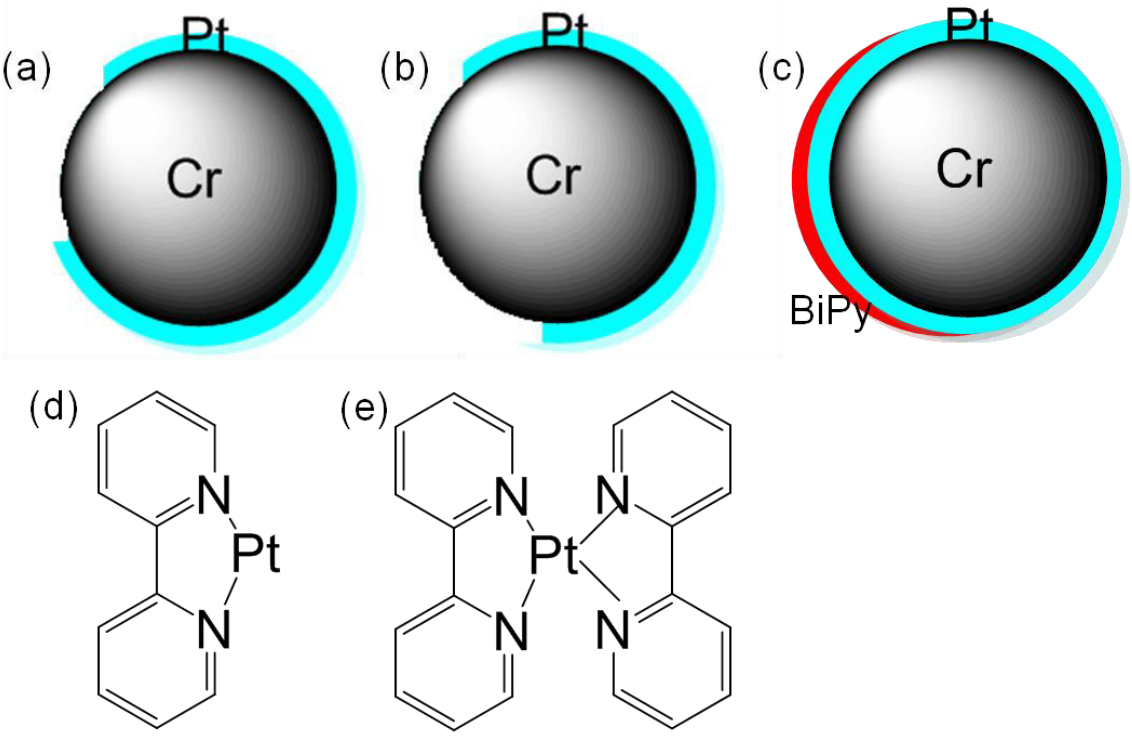

Figure 6.12: Schematic of possible core-shell structures (a-c) and Pt interaction with bipyridine molecule (d-e) in the present study

6.4 Conclusions

Pt-Cr nanoparticles stabilised with bipyridine molecule were synthesised with an average particle size of 2.5 ± 0.5 nm, confirmed from TEM and XRD results. The TGA analysis showed 5% decomposition of the bipyridine derivative and the metal content was calculated as 80% i.e. the residual mass left after the scan at 600 °C. Nanoparticles showed presence of 30 at.% Cr as evident from the TEM analysis and 80% of that Cr was in oxidised form as seen from XPS. XPS also confirmed the presence of almost 45% of Pt in the Pt^{2+} state corresponding to the Pt $(OH)_2$ and it was believed that this Pt does not contribute to the electrochemical behaviour. Presence of bipyridine molecule along with other remaining impurities was also confirmed from the XPS analysis. The ECSA of the Pt-Cr/C catalyst was very small as compared to that of commercial Pt/C catalyst. Also the Pt-Cr/C catalyst does not follow the same 4 electron process for oxygen reduction reaction as the number of electrons calculated for the ORR for Pt-Cr/C is only 2-3. Mass activity was also very low for Pt-Cr/C catalysts whereas it showed slightly higher similar specific activity as compared to Pt/C catalyst. The possible reasons for this electrochemical behaviour were due to the interference of the nitrogen in the bipyridine molecule.

References

1. Sreeprasad, T.S., et al., *Reduced graphene oxide-metal/metal oxide composites: facile synthesis and application in water purification.* J Hazard Mater, 2011. **186**(1): p. 921-31.
2. Sajanlal, P.R., et al., *Anisotropic nanomaterials: structure, growth, assembly, and functions.* Nano Rev, 2011. **2**.
3. Sreeprasad, T.S. and T. Pradeep, *Reversible assembly and disassembly of gold nanorods induced by EDTA and its application in SERS tuning.* Langmuir, 2011. **27**(7): p. 3381-90.
4. Mahouche-Chergui, S., et al., *Aryl diazonium salts: a new class of coupling agents for bonding polymers, biomacromolecules and nanoparticles to surfaces.* Chemical Society Reviews, 2011. **40**(7): p. 4143-4166.
5. Ghosh, D. and S. Chen, *Palladium nanoparticles passivated by metal-carbon covalent linkages.* Journal of Materials Chemistry, 2008. **18**(7): p. 755-762.
6. Mirkhalaf, F., J. Paprotny, and D.J. Schiffrin, *Synthesis of Metal Nanoparticles Stabilized by Metal−Carbon Bonds.* J Am Chem Soc, 2006. **128**(23): p. 7400-7401.
7. Ghosh, D., et al., *Titanium Nanoparticles Stabilized by Ti−C Covalent Bonds.* Chemistry of Materials, 2008. **20**(4): p. 1248-1250.
8. Cullity, B.D., *Elements of X-ray diffraction*. 1956, Reading, Massachusetts: Addison-Wesley Publishing Company, Inc.
9. Suryanarayana, C. and M.G. Norton, *X-Ray Diffraction: A Practical Approach*. 1998, New York: Plenum Press.
10. Seo, A., et al., *Performance and stability of Pt-based ternary alloy catalysts for PEMFC.* Electrochimica Acta, 2006. **52**(4): p. 1603-1611.
11. Shukla, A.K., et al., *An XPS study on binary and ternary alloys of transition metals with platinized carbon and its bearing upon oxygen electroreduction in direct methanol fuel cells.* Journal of Electroanalytical Chemistry, 2001. **504**(1): p. 111-119.
12. Aricò, A.S., et al., *An XPS study on oxidation states of Pt and its alloys with Co and Cr and its relevance to electroreduction of oxygen.* Applied Surface Science, 2001. **172**(1-2): p. 33-40.
13. Garsany, Y., et al., *Experimental methods for quantifying the activity of platinum electrocatalysts for the oxygen reduction reaction.* Anal Chem, 2010. **82**(15): p. 6321-8.
14. Takahashi, I. and S.S. Kocha, *Examination of the activity and durability of PEMFC catalysts in liquid electrolytes.* Journal of Power Sources, 2010. **195**(19): p. 6312-6322.
15. Othman, R., A.L. Dicks, and Z. Zhu, *Non precious metal catalysts for the PEM fuel cell cathode.* International Journal of Hydrogen Energy, 2012. **37**(1): p. 357-372.
16. Rao, C.V., *Iron and Nitrogen containing Carbon Catalysts with Enhanced Activity for Oxygen Reduction in Proton Exchange Membrane Fuel Cells.* Open Journal of Physical Chemistry, 2011. **01**(01): p. 11-22.
17. Zhang, L., et al., *Progress in preparation of non-noble electrocatalysts for PEM fuel cell reactions.* Journal of Power Sources, 2006. **156**(2): p. 171-182.
18. Koslowski, U.I., et al., *Nature of the Catalytic Centers of Porphyrin-Based Electrocatalysts for the ORR: A Correlation of Kinetic Current Density with the Site Density of Fe−*N_4 *Centers.* Journal of physical Chemistry C, 2008. **112**: p. 15356-15366.
19. Herrmann, I., et al., *Oxalate supported pyrolysis of CoTMPP as electrocatalysts for the oxygen reduction reaction.* Electrochimica Acta, 2009. **54**(18): p. 4275-4287.

20. Schulenburg, H. and S. Stankov, *Catalysts for the Oxygen Reduction from Heat-Treated Iron(III) Tetramethoxyphenylporphyrin Chloride: Structure and Stability of Active Sites.* Journal of Physical Chemistry B, 2003. **107**: p. 9034-9041.
21. Park, K.-W., et al., *Chemical and Electronic Effects of Ni in Pt/Ni and Pt/Ru/Ni Alloy Nanoparticles in Methanol Electrooxidation.* The Journal of Physical Chemistry B, 2002. **106**(8): p. 1869-1877.
22. Gasteiger, H.A., et al., *Activity benchmarks and requirements for Pt, Pt-alloy, and non-Pt oxygen reduction catalysts for PEMFCs.* Applied Catalysis B: Environmental, 2005. **56**(1-2): p. 9-35.
23. Antolini, E., J. Salgado, and E. Gonzalez, *The stability of Pt–M (M=first row transition metal) alloy catalysts and its effect on the activity in low temperature fuel cellsA literature review and tests on a Pt–Co catalyst.* Journal of Power Sources, 2006. **160**(2): p. 957-968.

Chapter 7

Conclusions and Recommendations for Future Work

7.1 Conclusions

The present work focussed on two different approaches of bimetallic catalyst synthesis in order to 1) reduce the amount of Pt loading, 2) improve the catalytic activity and 3) improve durability of the catalysts. The first approach involved the synthesis of Nafion-stabilised Pt-Cr alloy catalysts using wet chemical synthesis to incorporate the benefits of Nafion stabilisation and alloying. The detailed characterisations of these catalysts were done to confirm the formation of alloys and electrochemical characterisation to study the catalytic behaviour and durability. The second approach focussed on the synthesis of core-shell nanoparticles of Cr/Pt using supramolecular chemistry in order to form a monolayer of Pt on Cr core.

The initial attempts to synthesise Nafion-stabilised Pt-Cr using aqueous based solvent was not successful and only Pt nanoparticles with traces of Cr were formed. The average particle size of these nanoparticles was 6 ± 2 nm with some of the agglomerated particles reaching particle size higher than 10 nm. Even though no alloy formation was observed in these nanoparticles, they showed three times higher catalytic activity compared to commercial Pt/C catalyst but a very low electrochemical area. This was attributed to Nafion stabilisation resulting in improved triple phase boundary.

The synthesis method was modified to ethanol based solvent and also different ratios of reducing agents were used to synthesise Pt-Cr alloys. Alloys with an average particle size of 6 ± 2 nm and Cr concentrations of around 20-30 at.% were synthesised. It was also observed that the alloy distribution was not uniform over all the nanoparticles and there were regions enriched in Pt. Further, Nafion decomposition was observed during the synthesis process. XPS analysis confirmed the decomposition of Nafion i.e. breaking of side chains which resulted in the presence of C-C and reduction of side chains. The presence of C-C peak suggests that even though the side chains of the Nafion are breaking, the broken chains were still attached with the nanoparticles or left trapped in the Nafion chains and thus forms part of the structure.

The electrochemical characterisation showed Pt-Cr 4/C having the highest electrochemical surface area as well as better activity compared to other system studied. All the Nafion stabilised catalyst (20-25% loss) showed better durability in comparison to Pt/C catalysts (50% loss).

In-situ electrochemical testing was done only for the alloy catalysts synthesised using ethanol as solvent. When the Cr content in the alloy was increased to 20-30 at.%, the performance of the alloy catalysts improved, however it was still half to that of commercial Pt/C catalysts.

In the second part of this work, the synthesis of Cr/Pt core/shell nanoparticles was attempted using supramolecular chemistry. Pt-Cr nanoparticles with 30 at.% Cr were synthesised with an average particle size of 2.5 ± 0.5 nm, however, the core-shell structure could not be confirmed from the TEM results and needs further analysis by aberration corrected STEM. The electrochemical performance of Pt-Cr/C was studied and it was found to be very less in comparison to Pt/C catalyst. The possible reason for the lower performance can be partial covering of the Pt shell on Cr core as well as the possible interaction of Pt with residual bipyridine.

To summarize, the aim and objectives enlisted at the beginning of this study have been accomplished as follows:

1. Nafion-stabilised Pt-Cr alloy catalysts have been successfully synthesised using wet-chemical synthesis.
2. Electrochemical studies both ex-situ and in-situ were performed extensively to study the electrocatalytic activity and durability.
3. Core/shell nanoparticles of Cr/Pt were attempted using supramolecular chemistry and it was confirmed that nanoparticles containing 30 at.% Cr are present. However, the core/shell could not be confirmed using TEM.

7.2 Recommendations and Suggestions for Future Work

The present work endeavoured to synthesise Pt-Cr alloy catalysts stabilised with Nafion and also Cr/Pt core/shell nanoparticles for electrocatalysts in proton exchange membrane fuel cells (PEMFCs). In lieu of the results presented in this study the following suggestions have been proposed in consideration for future work:

1. Even though Nafion-stabilised Pt-Cr alloy catalysts were successfully synthesised, they still need improvements in terms of better uniformity, distribution, optimisation of Nafion content and also lowering the agglomeration of these nanoparticles to achieve better performance for PEMFCs.

2. It was observed that Nafion structure was broken during the synthesis process and showed the formation of C-C and other bonds with the breakage of side chains. Further studies need to be done to understand the mechanism of this process.
3. The formation of core/shell nanoparticles of Cr/Pt could not be confirmed and need further analysis using aberration corrected STEM.
4. A lot of oxidation was observed for Cr during the synthesis of Cr/Pt core/shell nanoparticles and thus this synthesis should be performed in inert atmosphere to avoid oxidation and get a stable core of Cr.
5. The strategies described here can be exploited for other non-precious metal (e.g. Ti, Ni, Co, Fe).